Heterogeneous catalysis in highly sensitive microreactors

Olsen, Jakob Lind

Publication date:
2010

Document Version
Early version, also known as pre-print

Center for Individual Nanoparticle Functionality

Heterogeneous catalysis in highly sensitive microreactors

Jakob Lind Olsen

May 31st 2010

Center for Individual Nanoparticle Functionality
Technical University of Denmark

DTU

Preface

The work presented in this dissertation have been carried out at the Technical University of Denmark (DTU), Department of Physics, at the Center for Individual Nanoparticle Functionality (CINF), from March 2007 to June 2010 with Professor Ib Chorkendorff and Associate Professor Ole Hansen as supervisors. CINF is funded by the Danish National Research Foundation which is greatly acknowledged for its support to this project. This dissertation is submitted in partial fulfillment of the requirements for obtaining the PhD degree from this university.

I would like to thank the students and staff at the department, and in particular at CINF, for their helpfulness and friendliness. My years as a PhD student would not have been the same without such great colleagues, both in regards to research activities and social aspects. I am grateful to Ib Chorkendorff for his guidance with respect to my project and sharing his understanding of the field of catalysis. I would also like to thank Ole Hansen for his help with all the technical details of the microreactors.

Jakob Lind Olsen
Kgs. Lyngby, May 31^{st}, 2010

Abstract

This thesis present a highly sensitive silicon microreactor and examples of its use in studying catalysis.

The experimental setup built for gas handling and temperature control for the microreactor is described. The implementation of LabVIEW interfacing for all the experimental parts makes automated experiments and data collection possible. An argon flush at the O-rings (used to interface the silicon microreactor with the gas system), which was developed, is presented. It enables experiments with temperatures up to 400℃, and up to 500℃ for short periods of time.

The CO oxidation reaction on platinum thin films is used to test the sensitivity of the microreactor. Activity is shown to be measurable for as little as a 15 μm^2 platinum, with an activation energy of $\sim$1 eV. A study of the light off phenomenon on platinum, showing light off at room temperature in gas mixtures of CO and O_2 with a large oxygen surplus, is presented.

The effect of pretreating the catalyst, CuZnO, in a mixture of H_2 and CO before methanol synthesis, is presented. Transient increased methanol production is seen after pretreatment, with a maximum in the transient for a pretreatment with a one to one CO to H_2 ratio. The highly active state of the catalyst after pretreatment in a CO and H_2 mixture is shown to have transient methanol synthesis capabilities at 60℃. Estimates of the area of the catalytic surface, is obtained using formate temperature programmed desorption measurements. From these, the possibility of adsorbates readily converted to methanol as the source of the transient increase in methanol production, is eliminated.

A study of mass selected ruthenium nanoparticles from a magnetron-sputter gas-aggregation source, deposited in microreactors, is presented. It is, shown that CO methanation can be measured on the mass selected nanoparticles in the microreactor. A parameter study shows negative reaction order in the CO concentration and apparent activation energies between 0.8 and 1.2 eV depending on reaction conditions. Temperature programmed reaction studies in H_2m shows different forms of carbon growth on ruthenium nanoparticles subjected to methane and CO at 250℃.

The use of the microreactor for photocatalysis and the development of a new two phase microreactor intended for photoelectrocatalysis is described. A single experiment of water electrolysis, with simultaneous measurement of H_2, O_2, and the cell current, is presented.

Resumé

Denne afhandling præsenterer en silicium mikroreaktor med høj følsomhed og eksempler på dens brug til studier af katalyse.

Det eksperimentelle setup bygget til behandling af reaktionsgasser og temperaturstyring beskrives. Implementeringen af kommunikation gennem LabView for alle komponenter, gør det muligt at automatisere eksperimenter og dataopsamling. Argon udskylning ved O-ringene (brugt til sammenkoblingen af silicium mikroreaktoren og gassystemet), som blev udviklet præsenteres, dette tillader eksperimenter at blive udført med temperaturer op til 400℃, og 500℃ i kortere tidsrum.

CO oxidation på platin tyndfilm bliver brugt til at teste følsomheden af mikroreaktoren. Det vises, at aktivitet af så lidt som 15 μm^2 platin tyndfilm kan måles med mikroreaktoren med en aktiveringsenergi på ca. 1 eV. Et studie af "light off" fænomenet på platin, som viser "light off" ved stuetemperatur i en gasblanding af CO og O_2 med stort overskud af O_2, præsenteres.

Effekten af at forbehandle katalysatoren, CuZnO, i blandinger af H_2 og CO før metanolsyntese beskrives. Efter forbehandling ses transient øget metanolproduktion, med en maksimal transient efter en forbehandling med en gasblanding med et en til en forhold mellem H_2 og CO. Den meget aktive tilstand af katalysatoren efter forbehandling i en CO og H_2 gasblanding vises at kunne producere metanol ved 60℃ i en begrænset periode. Muligheden for at den aktive tilstand af katalysatoren kan tilskrives adsorbanter som nemt omsættes til metanol afvises ved brug af estimater af overfladearealet af katalysatoren, ud fra format temperatur programmeret desorptionsmålinger.

Et studie af masseselekterede rutheniumnanopartikler, fra en magnetronsputter gas-aggregeringskilde deponeret i mikroreaktorer, præsenteres. Det vises, at CO metanisering på de masseselekterede nanopartikler kan måles i mikroreaktorene. Et parameterstudie viser en negativ reaktionsorden for CO koncentrationen, og en aktiveringsenergi mellem 0,8 og 1,2 eV, afhængig af reaktionsbetingelserne. Temperatur programmeret reaktionsstudier i H_2 viser deponering af forskellige former for kul på rutheniumnanopartiklerne udsat for metan og CO ved 250℃.

Brugen af mikroreaktorer til fotokatalyse og udviklingen af en ny to fase mikroreaktor til fotoelektrokatalyse beskrives. Et enkelt eksperiment med vand elektrolyse, hvor H_2, O_2 og strømmen gennem cellen måles simultant præsenteres.

Contents

1 Introduction **1**
- 1.1 Heterogeneous catalysis . . . 1
  - 1.1.1 Studying catalysts . . . 2
- 1.2 Dissertation overview . . . 3

2 Experimental setup **5**
- 2.1 The microreactor . . . 6
  - 2.1.1 Fabrication . . . 8
- 2.2 Anodic bonding . . . 9
  - 2.2.1 The bonding process . . . 9
  - 2.2.2 Pyrex lids . . . 11
  - 2.2.3 Cold bonding . . . 12
- 2.3 Gas handling . . . 15
  - 2.3.1 O-rings . . . 15
  - 2.3.2 The gas wall . . . 16
  - 2.3.3 Mass flow controllers (MFC's) . . . 18
- 2.4 Mass spectrometer . . . 19
  - 2.4.1 Calibration of the mass spectrometer . . . 21
- 2.5 Labview interface . . . 22
  - 2.5.1 Automatization of experiments . . . 23
- 2.6 Pump down experiment . . . 24

3 CO oxidation on Pt thin films **27**
- 3.1 Kinetics of CO oxidation on platinum . . . 27
- 3.2 Experimental results . . . 30
  - 3.2.1 Light off phenomenon . . . 30
  - 3.2.2 Sensitivity of the microreactor . . . 34

4 Methanol synthesis on CuZnO **39**
- 4.1 Methanol synthesis . . . 39
- 4.2 Transient increased reaction rate . . . 40
- 4.3 Experimental results . . . 41
  - 4.3.1 Catalyst deposition . . . 41
  - 4.3.2 Investigation of transient reactivity . . . 42
  - 4.3.3 Formate TPD . . . 48

5 Mass selected Ru nanoparticles **53**
5.1 CO methanation on ruthenium 53
5.2 The nanoparticle source 54
5.3 Experimental results 58
5.3.1 Parameter study 58
5.3.2 Particle size study 60
5.3.3 H_2 TPR 62

6 Other uses for the microreactor **67**
6.1 Photocatalysis 67
6.2 Two phase microreactor 69
6.2.1 Silicon membrane 71
6.2.2 Electrolysis 72

7 Conclusion and outlook **75**

List of included papers

Paper I
Highly sensitive silicon microreactor for catalyst testing
Toke R. Henriksen, Jakob L. Olsen, Peter Vesborg, Ib Chorkendorff, and Ole Hansen
Review of Scientific Instruments **80**, 124101, (2009)

Paper II
Anodic bonding with cooling of heat-sensitive areas
Peter C. K. Vesborg, Jakob L. Olsen, Toke R. Henriksen, Ib Chorkendorff, and Ole Hansen
Review of Scientific Instruments **81**, 016111, (2010)

Paper III
Gas-phase photocatalysis in μ-reactors
Peter C.K. Vesborg, Jakob L. Olsen, Toke R. Henriksen, Ib Chorkendorff, and Ole Hansen
Chemical Engineering Journal **160**:738 - 741, 016111, (2010)

Paper IV
Quantitative Measurements of Photocatalytic CO-Oxidation as a Function of Light Intensity and Wavelength over TiO2 Nanotube Thin Films in μ-Reactors
Peter C.K. Vesborg, Su-il In, Jakob L. Olsen, Toke R. Henriksen, Billie L. Abrams, Yidong Hou, Alan Kleiman-Shwarsctein, Ole Hansen, and Ib Chorkendorff
Journal of Physical Chemistry, Accepted 2010

Chapter 1

Introduction

The topic of this PhD project is heterogenous catalysis in microreactors. The main focus has been the development of a highly sensitive microreactor platform for studying tiny amounts of catalyst under well controlled reaction conditions, and testing the system using a diverse selection of catalytic reactions.

In this chapter a brief introduction of heterogenous catalysis along with the purpose of microreactors is presented followed by a short outline of the dissertation.

1.1 Heterogeneous catalysis

A catalyst is an agent that aids a catalytic process without being consumed in the process, and in the case of heterogeneous catalysis, the catalyst is a solid, and the reactants are either in the gas or liquid phase. In today's society catalysis is of great importance as almost all chemicals produced by the chemical industry are produced using catalyst [1]. Synthesis of ammonia, a key component in the production of fertilizer, for example, is done in the Haber Bosch process, where ammonia is synthesized from N_2 and H_2 with the help of an iron catalyst. Without this process, the world's food production would be significantly lower than what it is today. Catalysis also plays a big role in the current energy sector in processing crude oil and cleaning flue gases from power plants and will likely play a big role in energy solutions for the future, in production of biofuel, photocatalysis, and energy storage.

Industrially, catalysis usually takes place at high temperature and high pressure. Ammonia synthesis, for example, runs at 450-500℃ and 200 bar. The high temperature and pressure makes the synthesis energy intensive and expensive. The ammonia synthesis as

an extreme example uses 1-2% of the world's annual energy supply [2]. This highlights the potential of finding a new and better catalyst, as just a small increase in the performance will affect the global energy consumption significantly.

1.1.1 Studying catalysts

As heterogeneous catalysis happens at the interface between the solid and the gas/liquid, it is naturally a goal to maximize this interface, i.e. the catalyst surface to improve the performance. This is the reason why industrial catalysts in general takes the form of nanoparticles distributed on a porous support [3] to allow the reactants easy access.

When studying a catalytic process, which is a complicated process, a model system is used in order to eliminate some of the complexity and focus on parts of the process individually. Traditionally, this is done by using a ultra high vacuum (UHV) chamber to have a good control of the molecules involved, and by using a singly crystal of the catalyst material to have good control of the atomic state of the catalytic surface. A lot of fundamental knowledge can be gained in such studies, e.g., about the energies involved when a molecule interacts with a catalytic surface and the effect of difference in the morphology of the surface.

The surface of a transition metal catalyst consists of a series of crystallographic planes, and edges and corners at the intersections. A surface atom at a corner will have fewer bonds than an atom on a facet, and it will therefore be undercoordinated. The lack of bonds for the undercoordinated edge and corner atoms makes the interaction energy of adsorbates higher [4]. Thus, disregarding the geometrical difference between surface sites, the electronic state in it self means that there is an effect of changing the morphology of the surface.

That there is a big difference between surface sites was shown by for example Dahl et al. [5], who found a nine orders of magnitude difference in N_2 dissociation rate at steps compared to the close packed surface at 500 K.

For structure sensitive reactions, the size and morphology of the nanoparticle catalyst will have a great influence on the reactivity per total surface area of the catalyst, as the percentage of a given site on the surface will change with the size. For a Wullf constructed [6] nanoparticle the number of corner edge and facet sites will scale to the power of 0, 1, and 2 to the diameter of the nanoparticle down to a size of a few nm.

In recent years catalytic studies has started to shift focus away

from looking at model catalyst in UHV conditions to looking at nanoparticle catalysts at more realistic reaction conditions at a high pressure. What has become apparent is that there is a world of difference between catalysis in UHV and at high pressure, commonly referred to as the pressure gap [7]. This makes it difficult to draw conclusions about high pressure experiments from UHV experiments. One of the main differences between catalysis in UHV and at high pressure is the stability of the catalyst. At high pressure the interaction between the reactive gas and the catalyst can cause changes in the morphology [8, 9], particle migration, sintering, and segregation. This means that a catalyst tested at UHV might look completely different at high pressure. A very promising catalyst tested in UHV, might sinter at high pressure losing activity very fast.

There are several ways to bridge the pressure gap. One way is to study a catalyst using special equipment constructed with the ability to look at a catalyst under reasonably high pressures, such as ETEM[1]. Another route, the focus of this project, is to scale down the reactor used in catalytic testing at realistic conditions to gain better control of the conditions during reaction.

By scaling down a plug flow reactor to a reactor with dimensions measured in μm, a microreactor, several advantages are gained [10–13]. Due to the small dimensions of the microreactor, no significant differences in temperature or partial pressure of a gas are possible inside the microreactor. This gives a better control of the reaction conditions. Furthermore, only a very low amount of catalyst is needed, such that the catalyst can be produced by methods where the degree of control is high, but the production is low. Studying the activity of catalytic nanoparticles as a function of size, e.g., to get information about the active site [14, 15], would normally be difficult because the catalyst nanoparticles are synthesized with a broad size distribution. But using for example e-beam lithography [16, 17] or mass selected clusters from a cluster source [18, 19], a very narrow size distribution can be achieved, making size studies possible. With a high control of the size of the nanoparticles often comes a low production. For this reason, microreactors are a key component in such a study, which is also the main goal of this project.

1.2 Dissertation overview

As a large part of my PhD project was spent on designing, building, and testing the experimental setup used for catalytic experiments

[1] ETEM is a microscopy method designed to study nanoparticles at high pressure.

with the microreactor, a chapter is dedicated to the description of the different parts of the setup, including the microreactor. The design and fabrication of the microreactor was mainly the work of PhD student Toke Henriksen. More information about this can be found in Paper I.

The next three chapters contain information concerning three reactions used for testing heterogeneous catalysis with the microreactor system. The first reaction was CO oxidation on platinum thin films, which was used to test the sensitivity of the microreactor system. The second reaction was methanol synthesis on an industrial catalyst. This system was chosen to take advantage of the fast time response of the system to look at the dynamic behavior of the catalyst under changes in gas composition. The third system was CO methanation on mass selected ruthenium nanoparticles, with the goal of studying the reactivity as a function of the size of the nanoparticles.

The microreactor system was also used for photocatalysis and a special two phase microreactor for electrolysis was developed. Both uses are described in chapter 6. After the initial testing, most of the work with photocatalysis in the microreactor was done by PhD student Peter Vesborg, why only a short introduction to the subject is included. More information can be found in Paper III and Paper IV.

Chapter 2

Experimental setup

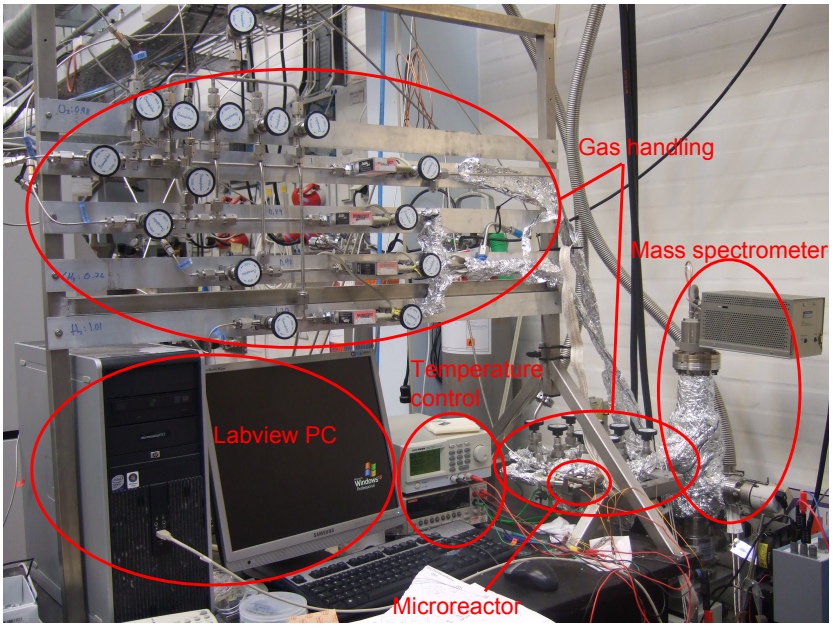

Figure 2.1: *Picture of the experimental setup with the different parts marked.*

In this chapter I will describe the different parts of the experimental setup shown in Fig. 2.1. Starting with the microreactor chip, the ideas behind its design, a description of its function, and a brief introduction to the fabrication process. A section will follow with information about seal the microreactor chip is sealed by anodic bonding, and a description of a special low temperature version of the anodic bonding that was developed. The rest of the chapter contains sections describing the other parts of the experimental setup: the gas handling, the detection by quadrupole mass spectrometer

(QMS) and the computer interface written in LabVIEW used to control the experimental setup.

2.1 The microreactor

The basic design of the microreactor is similar to a conventional plug flow reactor, only on a very small scale. The aspect that differentiates our design from more standard designs, is the placement of the main flow outlet before the reaction chamber instead of after as shown in Fig. 2.2. This has the important effect of changing the flow in the reaction chamber by orders of magnitude, from the level of the main flow, in the order of 10 mL/min in our case, to the level of the detection flow, around 10^{15} molecules per second ($\sim 2 \cdot 10^{-3}$ mL/min). At the same time the flow to the detection in the mass spectrometer is kept the same. By changing the flow design the sensitivity is increased several orders of magnitude. Another consequence of this design, is that it makes the flow in the reaction chamber a fixed number which can only be varied by changing the microreactor to one with different physical dimensions. Furthermore, the flow will be pressure and temperature dependent be discussed in section 2.6

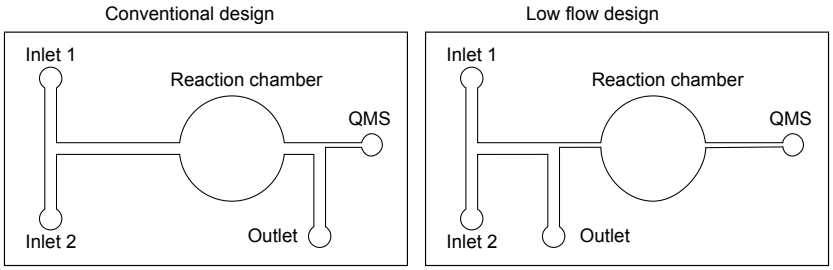

Figure 2.2: *Sketches of the flow channel design of a conventional plug flow reactor and the low flow design used for the microreactor. In the conventional design a large flow will pass through the reaction chamber and a small part of the output will be sampled for detection in the QMS. In the low flow design the sampling happens before the reaction chamber, such that every single reaction product will go to detection in the QMS, thereby increasing the sensitivity by orders of magnitude.*

Figure 2.3 shows a picture of the finished microreactor, where the different features can be seen. The four holes at the top are the gas connections to the gas handling system. The flow enters the microreactor chip through the two leftmost holes, which are the inlet holes for the main flow enabling gas mixing directly on the chip. The advantages of mixing the gas directly on the chip is that because the

dimensions are so small, the time delay is very short (seconds) and diffusion is the only source of contamination from the closed channel.

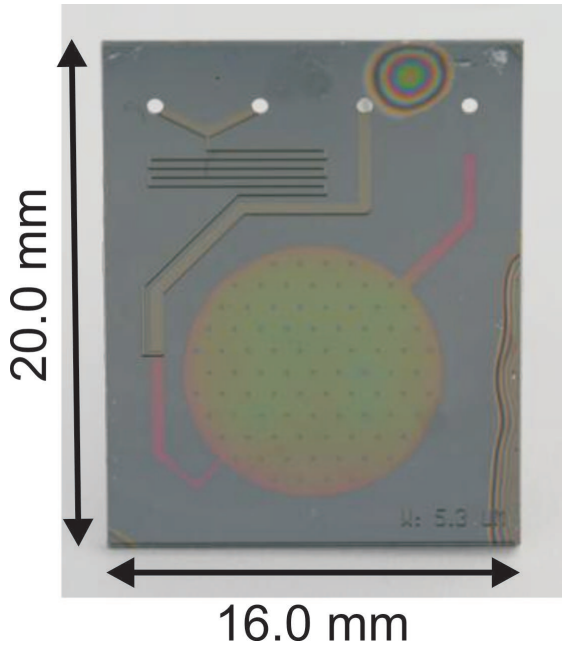

Figure 2.3: *Picture of a microreactor chip after it has been closed by anodic bonding of a pyrex lid. The four through holes at the top are connections to the gas handling system, two inlets, one outlet, and one connection to the QMS. The clearly visible main flow channels are 250 μm deep and the hard to see reaction chamber is 3 μm deep. The small dots seen in the reaction chamber are support pillars ensuring the pyrex lid does not collapse during bonding.*

After the two inlet channels are joined comes a long thin meander structure designed to cause perfect mixing of the two gas flows. This is necessary because the flow is laminar, such that mixing can only be caused by diffusion. Following the meander structure is the point where a small amount of the gas enters the reaction chamber before the rest is led directly to the outlet for the main flow (hole number three from the left). The flow in the reaction chamber is limited by the narrow capillary between the reaction chamber and the outlet to the mass spectrometer (hole number four from the left) which creates a pressure drop from around 1 bar in the microreactor to around 10^{-6} mbar in the mass spectrometer and a corresponding flow in the order of 10^{15} molecules per second.

Two versions of the microreactor were produced, where the only difference was the width of the capillary of either 5.6 μm or 54.5 μm, which resulted in a factor 10 difference in the flow. The narrow

channel is advantageous if a low reaction yield is expected, and the wide channel is advantageous if a fast response time is needed (the residence time will be lower), or a high conversion is expected.

2.1.1 Fabrication

The microreactors are fabricated in the cleanroom facility at Danchip DTU using standard microfabrication processes. The sequence of process steps are shown in Fig. 2.4 where the starting point is a 350 μm thick 4″ silicon wafer, a well suited microreactor material [20].

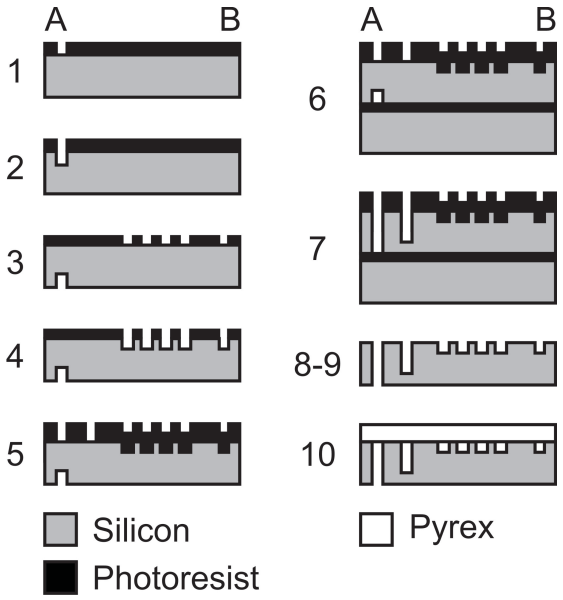

Figure 2.4: *Sketch of the microprocessing steps involved in the fabrication of the microreactor chips from a 350 μm 4″ silicon wafer.*

First, the 3 μm deep structures such as the reaction chamber and the capillary channel are etched in a Reactive Ion Etch (RIE) process, with the pattern defined in a polymer using UV-lithography. Afterwards, 100 μm of the through holes are etched from the back side followed by a front side etch of the main flow channels to a depth of 250 μm connecting to the partially etched through holes. Both these etches are performed using a Deep Reactive Ion Etch (DRIE) [21], again with the patterns defined using photolithography. Furthermore, for the final etch the wafer being processed is bonded to a handle wafer. This is done to avoid the etch of the through holes connecting the backside and the front side of the wafer stack, which is not allowed in the machine for DRIE. Finally the wafer is thermally oxidized with an oxide of ∼50 nm to make the surface

chemically inactive and nonconducting and the wafer is sawn into 16 chips with one microreactor each.

2.2 Anodic bonding

Before the silicon chips can be used as microreactors the etched patterns have to be closed off by a lid to form channels and a reaction chamber.

As a lid for the microreactor a pyrex lid is anodically bonded (also called mallory bonding [22]) to the silicon chip. This method has several features which makes it very suitable for our purpose. First of all, it creates a strong and hermetic seal [23]. This is a very important aspect when testing small amounts of catalyst, as even low amounts of contaminants can change the results drastically. For the same reason, it is important that the bonding method is chemically clean, in the sense that there is no vapor pressure of foreign elements as there would normally be if a glue was used. Finally, anodic bonding of pyrex to silicon is quite forgiving to small particles on the bonding surfaces [23, 24]. This is helpful as some forms of catalyst deposition can easily result in small deposits on the bonding surfaces. The big disadvantage of this method is the high temperature needed during bonding of around 300℃. Which, depending on the catalyst, can for example cause detrimental sintering of the catalyst.

2.2.1 The bonding process

A sketch of the setup we have used for anodic bonding is shown in Fig. 2.5. This is how the stack of the microreactor chip and pyrex lid is placed after the bonding surfaces has been cleaned by air duster and ethanol wipe. The hotplate is used to heat the stack to 300-350℃, necessary for making the pyrex lid conducting by ionic transport of Na^+ ions [25]. When a bonding voltage of -1 kV is applied to the point cathode on the heated stack, the voltage drop is over the gap between the silicon and pyrex. Huge electrostatic forces around areas of physical contact are created as a result of the small distance and thereby huge electric fields [23, 24]. This has the effect that the area pressed together and bonded slowly spreads across the whole chip, as can be seen in Fig. 2.6. After the bonding is complete and the temperature and voltage has been turned off, the bond will persist. Not only electrostatic forces from the migrated ions keep the reactor and the lid together, but chemical bonds are created between the SiO_2 and the pyrex. The bond is very strong and the reactor

can not be opened again afterwards. We have tested the stability of the reactor to high pressure by increasing the pressure inside the reactor to 7 bar, which is the highest our setup can currently supply, and there were no problems with the reactor breaking open.

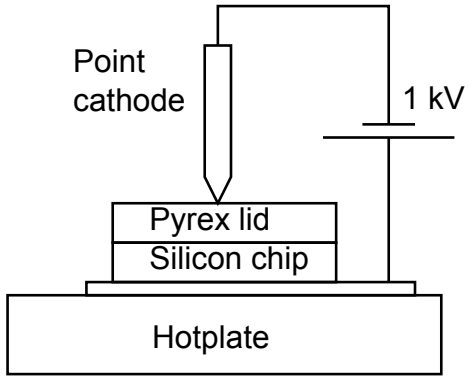

Figure 2.5: *Sketch of the setup used for anodically bonding the pyrex lid to the silicon microreactor. The pyrex silicon stack is heated to 300-350°C and a -1 kV potential is applied to the point cathode. During the bonding process of approximately 30 minutes depending on the temperature, a current of a few mA passes through the stack.*

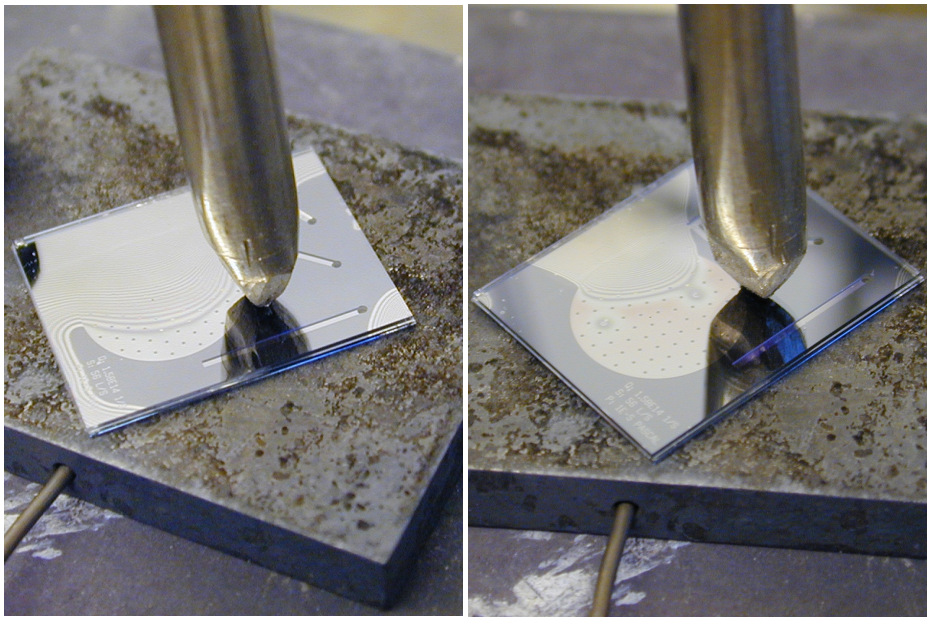

Figure 2.6: *Pictures of the anodic bonding process. The dark area where the features of the microreactor are clearly visible and is spreading from the first to the second picture, is the bonded area. The pattern seen in the unbonded region is the diffraction pattern from the gap at the interface between silicon and pyrex.*

The strong bond also means that it is impossible to open up the reactor to study the catalyst inside the reaction chamber by microscopy or surface sensitive spectroscopy methods. After use the reactor can be broken apart to study the catalyst, but then it cannot be used again.

2.2.2 Pyrex lids

Besides a bare pyrex lid made by sawing a 0.5 mm thick 4″ wafer into 16 pieces with the dimensions 16 times 20 mm to fit perfectly with the silicon reactor chips, we also produced a series of lids with integrated electrodes in the form of metal thin films structured on the lids. Of the lids with electrodes, we have have primarily used a lid with the dimensions 16 times 32 mm allowing room for contact pads.

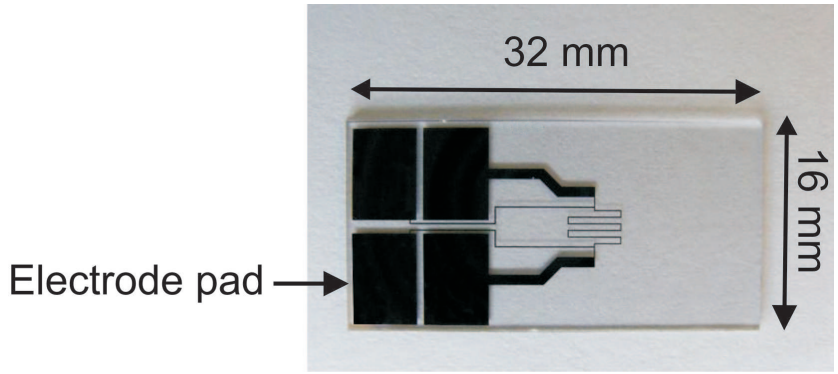

Figure 2.7: *Picture of a pyrex lid with a platinum thin film RTD. The resistance of the meander structure, which will be placed over the reaction chamber, can be measured accurately in a four point measurement using the four electrode pads. The resistance of the structure is approximately 470 Ω.*

The electrodes are made from 100 nm Pt thin films[1] structured as shown in Fig. 2.7 by a photolithographic lift off process. This serves the purpose of a resistance temperature detector (RTD), where the resistance of the central platinum meander structure can be used to determine the temperature in the reactor. By making a four point measurement of the resistance during experiments and converting the resistance into temperature as described in section 2.5, the temperature inside the reactor can be monitored very accurately[2].

[1] A 10 nm Ti film is used as an adhesion layer.

[2] In a test of the sensitivity of the RTD, a lid was produced with and RTD structure on both sides. By changing the gas mixture from an inert gas to a CO plus O_2 gas mixture, a roughly 0.1℃ temperature difference of the RTD inside the reactor was seen.

Some examples of similar Pt thin film structures used for electrodes have also been used for electrochemical testing as described in section 6.2.2.

2.2.3 Cold bonding

As discussed earlier, the high temperature needed for anodic bonding is detrimental to some catalysts, and was especially an issue for us when using the microreactor for photocatalysis (see section 6.1). For photocatalytic testing the reaction was run at room temperature, and the bonding temperature by far was the highest temperature the catalyst was subjected to. Thus, some work was put into finding a different method for bonding which did not subject the catalyst to as high a temperature.

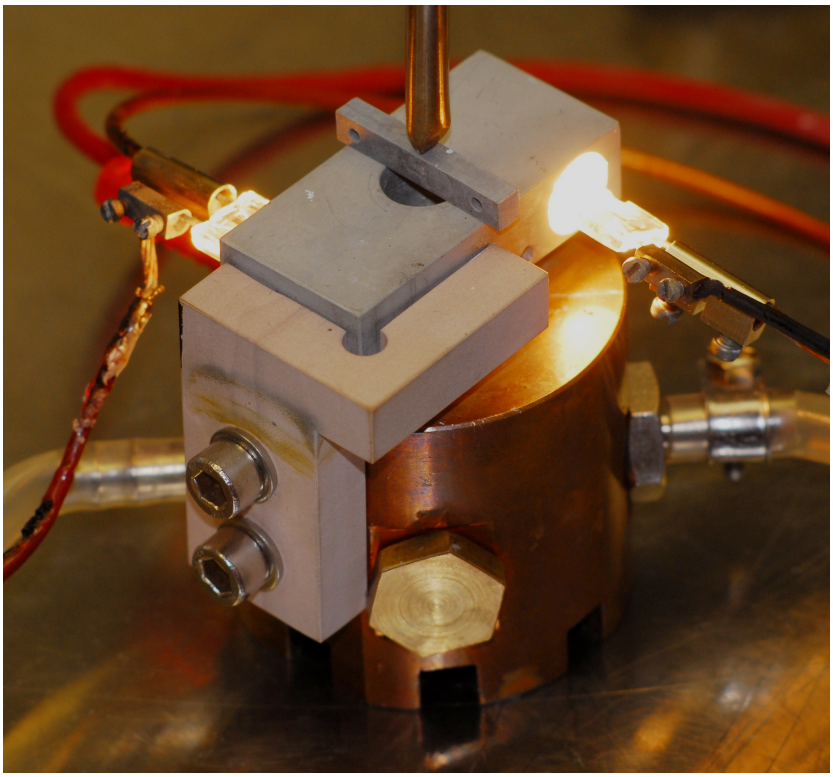

Figure 2.8: *Picture of the cold bonding setup while in the process of bonding. The block fixed with screws to the copper block is made from a ceramic and is there to fixate the aluminum block*

The method we developed relies on the fact that the high temperature is only needed for making the pyrex lid conducting and only in the region where the lid has to be bonded. With that in mind, we

came up with a method where the heating was done from the pyrex lid side in the region where the bonding was necessary i.e. not in the reaction area. At the same time the reaction area (where the heat sensitive catalyst is located) was cooled from the silicon side. The setup is shown in Fig. 2.8.

In short the reactor is placed on a small pedestal of copper on a larger block which serves as the cooling part of the setup. This block is kept cold by a continuous stream of cold water led through the block, such that the temperature of the block is kept at around 10℃ during bonding. An aluminium block with two cutouts for two 150 W incandescent light bulbs and a cut out to avoid heating the reaction chamber, is used to heat the pyrex lid and serve as the cathode. The block is heated to around 475℃ during bonding (happens at around 20 A through the two light bulbs). This method results in the heat profile shown in Fig. 2.9 in the bonding setup according to simulations. By using a lid with an RTD, the temperature inside the reaction chamber was monitored during bonding. The result shown in Fig. 2.10 agrees with the simulations, with a temperature of below 50℃ in the main part of the reaction chamber, a huge improvement from the previous 300-350℃.

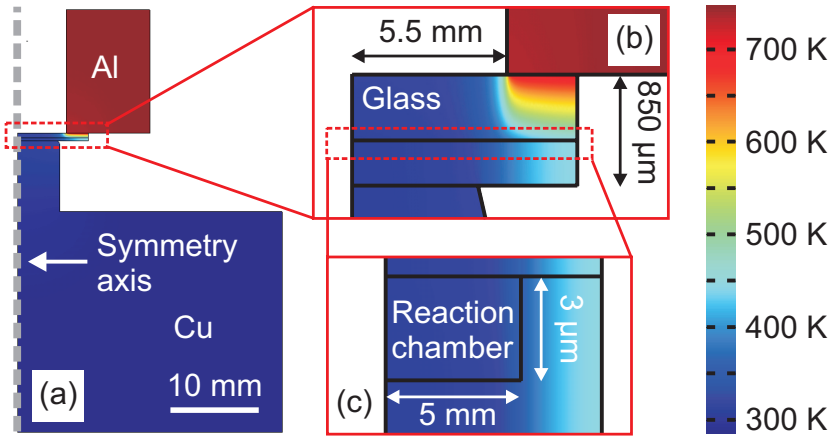

Figure 2.9: *The result of a finite elements simulations of the temperature throughout the cold bonding setup while bonding. The heat flow from the cathode vertically through the pyrex lid and radially in the silicon chip, causes large temperature gradients across the pyrex lid, making bonding of the outer regions possible, while the reaction chamber is mostly kept below 50℃.*

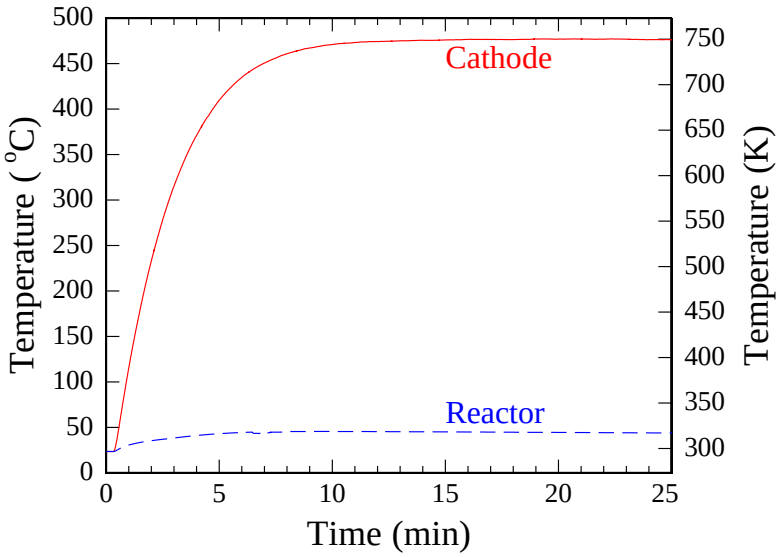

Figure 2.10: *The temperature of the aluminum cathode and the inside of the pyrex lid over the reaction chamber measured during bonding in the cold bonding setup.*

2.3 Gas handling

One of the challenges with our microreactor system was to interface the microreactor chip made of silicon with standard gas handling equipment in stainless steel. The solution we used rely on designing a gas manifold in stainless steel as sketched in Fig. 2.11 which was machined by our workshop.

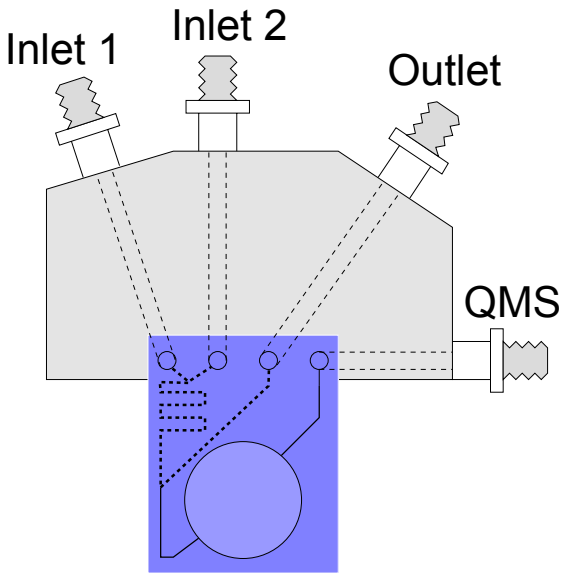

Figure 2.11: *Sketch of the steel gas manifold interfacing the microreactor with the gas handling system. Gas tight connections between the silicon reactor and the steel block is ensured by O-rings. The interconnections to the gas system comes from four VCR fittings.*

Four VCR (swagelok) fittings were welded to the block, making connections to the rest of the system possible, which has been kept in $1/4''$ stainless steel tubing with VCR fittings, copper gaskets, and needle valves from Swagelok.

2.3.1 O-rings

Getting a leak tight connection between the steel block and the silicon microreactor proved to be one of the bigger challenges. A previous version of the setup had used Viton perflourelastomer O-rings which had two issues. They were only temperature resistant up to around 200℃. at which point the elastomer becomes hard and the O-rings start leaking, and diffusion through the O-rings of atmospheric air was significant. Gold O-rings were tested as a soft metal for sealing, which would eliminate both the temperature and

diffusion problem. Unfortunately, we never got the gold O-rings to seal properly. The problem was that even though gold is soft, it still takes a significant force to deform the gold, and the microreactors are brittle and break easily. If some form of knife edge were to be made in the silicon surface, the gold O-rings could probably be made to work, but would still have had to be replaced after use, making the solution less practical and the fabrication of the microreactor more complicated. The solution we ended up with was switching material to Kalrez, a more temperature resistant material making experiments above 200℃ possible. To limit the effect of the diffusion leak, we designed a system allowing a continues flush of argon in the region surrounding the O-rings, replacing at least 99% of the air leak with an argon leak. Out of the four O-rings, only the one at the mass spectrometer outlet has a low enough pressure on the other side for the diffusion through the O-rings to have an effect. Therefore, the problem with the leak was only with interpreting the signals in the mass spectrometer complicated by the addition of extra signals, not with leaks inside the reaction chamber. By replacing the leak from air to argon it was easier to account for, by simply subtracting argon signals in the mass spectrometer as a background. It has to be noted that the diffusion leak was only a big problem at elevated temperatures where the diffusion rate through the elastomer was high. For experiments at room temperature the leak was low enough to be ignored in many experiments.

2.3.2 The gas wall

Figure 2.12 shows a sketch of the gas wall. The gas wall makes it possible to mix up to four different gases in a wide range of compositions into the two inlets on the microreactor at any pressure set by the pressure controller. Our current pressure controller allows pressures between 0.1 bar and 2.5 bar.

The setup can be divided into three parts. A gas supply part, a gas mixing part, and a microreactor interface part. The design of the gas supply has two functions: 1) it makes changing gas in one of the four lines fast with no problems with cross contaminations of the gases. Because of the access to a pumping line, the need for long flush periods to clean a line is eliminated. 2) it makes it possible to use one gas on several lines at the same time by passing it through the pump line manifold, this is useful if for example a trace gas is needed in both inlets on the microreactor.

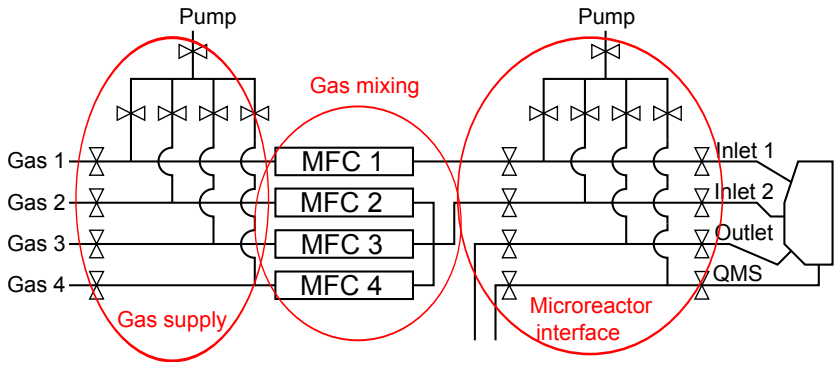

Figure 2.12: *Sketch of the gas wall used for supplying the microreactor with the desired gas mixture and pressure.*

The mixing part, consisting of four lines with mass flow controllers (MFC's) combining into two lines, is as the name implies for mixing the gases into the composition wanted. As the overall flow is not important[3] the four flow rates can be chosen almost freely in order to get the wanted composition of gases. The total flow is limited by two factors: 1) with a low flow rate, it will take a long time to change the gas in the feed line. 2) with a high flow rate, the small dimensions of the microreactor will cause a significant pressure drop. What exactly these limits are depend on the pressure in the system, as changes in pressure changes the volume of a given flow of gas. Normally a flow of 10-20 mL/min is the best choice for experiments at 1 bar.

The gas lines connecting the manifold block interfacing with the microreactor are similar to the system for the gas supply, with the four lines being the two inlets and the outlet for the main flow in the microreactor, and the connection to the mass spectrometer. But, here the connections to a pump is more important, as it is used each time the microreactor is changed. Most importantly on the line connecting to the mass spectrometer. Pumping this line down to around 1 mbar makes it less of a problem to open up from high pressure into the UHV chamber containing the mass spectrometer. This is something you normally want to avoid if possible as it increases the background pressure in the UHV chamber. Secondarily, it is also used on the other lines to remove the atmospheric air from the gas handling system, which enters the system when changing the microreactor. Thus shortening the time it takes for the setup to stabilize with a certain gas flow. As a final note, the outlet of the pressure controller is also connected to a pump. This makes running experiments not

[3]The flow in the reaction chamber is determined by the capillary, and not the overall flow.

only at elevated pressure but also at below 1 bar possible, the limit is around 0.1 bar, where our current pressure controller can still control the pressure well.

2.3.3 Mass flow controllers (MFC's)

In our setup we use four MFC's from Bronkhorst with maximum flow rates of 1, 7.5, 20, and 25 mL/min which can operate down to 2% of full scale. This means two gases can be mixed in ratios from 1:1 up to 1:1250 opening up for a wide range of gas mixtures.

The mass flow controllers measure the flow by measuring the temperature at two points while the gas passes through the controller. In between these two measurements a heating element supplies a constant heat flow to the gas. The change in temperature, ΔT, can then be converted to a flow, F, as $F = \frac{\mathrm{d}Q}{\mathrm{d}t} \cdot (\Delta T^{-}1 \cdot c_P \cdot \rho)$, where c_P is the specific heat of the gas, and ρ is the density. The measurement of the flow is then used as a feedback to control a valve that can be opened or closed to change the flow to a given setpoint. One thing to note about the way the controllers measure the flow, is that it does not measure the actual volume of the gas passing through in a giving time, but the heat capacity of that volume of gas. Thus, a correction for the heat capacity per volume of a given gas has to be taken into account. Table 2.1 contains the conversion factor for gases used in this project, when converting from one gas to the other.

N_2	1
He	1.41
CO	1
O_2	0.98
H_2	1.01
CO_2	0.74

Table 2.1: *Table containing the inverse of the values for $c_P \cdot \rho$ relative to N_2 needed for setting the correct flow setpoint on the MFC's for gases used in this project.*

Furthermore, to correct for the possible drift the MFC's may have had in their settings over the years, they were calibrated with respect to each other. It was not necessary to calibrate them in absolute numbers since the flows are only used to create a specific gas mixture. They were calibrated by setting each individual controller to a flow one at a time and letting that flow slowly fill up the volume in the tubing between the MFC's and the pressure controller while measuring the pressure. Since the volume is the same, the relative

flows can be found from the slope of the pressure as a function of time. The result of such an experiment can be seen in Fig. 2.13.

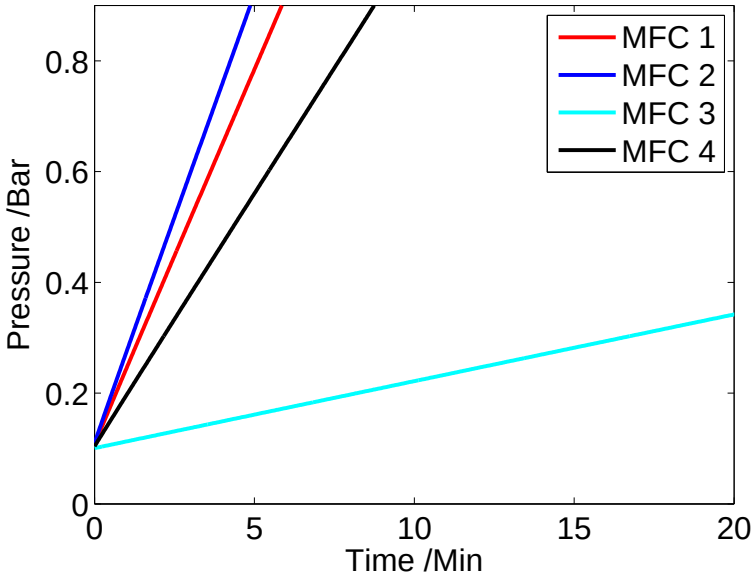

Figure 2.13: *The result of a calibration experiment for the MFC's. The four flow controllers were given setpoints of 10, 7.5, 1, 10 mL/min and the pressure of the gas system was measured while it was filled. Calibration with respect to flow controller one gives the following values for the correction: 1.00, 0.89, 0.90, 1.20.*

To figure out which setting has to be used for the MFC, F_{set}, to get an actual flow, F_{real}, in mL/min out, the following equation can be used:

$$F_{set} = \frac{F_{real}}{k_{cal} \cdot c_P \cdot \rho}, \tag{2.1}$$

where k_{cal} is the correction found in the calibration and $c_P \cdot \rho$ is the correction for the heat capacity found in table 2.1. Which means that if a flow of 5 mL/min of H_2 from flow controller 4 is wanted, the set point has to be set to $\frac{5 \cdot 1.01}{1.2} = 4.21$.

2.4 Mass spectrometer

The mass spectrometer used for detecting all the components of the gas passing through the microreactor is a quadrupole mass spectrometer from Balzers (QMA 125). It works as sketched out in Fig. 2.14 [26], where the gas enters to the left, is ionized by the

electron emission from the hot filament. The now positive ions are accelerated through the quadrupole mass filter, which only allows ions of a specific mass to charge ratio to pass through. Finally, the ions passing through are measured using the Secondary Electron Multiplier (SEM), which through electron cascades from the supplied SEM voltage (in our case 2kV) can be measured as a current, usually in the order of 10^{-14} to 10^{-6} A. The mass filter works by supplying the four poles, cross pair wise, with a DC voltage and a high frequency AC voltage at around 2 MHz. By changing the amplitude of the high frequency voltage, the trajectories of the ions can be tuned to allow a specific mass to charge ratio to pass through. To measure for example the amount of oxygen, the filter is set to let ions with 32 atomic mass units per charge pass through (from now on referred to 32 AMU).

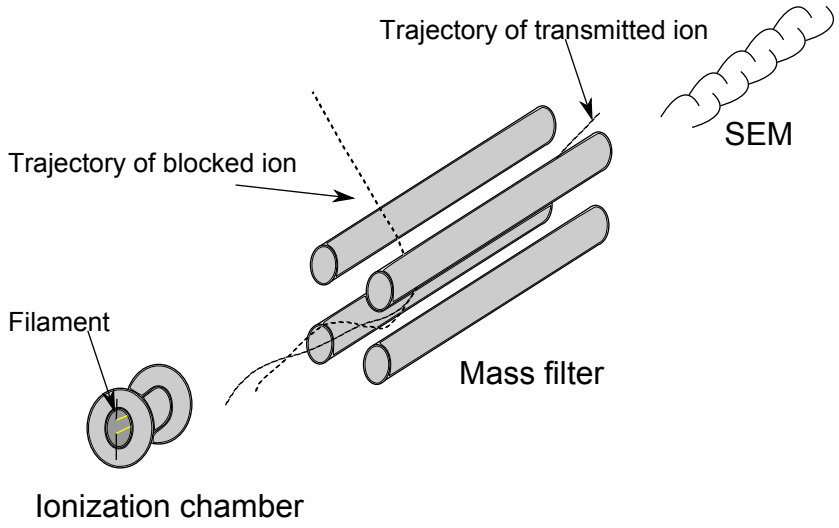

Figure 2.14: *Sketch of the mass spectrometer. An ionization chamber where the electron emission from the filament ionize the gas. The mass filter where the electric field caused by the supplied voltage on the four poles determines the trajectory of the incoming ions. Unwanted masses of the ions will be sent out of the path, and the correct masses will have trajectories transmitting them to the SEM, where they are measured.*

There are a couple of effects which has to be taken into account when analyzing the signals, which makes it a bit more complicated. First of all, the ionization cross section of different gas molecules are not the same, this is something that can be looked up, but since the cross section depends on the exact setup, the best is to do a calibration. Secondly, every molecule has a fingerprint of AMUs where it can be detected. For example CO will have a main peak at

28 AMU, but in the ionization process the molecule can split into a C and an O atom, measured at 12 AMU and 16 AMU. Furthermore, the natural isotope of carbon C^{13} creates peaks at 29 AMU and 13 AMU. Also if a molecule gets double ionized in the ionization process, it will be detected at half the AMU, for CO that means a peak will appear at 14 AMU. Secondary effects such as measuring a split off double ionized C atom at AMU 6 are unlikely enough that they can usually be disregarded. But, with more complex molecules as for example ethanol, a quite large fingerprint still exists.

2.4.1 Calibration of the mass spectrometer

To convert a signal measured in the mass spectrometer to the number of molecules per second of a given gas flow coming from the microreactor, a couple of calibration experiments are needed. First of all, the total flow through a microreactor has to be found. An experiment doing this for atmospheric air is described in section 2.6 with the result that $6 \cdot 10^{14}$ molecules exits the reaction chamber of that specific microreactor per second at room temperature.

Once the flow of one reference microreactor has been found, F_{ref}, the flow of another, F, can be found by comparing the mass spectrometer signal of any gas using the two microreactors, as the signals are proportional[4] to the number of gas molecules per second in the flow. Thus: $F = \frac{I}{I_{ref}} F_{ref}$, where I is the ion current measured.

Once the total flow is known, the sensitivity of the mass spectrometer to the individual gases can be found. If for example we want to find the sensitivity for helium, a known mixture of a small amount of $X_{\%}$ helium in N_2 is passed through the microreactor[5], such that the helium flow is:

$$F_{\mathrm{He}}^{ref} = X_{\%} \cdot F, \tag{2.2}$$

and thus the calibration constant for helium C_{He} is:

$$C_{\mathrm{He}} = \frac{F_{\mathrm{He}}^{ref}}{I_{\mathrm{He}}^{ref} - I_{\mathrm{He}}^{0}}, \tag{2.3}$$

where I_{He}^{0} is the background signal measured at 4 AMU before starting the flow of helium. Once the signals for the gases of interest has been calibrated for any microreactor, the same constant is valid

[4] At very high pressures, above $1 \cdot 10^{-5}$ mbar some nonlinearity might appear as the space charge of the ionized gas can start to interact with the individual ions.

[5] The reason for using a small amount of helium in N_2 is that the flow through the capillary of the microreactor depends on the molecular mass as discussed in section 2.6, and the flow was found for atmospheric air, thus this gas mixture will have a very similar flow.

no matter which microreactor is used. Thus, the number of molecules passing through per second of gas x, F_x can be calculated as:

$$F_x = C_x \cdot (I_x - I_x^0). \tag{2.4}$$

Of course, matters will sometimes be complicated by the fact that several different molecules give signals at the same AMU, but here the fingerprint of the molecules can be used to choose an AMU which is not the main peak for a measurement or at least to differentiate the signals.

2.5 Labview interface

The control and data collection of the different parts of the experimental setup, such as the MFC's, the pressure controller, the temperature control, and the mass spectrometer are all done from a single PC using a program written in LabVIEW. The LabVIEW program interfaces mainly through a couple of DAQ-cards. There are two main reasons for controlling everything through a single program like this. It makes data collection a lot easier, as all the parameters of the setup monitored constantly can be put into a single data file with no timing issues when comparing data from different sources. It also makes scripting of the setpoints of the setup possible, which means the experiments can be automated.

The MFCs and the pressure controller are operated by a 0-10 V analog signal for a flow/pressure between 0 and maximum. In the same manner the actual flow/pressure can be read by an analog 0-10 V signal. All communication with the PC happens via the DAQ-cards. The temperature is measured using the pyrex lids with integrated RTD or if not possible, by a thermocouple. The resistance of the platinum RTD, measured in a four point measurement by a multimeter, can be converted into a temperature as long as the resistance at any temperature is known. The resistance, R, of platinum as a function of temperature in Celsius, T, can be found from this equation [27]:

$$R = R_0 \cdot \left(C_1 \cdot T + C_2 \cdot T^2 + 1\right), \tag{2.5}$$

where $C_1 = 0.00381\ ^\circ\mathrm{C}^{-1}$ and $C_2 = -6.02 \cdot 10^{-7}\ ^\circ\mathrm{C}^{-2}$. The resistance at 0℃, R_0, depends on the exact dimensions of the platinum meander, but is usually within 70 Ω of 470 Ω. This means that before an experiment, the resistance at room temperature measured is typed into the program, and from then on the resistance can be converted

into temperature. If the platinum thin film RTD has not been annealed beforehand, the value of R_0 can drift a bit during heating [28], which is why it is best to anneal it first. The microreactor is heated by a resistive heating element pressed to the backside of the reaction chamber. As the output of the power supply connected to the heating element is controlled by the PC, a PID[6] algorithm with the measured temperature and the temperature setpoint as inputs, can regulate the temperature with changes of up to 1℃/s and fluctuations of less than 0.1℃. Communication with the multimeter for the four point resistance measurement is done via GPIP and with the power supply via serial communication.

2.5.1 Automatization of experiments

Controlling everything on the setup, except the valves from a LabVIEW program on the PC, opens up the possibility of automating experiments by writing scripts for the setpoints for the MFCs and the temperature. Automating the experiments makes it possible to use the setup more efficiently as experiments can run during the night or over the weekend. Furthermore, it removes the human factor when running experiments, which means it is possible to get the exact same timings and therefore reaction conditions for a series of experiments, making comparisons between results easier. If does take some planning to run experiments automatically, as no corrections can be made on the fly. If for example it takes longer for the microreactor to cool down than expected, the next part of the experiment might be run at too high a temperature. But as it is not necessary to be at the setup while an experiment is being run, the time spent planning is time well spent.

[6]Proportional Integral Differential

The scripts needed for controlling the setpoints of for example the temperature is written in standard programming code. A script for four consecutive temperature ramps from 50 to 400℃ with a rate of 1℃/s and 5 minutes of cooldown time could look like this:

```
if(t<(350+300)*4){
    while(t>650)
        t = t - 650;
    if(t<350)
        T = 50 + t;
    else
        T = 50;
}else
T = 0;
```

Almost all the measurements performed in this project has been done using scripts like these. Some examples of results from experiments using much more complex scripts lasting several days can be found in section 5.3.

2.6 Pump down experiment

A key feature of the microreactor is the capillary connecting the reaction chamber and the outlet to the mass spectrometer, as the dimensions of this channel determines the flow through the reaction chamber and thereby also the pressure in the mass spectrometer. Since the mass spectrometer is best operated at pressures between $1{\cdot}10^{-7}$ and $1{\cdot}10^{-5}$ mbar, it is important that the capillary is produced with the correct dimensions.

The capillary has a length of $l = 1500$ μm and a cross section of 5 times 3 μm. By treating it as having a circular cross section of the same area, i.e. with a diameter of $d = 4.4$ μm, an analytic expression of the flow can be found. This flow turns out to transition from the intermediate to molecular flow regime partway through the capillary, resulting in a set of equations determining the flow of molecules, F, analytically:

$$F = c\frac{p_1 - p_2}{k_B T}, \tag{2.6}$$

with

$$c = \frac{\pi}{128}\frac{\bar{p}d^4}{\eta l} + \frac{1}{3}\sqrt{\frac{\pi}{2}}\frac{d^3}{lv}\frac{1 + \frac{dv\bar{p}}{\nu}}{1 + 1.24\frac{dv\bar{p}}{\eta}}, \tag{2.7}$$

for the intermediate flow regime [29], where p_1 and p_2 are the pressures at the start of the channel and at the transition point between intermediate and molecular flow, $\bar{p} = \frac{p_1 - p_2}{2}$, η is the viscosity of the gas, and $v = \sqrt{\frac{m}{k_B T}}$. For the molecular flow regime [30]:

$$F = \frac{1}{3}\sqrt{\frac{\pi}{2}}\frac{d^3}{lv}\frac{p_2 - p_3}{k_B T}, \tag{2.8}$$

where p_3 is the pressure at the exit of the capillary channel. By combining the two equations and eliminating p_2 the flow as a function of pressure difference across the capillary is found.

To verify the theoretical calculations an experiment was set up to measure the flow as a function of pressure. This was done by closing off the two gas inlets with blinds and the outlet with a baratron, such that the flow through the capillary[7] would slowly empty the closed gas volume of 11.2 mL in the steel gas manifold. By monitoring the pressure measured by the baratron as a function of time, the flow could be calculated. Figure 2.15 shows a plot of the pressure as a function of time as it was measured and a plot of the flow as a function of pressure from the measured data together with the calculated flow from the analytical expression in equation (2.6) and (2.8). A good agreement between the measurement and the calculation is seen. Extrapolating the data up to 1 bar, a flow of $6 \cdot 10^{14}$ molecules per second is found. As this experiment was performed with atmospheric air, the flow of molecules with a different molecular weight will vary as can be seen by equation (2.6). In the same manner the flow will also vary as a function of the temperature of the gas, something that has to be taken into account when making experiments at different temperatures.

[7] A microreactor with a narrow capillary was used, even though a wide capillary would have tested a larger pressure range in the same time because of the larger flow.

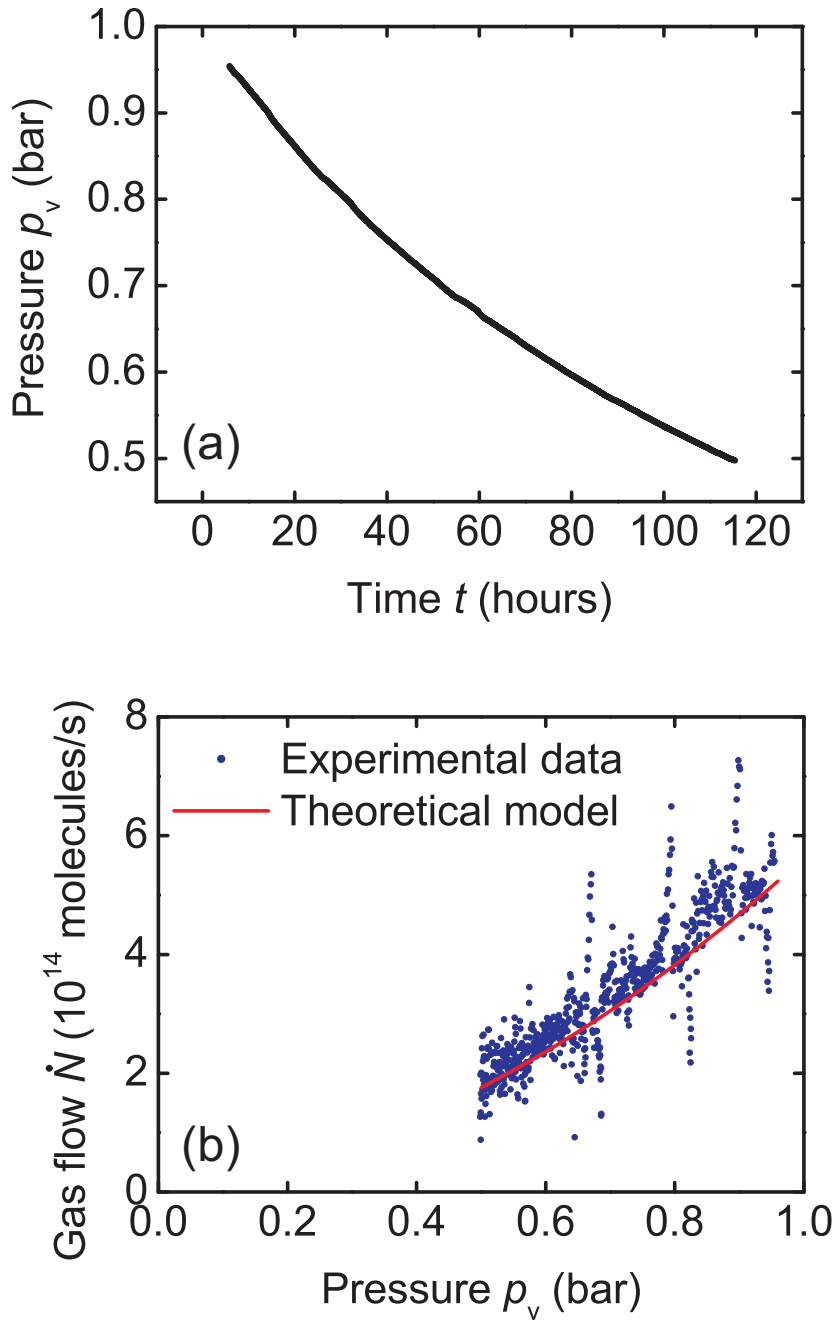

Figure 2.15: *(a): The pressure measured as a function of time as the closed volume of 11.2 mL in the steel gas manifold is emptied of gas through the narrow capillary in the microreactor. (b): The measured pressure as a function of time converted to molecular flow together with the prediction from the theoretical modal for a channel with the dimensions of the capillary.*

Chapter 3

CO oxidation on Pt thin films

To test the performance of the microreactor system, we chose CO oxidation on platinum as the first test reaction. This reaction was chosen for two main reasons, it is a reaction that has been studied a lot and the kinetics of the reaction is therefore quite well understood. Thus, it is easier to predict what will happen and possible to compare with previous studies. Furthermore, CO oxidation on platinum was chosen because it is a relatively simple reaction in the sense that there is not a lot of reaction products or intermediates to account for.

This chapter will start with a short introduction to CO oxidation on platinum and the kinetics governing the reaction. The following two sections will focus on the results from testing. One section about the light off phenomenon and one about a study of the sensitivity of the microreactor system, where measurements with as little catalyst as possible were performed.

3.1 Kinetics of CO oxidation on platinum

The reaction between CO and O_2 catalyzed by platinum is known to proceed through a Langmuir Hinshelwood mechanism [1], where CO adsorbs on the platinum surface along with O_2 that adsorbs dissociatative. The adsorbed CO and O reacts and the produced CO_2 desorbs without a barrier. The four reaction steps can be written as:

$$CO + * \rightarrow CO^* \tag{3.1}$$
$$O_2 + 2* \rightarrow 2O^* \tag{3.2}$$
$$CO^* + O^* \rightarrow CO_2^* + * \tag{3.3}$$
$$CO_2^* \rightarrow CO_2 + *, \tag{3.4}$$

where * denotes a surface site.

When dealing with platinum catalysts in flow reactors where the gas flow consists of CO and O_2, the platinum surface can be said to be in one out of three possible states depending on the reaction conditions: CO poisoned, saturated with O, or low coverage.

CO poisoned: In this case the surface is almost fully covered with CO. The reactivity is low and dominated by the lack of sites for O_2 to adsorb. This state appears at low temperatures when there are decent amounts of CO present in the gas phase. It is caused by the difference in probability of a CO molecule and an O_2 molecule adsorbing when colliding with a highly saturated surface, as O_2 needs two free sites to adsorb.

Saturated with O: To get the surface fully saturated with O, only trace amounts of CO can be present in the gas phase, as each CO molecule will have an almost 100% chance of reacting with an O atom creating two new empty sites with even higher chance of another CO molecule to adsorb and react, thus accelerating the process removing the O from the surface.

Low coverage: In this state the coverage of both CO and O us low. The reactivity will be high compared to the CO poisoned surface, making it harder for CO to stay on the surface. A high temperature almost always creates a surface with a low coverage, since the high temperature will increase both the desorption and reaction rates, two pathways for removing both CO and O.

	Low temperature	Intermediate temp.	High temp.
High CO conc.	CO poisoned	CO poisoned	Low coverage
Stoichiometric	CO poisoned	CO poisoned / Low coverage	Low coverage
Low CO conc.	CO poisoned / High O coverage	Low coverage	Low coverage

Figure 3.1: *A table describing the state of a platinum surface for different gas mixtures and temperatures. At certain conditions the state of the surface is bistable, causing hysteresis in some experiments.*

The table shown in Fig. 3.1 outlines what state the surface will be in under different reaction conditions. As can be seen, under certain reaction condition two states are viable. Which one of the two states will be seen depends on the history of the system. For example at around stoichiometric CO to O_2 ratio in the inlet gas, if we start at low temperature, the surface will be CO poisoned, then as the temperature is increased the rate will slowly increase, and at a certain temperature called the light off temperature, the CO adsorption can no longer keep up with the increased reaction rate. With more empty sites the O_2 adsorption increases and thus the reaction rate. This has the effect of 'burning' off all the CO from the surface in a dramatic switch to a surface with a low coverage and high reactivity [31]. Decreasing the temperature again will not put the surface back to the CO poisoned state, as the reactivity of the surface is now much higher keeping the coverage low. An example of this hysteresis is sketched in Fig 3.2.

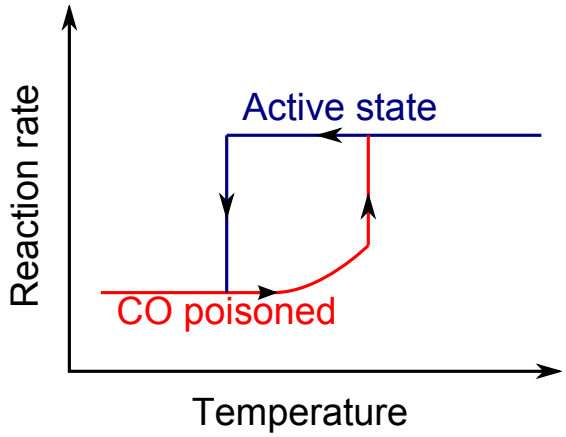

Figure 3.2: *A sketch of the bistable nature of the platinum surface at around stoichiometric CO to O_2 ratio in the inlet gas. Going from the CO poisoned platinum surface to the active state is referred to as light off. In the active state there is no temperature dependence of the reaction rate, as the CO is fully converted.*

The bistable condition of the platinum has been shown to cause spontaneous oscillations in the system under certain conditions. These oscillations has been the subject of a great deal of study. But to avoid complicating the measurements more than necessary, we have not looked into this effect, and focused on running the reaction under stable conditions.

3.2 Experimental results

Platinum thin film circles deposited on the inside of pyrex lids with RTD (see section 2.2.2) as shown in Fig. 3.3 were used as catalyst. The thin films sputtered from a pure platinum target in the cleanroom are patterned using photolithography in a liftoff process, which allows fine control over the deposited area. An important aspect as the main purpose of this study was to measure the sensitivity of the microreactor system, making well defined catalyst area essential.

The microreactor with a narrow capillary was used and the lid was hot bonded to the reactor. No special activation or cleaning steps were performed after mounting the microreactor, as the organic material from air exposure was quickly removed by the oxygen in the gas mixture.

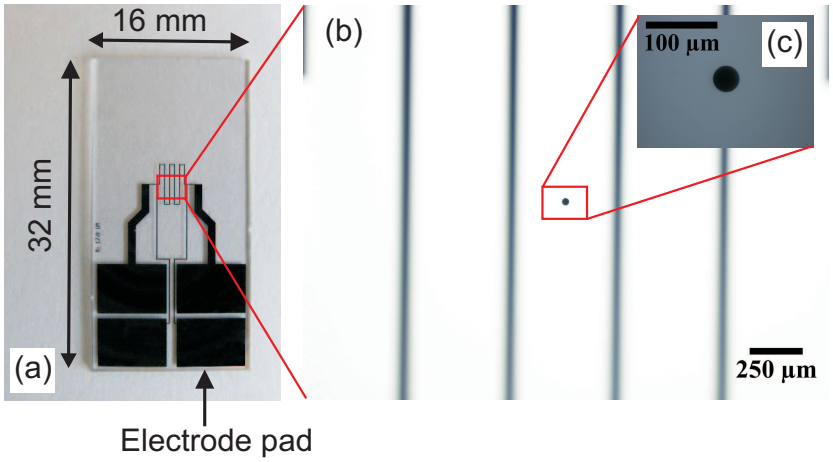

Figure 3.3: *Picture of a lid used for the CO oxidation on platinum measurements. (a) The lid with four electrode pads for electric contact in the four point measurement of the resistance of the meander structure. (b) Close-up of the meander structure with the catalyst visible through the pyrex. (c) Close-up of the platinum thin film circle catalyst with an area of 36 μm^2.*

3.2.1 Light off phenomenon

Exploring the parameter space of temperature and CO to O_2 ratio in preparation for the sensitivity study made it obvious that it would be beneficial to study the light of phenomenon to get a better understanding of the dynamics.

There were several advantages from using the microreactor setup for a study like this. The choice of platinum thin films as catalyst ensured that the state of the surface was well defined unlike for

dispersed nanoparticles on a porous support, where the temperature is unknown as the exothermic reaction might heat the catalyst locally. Furthermore, the state of the surface might vary from particle to particle, with CO poisoned surfaces at the flow entrance and low coverage surfaces at the exit.

The microreactor setup was also well suited for this study for practical reasons. The temperature can be changed rapidly as well as the gas composition, and no special care has to be taken when working with dangerous mixtures of CO and O_2 because of the tiny gas volumes.

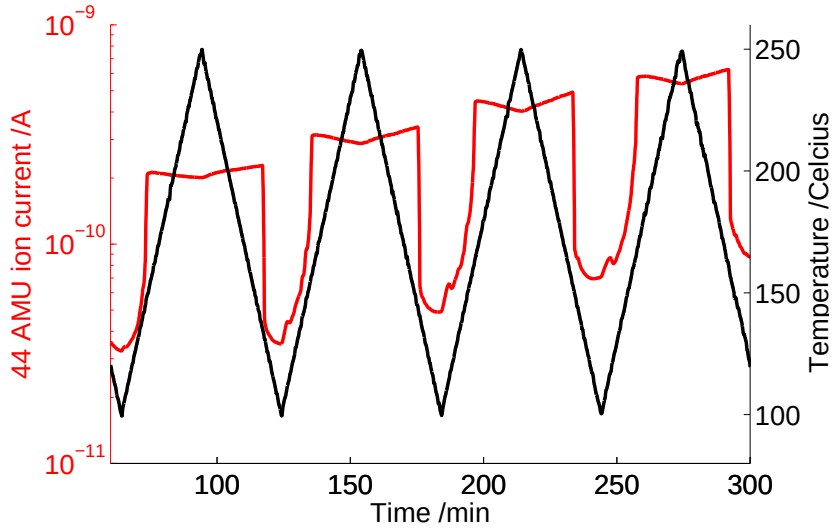

Figure 3.4: *Results from an experiment with CO oxidation on a 4 mm diameter platinum circle in a oxygen rich gas mixture. CO_2 production (44 AMU ion current) as a function of time for four consecutive temperature ramps from 100 to 250℃ and back with a rate of 5℃ per minute. Each set of temperature ramps correspond to a different pressure of 0.2, 0.4, 0.6, or 0.8 bar. The V shape seen in the ion current profile at high temperature is a result of the flow being temperature dependent (see section 2.6) while the CO is fully converted.*

An example of the result of studying the light off phenomenon for a small set of parameters is seen in Fig. 3.4, where the 44 AMU signal corresponding to CO_2 is shown as a function of time for four sets of temperature ramps, each set of ramps for a different pressure. To help interpretation of the results, the same data is shown as a function temperature in Fig. 3.5. Here the hysteresis is clearly seen for all four pressures. The temperature at which the switch in surface state happens varies with pressure, the lower the pressure the lower the light off temperature. The explanation is that at lower pressure

the CO partial pressure will be lower, making it easier to escape the CO poisoned state of the surface. By varying the gas mixture as well as the pressure, it was found that the effect of changing the O_2 partial pressure was minor compared to that of CO.

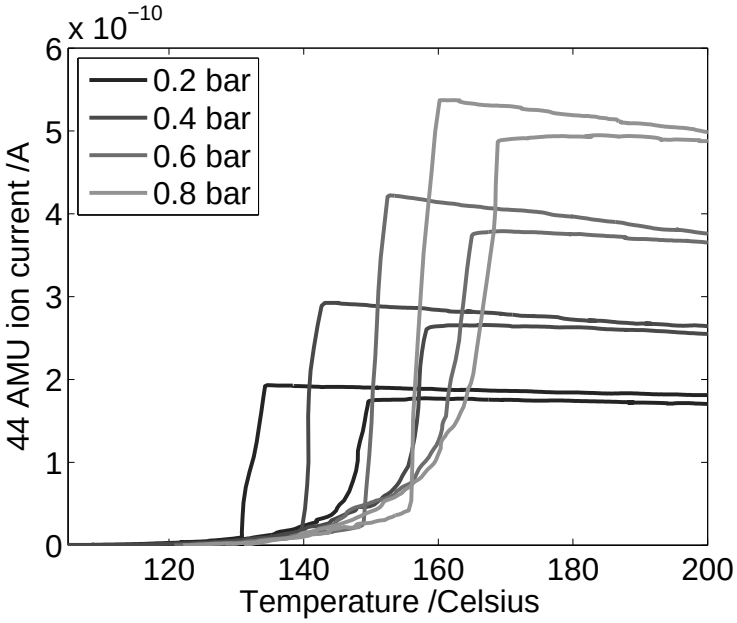

Figure 3.5: *CO_2 production (44 AMU ion current) as a function of temperature for the data shown in Fig. 3.4. At all four pressures a clear hysteresis is seen, with the light of temperature increasing with pressure, and the region of hysteresis diminishing.*

By turning off the flow of CO while keeping the O_2 flow constant, the CO partial pressure dropped as the desorption of CO from the stainless steel tubing and other dead volumes slowly wore off approaching the limit of a CO to O_2 ratio of 0. In this limit the light off was achieved at room temperature. Since at this point only trace amounts of CO were still in the gas flow, the CO_2 produced after light off (at full conversion) was very low, almost at the level of the background in the mass spectrometer. Therefore, the CO_2 produced in the light off process was clearly resolved. As the light off process is a matter of switching from a surface fully saturated with CO to an empty surface by reacting the CO off as CO_2, the amount of CO_2 produced should correspond to the number of adsorption sites, in this case the number of exposed surface sites.

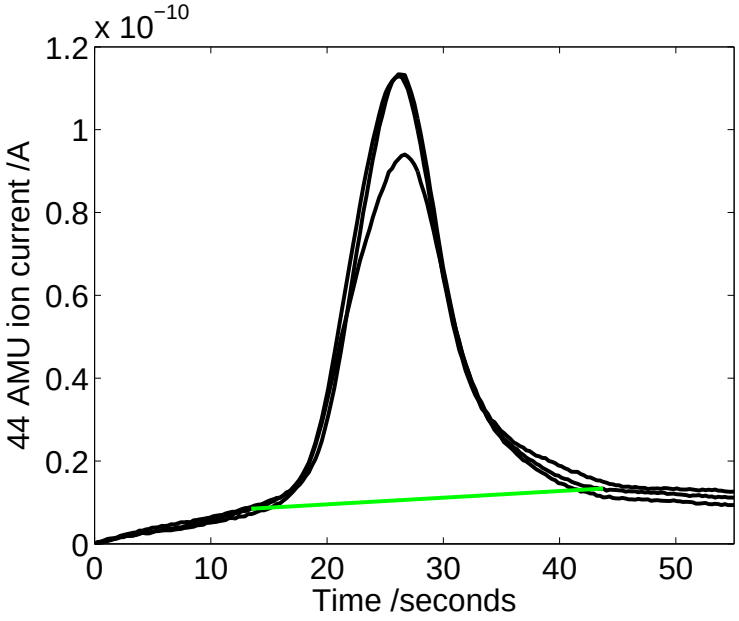

Figure 3.6: *CO_2 signal (44 AMU) during light off as a function of time from three consecutive measurements of light off at 30℃ on a 4 mm diameter platinum thin film circle ($1.9 \cdot 10^{14}$ sites). The peak area calculated with the green line as a background corresponds to 1.84, 1.93, and 2.00· 10^{14} molecules.*

Figure 3.6 shows the CO_2 produced during light off as a function of time. The experiment was performed as follows. The microreactor was kept at a constant temperature of 30℃ with a high flow of O_2 at 1 bar. A small amount of CO was let in until the surface was CO poisoned (seen as a rapid drop in reactivity) and then turned off again. By waiting, the CO content in the gas dropped and, at some point light off was achieved, and the next measurement was started by letting in CO again. The difference in the CO_2 signal before and after light off indicated the amount of CO in the gas at the time of light off. The width of the peak can be explained by the residence time of around 10 seconds in the reaction chamber. The area of the peak corresponds to 1.8 - $2.0 \cdot 10^{14}$ molecules, where the conversion has been done without prior calibration of the CO_2 signal. The reason why the first peak has a lower maximum than the following two might be a small change in the surface morphology caused by going from a CO poisoned to O saturated surface, opening up more CO adsorption sites. Compared to the number of atoms on a (111) surface of platinum on a 4 mm diameter circle of around $1.9 \cdot 10^{14}$, the numbers fit very well, especially considering the lack of calibration and the simple assumption of a perfect (111) surface.

The results show that the method could be used to estimate the platinum surface area of a more complex platinum catalyst of for example distributed nanoparticles.

Another method for determining the area could be through a temperature programmed desorption (TPD) measurement. A test with CO TPD was tried, but no good results came out of it. The two problems encountered was the higher sticking of CO to stainless steel combined with a higher background of CO in the mass spectrometer, resulting in smaller signals and a higher background. Furthermore, the fact that changing the temperature of the microreactor changes the background as discussed in section 2.6, makes measurements with constant temperature easier.

3.2.2 Sensitivity of the microreactor

By the sensitivity of the system, what is meant is the catalytic production needed for a given signal to rise significantly above the background and the noise level in the mass spectrometer. This means that the sensitivity will depend on both the reaction and the reaction conditions, and is as such not a simple measure. In this case, we wanted to see how little catalyst was needed to measure catalytic activity. Since CO oxidation on platinum is a fast reaction, it is well suited for this purpose. Furthermore, we chose to run the reaction at 1 bar and a reasonably high O_2 to CO ratio to have a high reaction rate. Running the reaction with the catalyst in the active state was not a good option, since we always ended up with full conversion, making any comparisons impossible.

In order to vary the amount of catalyst, we produced a series of pyrex lids with RTD's on one side and very small platinum thin film circles on the other side. In this way we could test the reaction rate for different well controlled amounts of catalyst area. The areas we tested was between 15 and 5000 μm^2. Since the areas tested varied by orders of magnitude, it was not possible to simply measure the rates of the different samples at a specific set of reaction parameters, as either the large areas would result in full conversion or the small areas would produce signals below the detection limit. What we instead did was measure the CO_2 signal during a temperature ramp as shown in Fig. 3.7. By plotting the data in an Arrhenius plot (see Fig. 3.8) it is clear that at low temperatures the signal is dominated by the noise and at high temperatures light off and full conversion takes place. But in between a standard Arrhenius behavior is seen, with an apparent activation energy, E_a, of $\sim$1 eV is found, agreeing with literature [32].

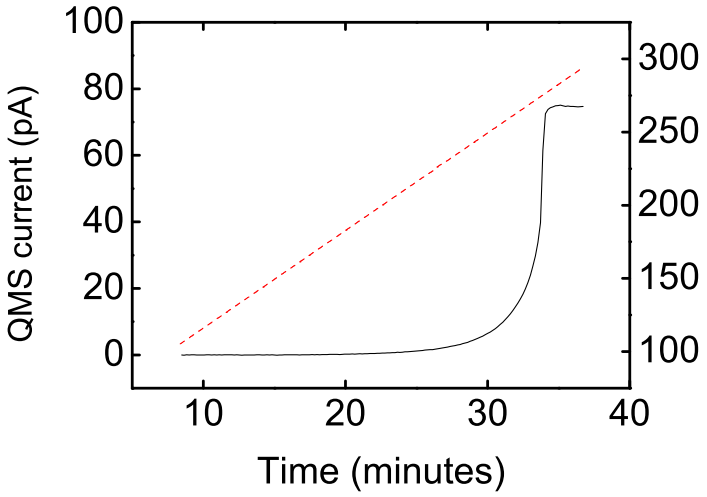

Figure 3.7: *The CO_2 signal (44 AMU ion current) measured while the temperature was increased with a constant rate of 400°C/h on a 515 μm^2 platinum thin film circle.*

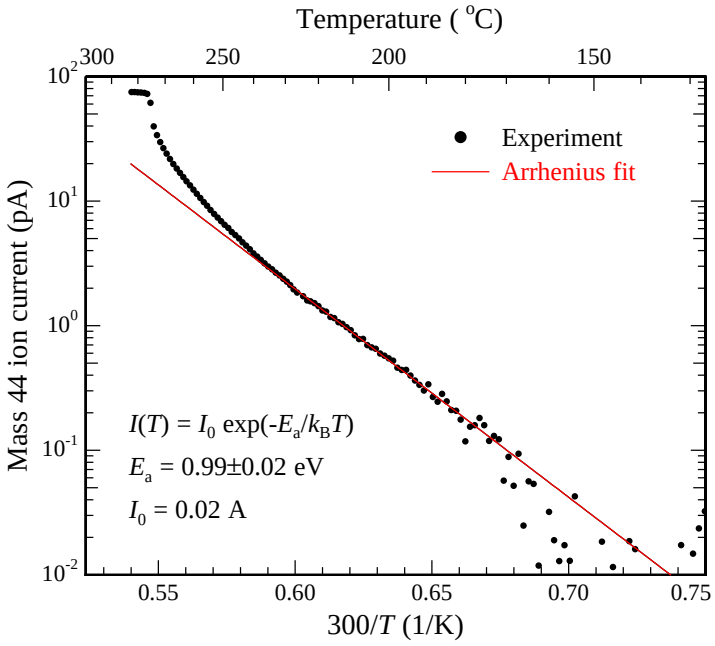

Figure 3.8: *Arrhenius plot of the data shown in Fig. 3.7 with the background subtracted. The Arrhenius fit has an apparent activation energy of 0.99 eV.*

To compare the different samples we looked at the temperature for which the CO_2 signal rose significantly above the noise level. An ion current of $1 \cdot 10^{-12}$A was chosen as an appropriate level. Since this ion current was reached at a temperature lower than the light off temperature on all the samples, we know the reaction rate, R, is equal to:

$$R = A \cdot k \cdot \exp(\frac{-E_a}{k_B T}), \tag{3.5}$$

where A is the area of the catalyst and k is the rate constant per area. Thus for a constant reaction rate of $1 \cdot 10^{-12}$A (R_{12}) the inverse of the temperature needed ($\frac{1}{T_{12}}$) as a function of area is:

$$\frac{1}{T_{12}} = \frac{k_B}{E_a} \left(\ln(A) + \ln(k) - \ln(R_{12})\right). \tag{3.6}$$

By plotting the measurements of these point for al the different platinum areas in a $\frac{1}{T}$ vs. $\ln(A)$ plot (see Fig. 3.9) the points fall on a straight line as expected with a slope corresponding to $E_a = 1.02$, which fits well with the individual E_a's measured.

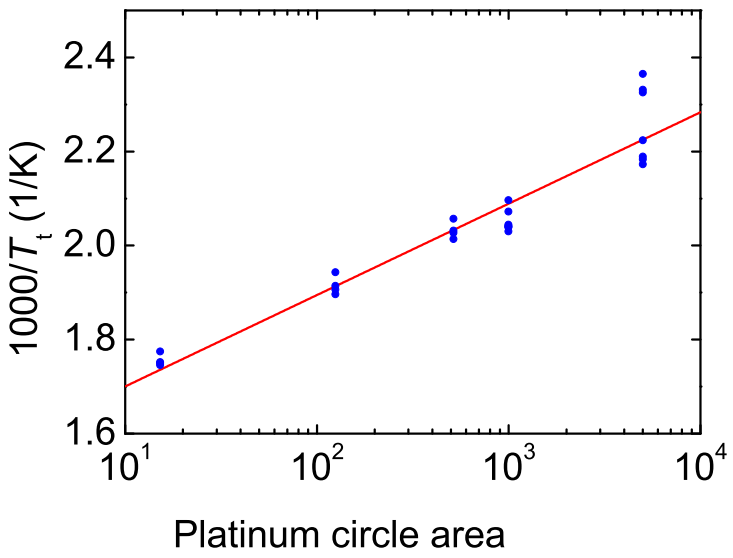

Figure 3.9: *The inverse of the lowest temperature where CO oxidation was measurable plotted as a function of the platinum circle area. The red line is a linear fit corresponding to an apparent activation energy of 1.02 eV.*

For the sample with the smallest catalyst area, 15 μm^2, the temperature needed was 300℃, which is close to the practical limit of the system, thus this area is close to the minimum area that can be measured on. Compared to other microreactors [33, 34], this is a very small catalyst area. If the area is converted into 10 nm nanoparticles, only $25{\cdot}10^3$ would be needed. Which is easily within the limit of for example the production using e-beam lithography or size selected clusters, making measurements on very well defined particles possible.

The experiments described in this chapter has shown the high sensitivity of the microreactor, being able to measure reactivity on as little as 15 μm^2 platinum, with and apparent activation energies of ∼1 eV for CO oxidation. It has also been shown that light off can be achieved at room temperature with a very low CO concentration, and this can be used for determining the surface area of platinum.

Chapter 4

Methanol synthesis on CuZnO

After working with CO oxidation, which has low industrial interest often used as a test reaction for its simplicity, we chose methanol synthesis. As catalyst, we chose Cu on ZnO in about even amounts with a small amount of Al_2O_3 to stabilize the catalyst, which is what is used industrially.

There were several good reasons for choosing this reaction for testing the microreactor. First of all, we wanted to test the system with a reaction that was not especially fast, more complicated than CO oxidation and not as well understood. In other words, was it possible for us to gain new mechanistic knowledge about a reaction using the microreactor system.

Secondly, we were interested in trying to take advantage of the fast response time of the microreactor system to explore transient behavior in a reaction. The methanol synthesis was interesting in this regard because several studies [35, 36] has looked into changes in the CuZnO catalyst with changes in the gas environment. Finally, we wanted to get away from using simple thin films as catalyst, and work towards actual nanoparticles as catalyst, which an industrial catalyst would allow us to.

4.1 Methanol synthesis

The chemical methanol, CH_3OH, is an important intermediate in the chemical industry used in the production of many higher chemicals. Methanol can also be used for storing energy as a liquid fuel because of its high energy to volume(weight) ratio and ease of use [37].

Industrially, methanol is synthesized at 200-250℃ and 50-100 bar

from a gas mixture of 90% H_2, 5% CO, and 5% CO_2 [1]. The high pressure and temperature is what makes the synthesis expensive. The high temperature is needed to get a reasonable rate. The higher pressure also increases the reaction rate, but is needed to change the equilibrium concentration which is negatively influenced by the high temperature as the reaction is exothermic.

There are two processes taking place during synthesis:

$$3H_2 + CO_2 \rightarrow CH_3OH + H_2O \tag{4.1}$$

$$CO + H_2O \rightarrow CO_2 + H_2 \tag{4.2}$$

As can be seen, no CO actually takes part in the production of methanol, but introducing CO into the gas mixture helps the reaction in several ways by reducing the water concentration in the gas, which changes the equilibrium concentration of methanol and increases the reaction rate [38, 39].

The direct formation of methanol from CO:

$$2H_2 + CO \rightarrow CH_3OH, \tag{4.3}$$

which would be a better reaction as the equilibrium concentration is more favorable, does not take place [40]. Or if it does take place, the rate is so low that it is insignificant.

The reaction pathway for methanol synthesis is not fully understood, but formate is believed to be an intermediate in the reaction [41]. Formate is also the main species on the surface during reaction.

4.2 Transient increased reaction rate

Studies have shown that a large increase in reaction rate is seen after pretreating the CuZnO catalyst in a gas mixture of CO and H_2. The increase in the rate is temporary, but the pretreatment can be performed over and over again to regain the transient increase in reaction rate [42].

An extensive ETEM study has shown that by changing the gas environment of Cu clusters deposited on ZnO, the morphology of the Cu particles is changed [36]. The more CO_2 and especially water present, the more the Cu clusters ball up, and the more H_2 and CO there is, the more the Cu clusters wet the ZnO and flatten out. One suggested explanation for this behavior is that the ZnO is reduced by CO and H_2, creating stronger interaction between the ZnO and the Cu giving rise to the wetting effect. The surprising thing is that a maximum in this effect is not seen with pure CO (which has a

higher reduction potential than H_2), but with an even amount of CO and H_2, and at the same time the highest transient methanol production rate is seen at this 1:1 CO:H_2 mixture.

At this stage there are several interesting open questions with regards to this mechanic. First of all, why is the rate increased and is it something that can be used to increase the rate industrially? If for example the rate is increased because the surface area is increased when the Cu wets the ZnO, or a specific site is more likely to be exposed, then it might be something that could be taken into account when synthesizing the catalyst increasing its performance. A key question is, what can explain why both CO and H_2 is needed for the transient increase in reaction rate? With better understanding a greater effect could possibly be achieved, or a static increase in reaction rate could be forced, which would of course be of great interest.

4.3 Experimental results

The experimental results are divided into two parts. An investigation of the transient increase of reaction rate, trying to reproduce the results by Vesborg et al. [36], and work done on formate TPD measurements, trying to correlate the results with the transient reaction rate study.

To reduce the size of the catalyst to a size suitable for the microreactor, as an industrial catalyst comes in cm sized pellets, and the microreactor depth is only 3 μm, the first step was to find a way to get the catalyst into the reaction chamber.

4.3.1 Catalyst deposition

The first step was grinding down the catalyst pellets into smaller particles to be suspended in demineralized water. To remove the largest particles the suspension was sonicated and a couple of minutes was given for the largest particles to precipitate, whereafter, the rest of the suspension was sampled, dried, and weighed. Finally the catalyst was suspended in demineralized water at a concentration of 1 g/L and sonicated again.

The catalyst was deposited by dropping 1-10 μL of the catalyst suspension onto the microreactor while it was on a hotplate at around 50℃ for faster water evaporation. This method gave a somewhat uneven distribution of catalyst particles in the reaction chamber because of the way the water droplet evaporates. The total

amount of catalyst should in theory be controllable, but because of the instability of the suspension, rather big variations in deposited amount were seen. Since the amount of deposited catalyst was so small, it was not possible to measure it after deposition by for example weighing. For the experiments studying the transient behavior it was not necessary to know the exact amount of catalyst, but this means that it does not make sense to talk about the rate per site or compare the rates from sample to sample. Which is why discussion about reactivity in the next sections will only be about qualitative observations.

4.3.2 Investigation of transient reactivity

The initial experiments were used to test different catalyst amounts, in order to get a high enough conversion to see significant methanol signals during reaction, but low enough conversion that we did not run into problems with equilibrium concentration. The first real experiment was to try and reproduce the result showing higher transient methanol production with a pretreatment of a 1:1 CO:H_2 gas mixture.

The experiment was setup in the following way. The overall pressure was set to 1 bar and the temperature was set to a constant 160 ℃. One gas line was filled with a methanol synthesis gas: 75% H_2, 10% CO, 10% CO_2, and 5% He as a calibration gas. The other gas line was filled from two flow controllers, one supplying H_2 and one supplying CO, making a range of mixtures of the two possible. Because of the way the gas handling system works, switching between the synthesis gas and the pretreatment gas only took in the order of seconds as the mixing takes place on the chip. After switching gas, only trace amounts of the closed gas feed diffused into the reaction chamber. On the other hand, changing the ratio of H_2 to CO in the pretreatment gas took several minutes, since all the gas in the gas line has to be replaced. This means that the CO and H_2 gas mixture did not have the exact ratio requested and especially in the case of pure CO and pure H_2, the gas was not 100% pure, most pronounced for pure H_2 since it took a long time to remove CO from the gas lines, as CO is adsorbed on the stainless steel tubing walls.

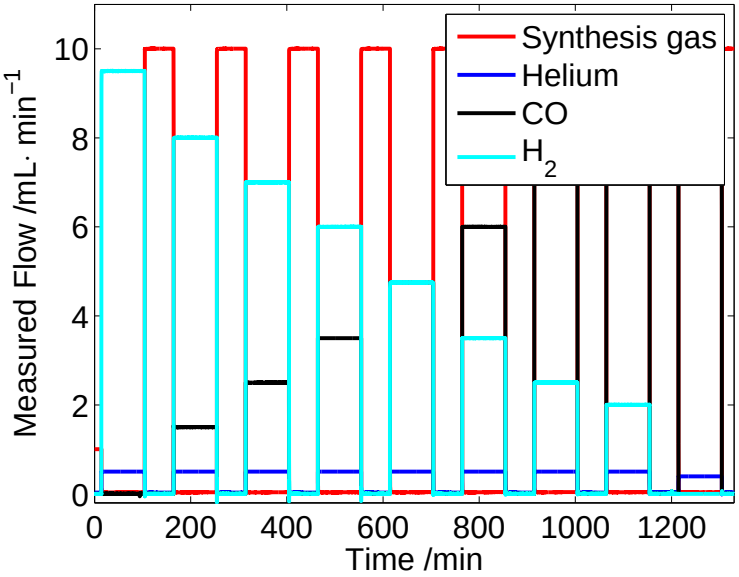

Figure 4.1: *Flow measured by the four MFC's during a measurement of the transient methanol production as a function of CO to H_2 ratio in the pretreatment gas mixture. Experiment performed automatically in a single 24 hour session.*

Figure 4.1 shows the parameters scanned as a function of time in an experiment measuring the transients after nine different pretreatment mixtures. Figure 4.2 shows the QMS signal for 31 AMU recorded simultaneously, here it can be seen that clear transients in the methanol production appear with varying maxima for the different pretreatments, and furthermore, the high time resolution of the microreactor system clearly resolves the full transient peak, as the time constants in the transient are reasonable long in the order of minutes.

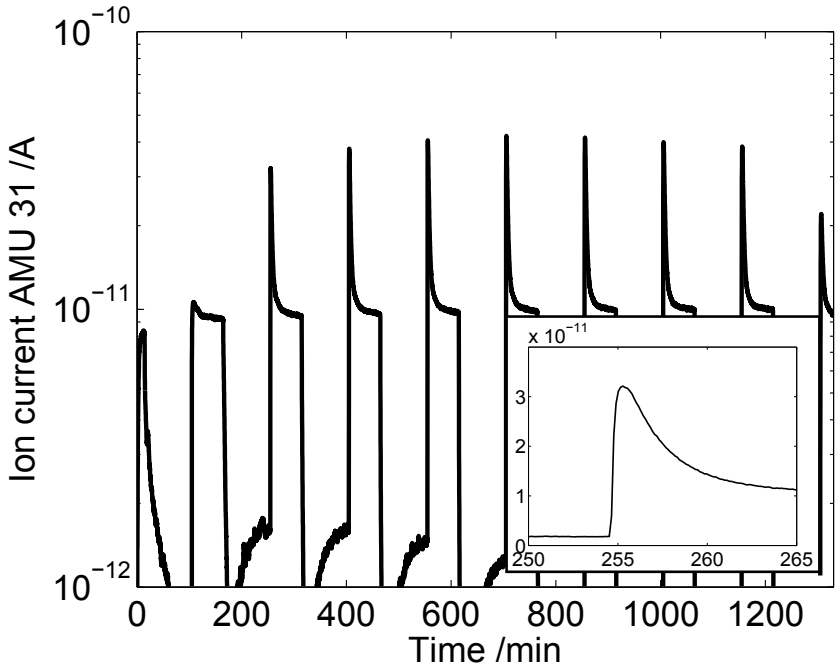

Figure 4.2: *The methanol signal (31 AMU ion current) measured as a function of time. The gas is switched between methanol synthesis gas and a pretreatment gas mixture of varying amounts of CO and H_2. After each pretreatment a transient increase in methanol production is seen as a narrow peak. Insert: close-up of a single peak, showing that it is fully resolved with time constants in the order of minutes.*

One thing to notice is the nonzero methanol signal during pretreatment even though CO and H_2 alone should not be enough to produce methanol. There are two likely explanations for such a signal that does not involve direct formation of methanol from CO, as the signals are very small. Either the continuous diffusion of CO_2 from the closed line, or a reduction of the ZnO support are sources of oxygen opening up for methanol production. Throughout the pretreatment process the methanol production increases, indicating the transformation of the catalyst to a more active state.

The relative increase in methanol production at the peak of each transient is plotted as a function of the percentage of CO in the pretreatment gas and shown in figure 4.3. The data reproduces the previous result well. Again a clear maximum in the transient production is seen at about even CO to H_2 ratio. Since we at this early stage in testing were mainly interested in the quantitative behavior, the setup was not calibrated for this experiment, and thus the exact shape of the curve might change a bit, but not the general trend.

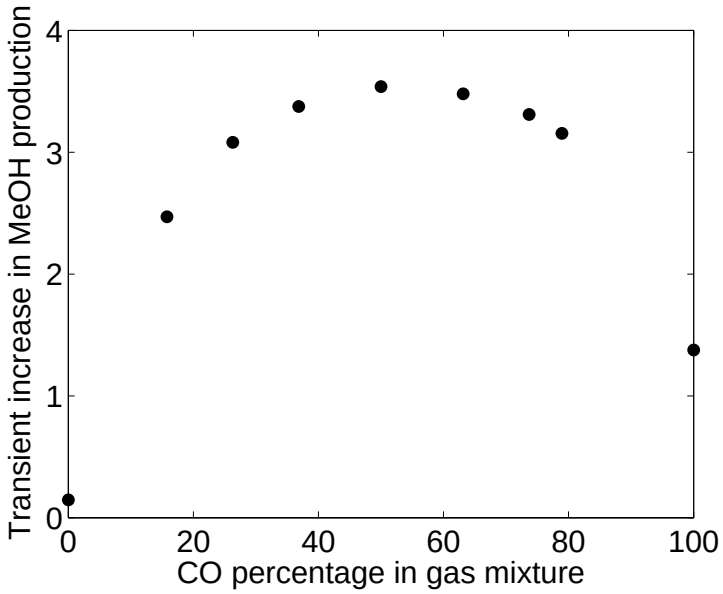

Figure 4.3: *The peak height of the transient methanol production as a function of CO to H_2 ratio in the pretreatment. A clear maximum is seen when the ratio is close to 1:1.*

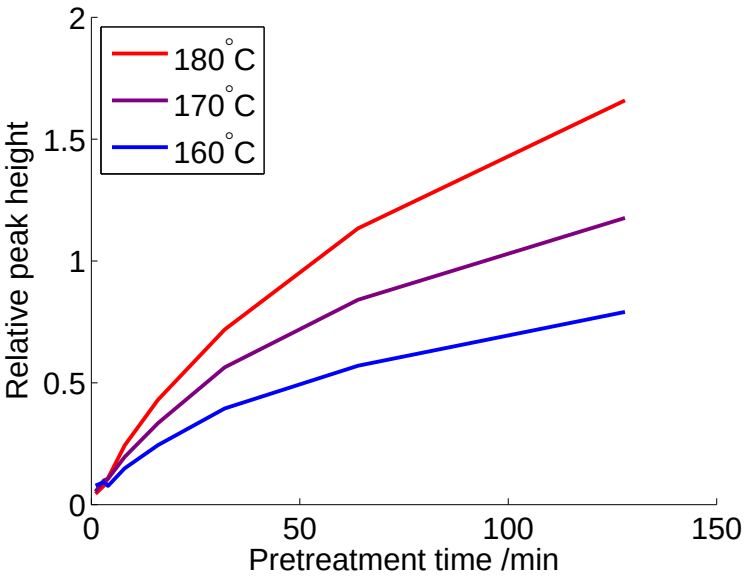

Figure 4.4: *The result of an experiment where the pretreatment time with a one to one CO to H_2 gas mixture was varied for three different temperatures. For each measurement the relative peak height compared to the steady state methanol production at that temperature is plotted as a function of the pretreatment time.*

One aspect of the dynamics of the pretreatment, the time constant involved, is examined in an experiment where the pretreatment time is varied for three different temperatures, whereafter the transient methanol production is measured. The maximum of the transient peak is plotted as a function of pretreatment time in Fig. 4.4. After two hours the transient is still increasing. The higher the temperature the faster the process is.

To examine the surprising maxima in transient methanol production at a one to one ratio of CO to H_2 in the pretreatment gas, a series of experiments were performed where the pretreatment was split into two, one with pure CO and one with pure H_2 to see if there is a real symbiotic effect of the two gases, or if each gas has their separate role that can take place one after the other. The result of an experiment where the temperature was lowered[1] as the gas was changed between H_2 and CO is seen in Fig. 4.5. Transients are seen for both orderings of the pretreatment processes, with the highest seen for the pretreatment with CO first followed by the H_2. It has to be noted that e.g., some H_2 from the synthesis gas could potentially be left in the system during the pretreatment, skewing the results. A more thorough study is needed before a final conclusion can be made on this issue.

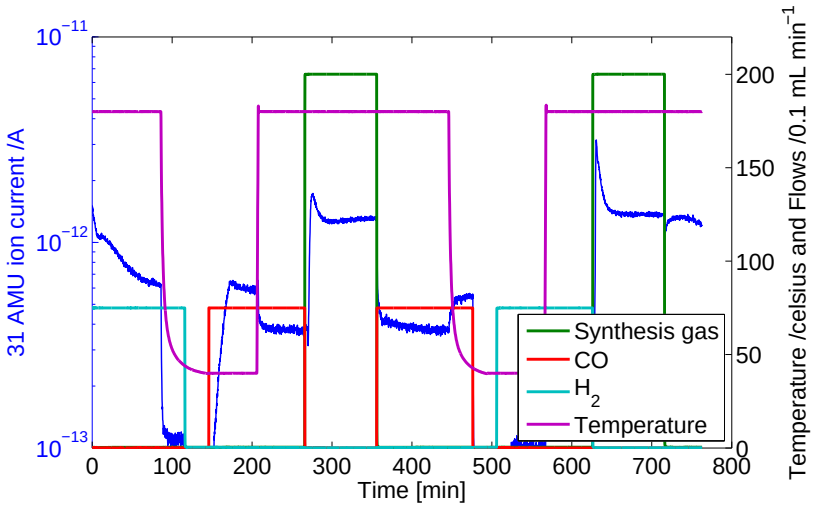

Figure 4.5: *Testing the supposed beneficial effect of having both CO and H_2 present at the same time during pretreatment by letting in the two gases sequentially. The methanol synthesis and pretreatment was performed at a temperature of 180℃, but the temperature was lowered to 50℃ as one pretreatment gas was pumped out before letting the next one in to help with the stability of the pretreated catalyst.*

[1] The stability of the active state of the catalyst was tested by heating to 240℃ for 5 minutes under vacuum, which resulted in the loss of any transient methanol production.

The stability of the highly active state of the catalyst was tested in an experiment, where the reactor was cooled down to 60℃ after pretreatment at 160℃. At 60℃ the gas was changed to methanol synthesis gas for varying lengths of time, before the reactor was heated back up to 160℃ and the transient methanol production was measured. This experiment showed a slow decay of the transient methanol production with a time constant in the order of 1 hour. Surprisingly though, the methanol production in synthesis gas while at 60℃ was nonzero as can be seen in Fig. 4.6. Just as the highly active state was transient at high temperature the activity at 60℃ was also transient, just with a longer decay time, but as the methanol production is was also a lot lower at 60℃. The total area of the transient peak was not as large as for the high temperature.

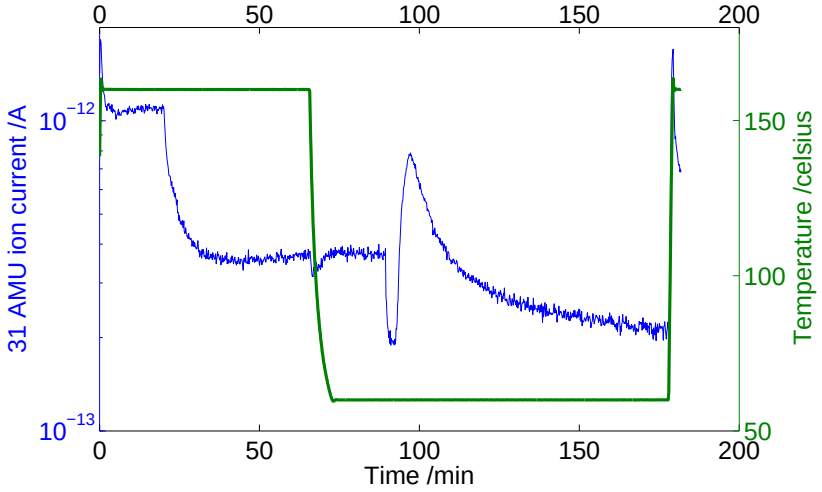

Figure 4.6: *A plot of methanol production at 60℃. After a pretreatment at 160℃ in a one to one gas mixture of CO and H_2 the temperature was lowered to 60℃ whereafter the gas was switched to methanol synthesis gas. A transient methanol production was seen lasting many minutes. The reason the 31 AMU signal is higher before the switch to methanol synthesis gas than after the transient production is complete, is that the high level of CO in the pretreatment gas has a significant background at 31 AMU in this range. The number of methanol molecules measured in the peak was around* $9.4 \cdot 10^{14}$.

Since we did not know the amount of catalyst in the reactor because of the deposition method, it is not straightforward to prove or disprove that the highly active state of the catalyst is some active surface species covering the surface after a pretreatment procedure. Or if it is a higher surface area caused by morphology changes of the particles or something else with a potential for long term

stable reaction rate increase. To get a better idea of the amount of catalyst in the reactor, some time was spent on trying to produce a TPD measurement that could be correlated with the surface area of the catalyst. Some success was achieved when using the formate present at the surface during synthesis as the detection molecule. The following section will describe the experiments and some of the results obtained from these experiments.

4.3.3 Formate TPD

The procedure for making the TPD measurement was the following. First, the catalyst was heated up to what I will refer to as the synthesis temperature in synthesis gas, to get the reaction running and thus formate formed on the surface. After a certain amount of time, the temperature was set to 90℃ and a few minutes were given for the reactor to cool down. At 90℃ the gas was changed to helium and the pressure lowered to 0.1 bar and again a few minutes delay was introduced before the temperature was lowered to 50℃ until the gas system equilibrated to the changes. Finally, the reactor was heated to 240℃ with a rate of roughly 1℃/s. The reason for stopping at 240℃ was to avoid sintering of the catalyst. During the heating ramp, formate on the surface decomposed to CO_2 and H_2 which was released to the gas phase. The mass spectrometer was set to detect CO, H_2O, CO_2, and methanol in case other molecules were on the surface. It was not possible to detect H_2 as the background was too high.

Figure 4.7 shows an example of the CO_2 signal as a function of temperature measured in a set of TPDs for three different synthesis temperatures. As can be seen, the area of the CO_2 peak, corresponding to the formate on the surface becomes higher with lower synthesis temperature. This agrees well with the fact that the formate coverage on the copper surface is highest at low temperature [38].

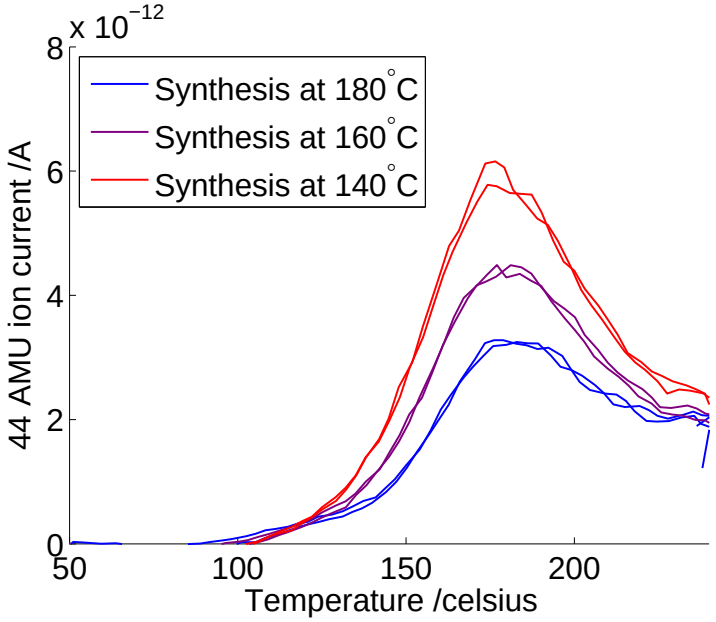

Figure 4.7: *The result of 6 TPD measurements of adsorbed formate after methanol synthesis at either 140, 160, and 180℃. The formate decomposes at the surface when heated with a rate of ∼1℃/s, and is detected as CO_2 (44 AMU ion current) as it desorbs.*

To get as accurate a measure of the catalyst area as possible, a TPD at 90℃ was performed as the formate coverage was highest at this temperature. To ensure enough time was given for the formate to build up on the catalyst in the methanol synthesis gas, a study of the effect of different synthesis times at 90℃ was performed. The result of the study can be seen in Fig. 4.8. For a better overview, the areas of the peaks are plotted as a function of the synthesis time at 90℃ in Fig. 4.9, which shows a fast increase in area at the beginning, with a slow approach to a maximum peak area after about 3 hours in methanol synthesis gas at 90℃. The area of the peak corresponds to approximately $3.2 \cdot 10^{14}$ CO_2 molecules, and if a formate coverage of 30% is assumed and each CO_2 molecule correspond to one formate molecule, the exposed copper surface has roughly $1 \cdot 10^{15}$ surface atoms. Compared with the number of methanol molecules produced in the transient at 60℃, of a similar number, which is a lot lower than the amount of methanol produced in the transient peaks at high temperature, it should be clear that the highly active state of the catalyst can not just be an adsorbed surface species easily converted to methanol.

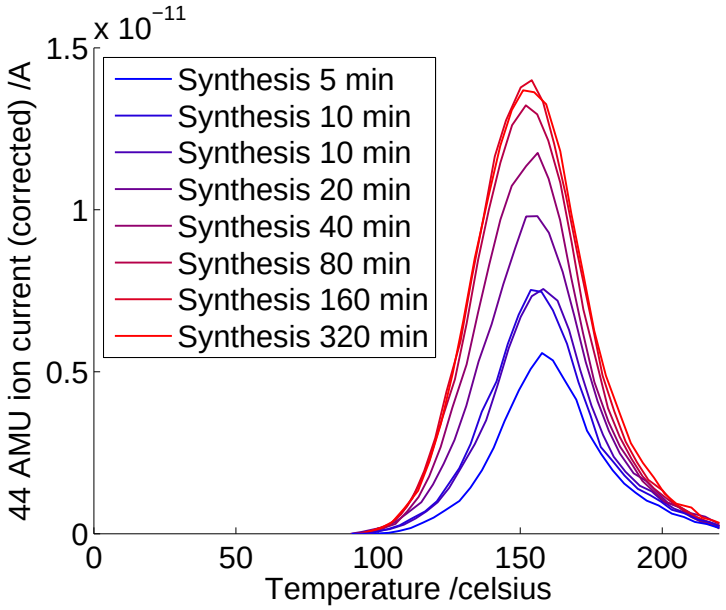

Figure 4.8: *The result of a series of formate TPD measurements performed after exposing the catalyst to methanol synthesis gas for various time intervals. The formate is measured as CO_2 (44 AMU ion current) which formate decomposes into during the heating with a rate of ~ 1℃$/s$.*

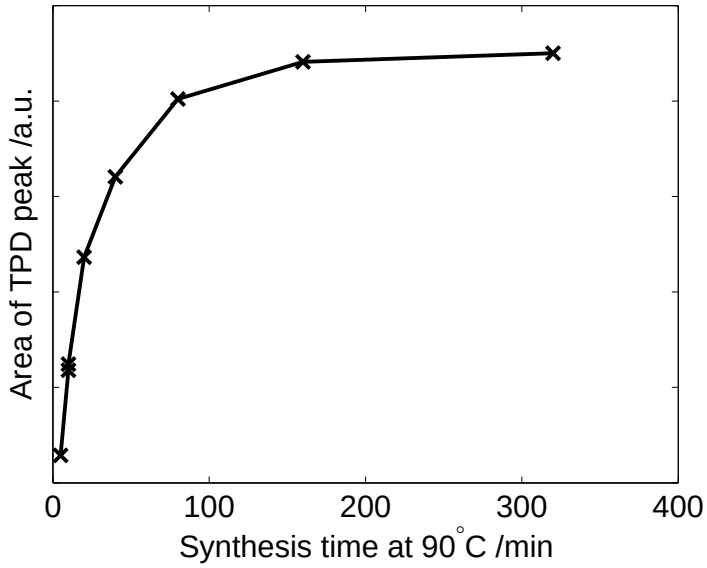

Figure 4.9: *The area of the formate TPD peaks shown in Fig. 4.8 plotted as a function of the time the catalyst was exposed to synthesis gas at 90℃. The maximum level reached after about 3 hours corresponds to approximately $3.2 \cdot 10^{14}$ formate molecules.*

In this chapter it was shown that a transient increased methanol production is seen for CuZnO catalysts after pretreatment in CO and H_2, with the greatest effect at a one to one ratio of CO to H_2. A surprising methanol production at 60℃ of the active state of the catalyst after pretreatment was discovered. The kinetics behind the active state was studied and formate TPD measurements were tested as a method for determining the catalyst area. This study was not finished during my PhD.

Chapter 5

Mass selected Ru nanoparticles

The main goal when designing the highly sensitive microreactor was to create a platform making measurements of the catalytic activity of well defined nanoparticles possible, with the purpose of creating a better understanding of the relation between activity and morphology. The first candidate for well defined nanoparticle production for the microreactor was the nanoparticle source here at CINF, which can produce mass selected nanoparticles with sizes ranging from around 2 to 15 nm. The reason why the microreactor system is a good platform for making these measurements, is that the production of the nanoparticle source is so low that it is almost practically impossible to produce enough catalyst for measurements in a more conventional reactor.

Motivation for measuring the reactivity of mass selected nanoparticles comes from the fact that by comparing the reactivity of nanoparticles of different sizes, insight into the nature of the active sides on the nanoparticles can be gained. As the size of the nanoparticles change, the ratio of corner, edge, and facet sites will change. Thus, if a trend in reactivity relates to the changes in morphology, it can lead to knowledge about the active site, and potentially improved reactivity or selectivity when synthesizing new catalyst.

5.1 CO methanation on ruthenium

A key point in finding a catalyst and a reaction appropriate for a study of reactivity vs. particle size, is that there is en effect of varying the size. A reaction that takes place on the facets of the nanoparticles, and only interacts with a single surface atom would

for example see no size effect in the range of sizes our nanoparticle source produces, since the amount of facet sites per total surface area would be almost constant. The reaction decided upon for this study was CO methanation on ruthenium nanoparticles [43, 44]:

$$CO + 3H_2 \rightarrow CH_4 + H_2O \tag{5.1}$$

A reaction which is e.g., used for removing CO from the feed gas in ammonia plants [45], as CO poisons the catalyst.

The reaction mechanism for this reaction on ruthenium is believed to be dissociation of CO followed by hydrogenation of O to H_2O and of C to CH_4 with the rate limiting step being the initial breaking of the CO bond [46]. This step is believed to take place only at the step sites [47]. Thus, in theory the optimal nanoparticle size would be rather small, since this increases the ratio of edges and thus step sites to the total surface area.

5.2 The nanoparticle source

Production of the mass selected nanoparticles happens in a magnetron-sputter gas-aggregation source, which forms the nanoparticles, combined with a quadrupole mass filter, which filters the formed particles according to mass to get a narrow distribution of particles. As long as the particles with the same mass do not have large differences in morphology, there will be a one to one correspondence between mass and size, making the terms size selected and mass selected interchangeable.

The ruthenium nanoparticles are created from a 99.99% pure ruthenium target which is sputtered to create a flux of ruthenium atoms. The sputtering is carried out with a helium argon mixture inside an enclosure cooled by liquid nitrogen. By condensation with the aid of the cold gas atoms, the ruthenium atoms aggregate into larger nanoparticles before they exit the enclosure by a 3 mm opening. The size of the particles will be determined by a combination of the sputtering power, the length of the aggregation zone, and most importantly the flow of helium and argon. By having a large flow of gas, the atoms will have a shorter time to aggregate, and the result will therefore be smaller particles. At the exit from the aggregation zone 30-80% of the particles will be single charged and can thus be filtered by mass using the quadrupole mass filter to get a narrow distribution of sizes.

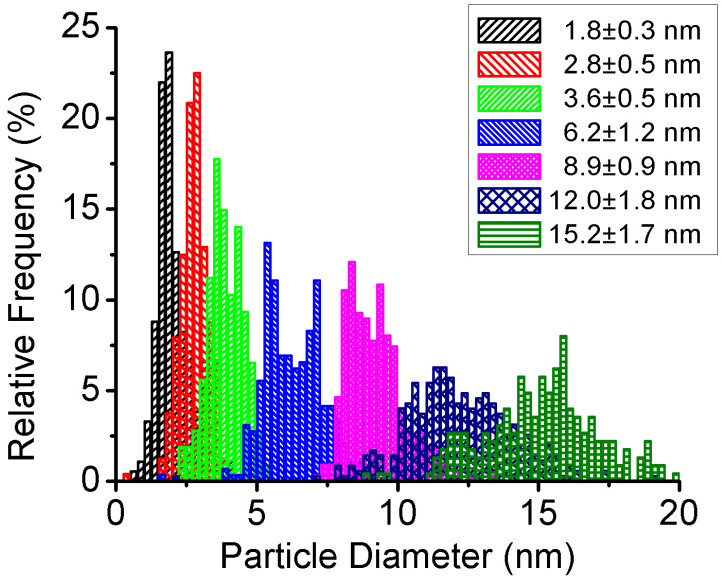

Figure 5.1: *Histogram of the nanoparticle distributions as a function of particle diameter for a series of mass selected particles with sizes between 1.8 and 15.2 nm in diameter. The diameter and frequency was measured by TEM studies of the particles produced at the different settings. The smaller the particles, the more narrow the distribution.*

Figure 5.1 illustrates some possible size distributions that can be produced with the setup configured to sizes from 1.8 to 15.2 nm.

In order to get the nanoparticles into the microreactor a sample holder was modified to carry the microreactor inside the UHV chamber containing the nanoparticle source. The amount of particles deposited was counted by measuring the current from the charged particles hitting the microreactor. As the particles are single charged, the current should correspondd one to one to the number of particles. To verify the output of the source, scanning electron microscopy (SEM) was used.

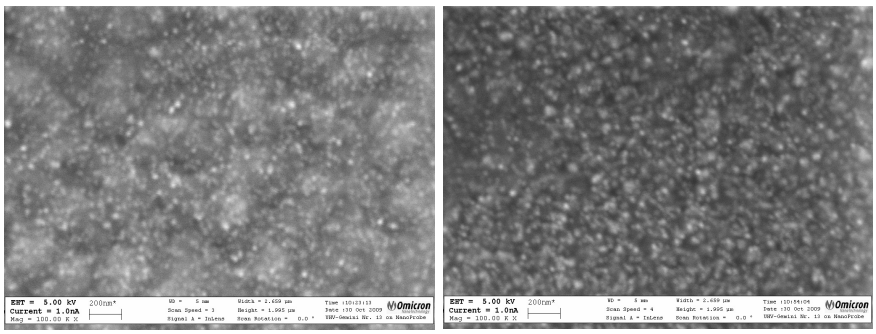

Figure 5.2: *SEM micrograph of 7 nm ruthenium nanoparticles at the bottom of the reaction chamber (left) and at the top of the support pillars (right). The long scale roughness seen in the image from the reactor bottom is an artifact of the RIE process used for etching the reaction chamber.*

The surface roughness caused by the etch for the reaction chamber, made resolving the particles difficult as seen in Fig. 5.2, which is why the focus was switched to the unetched and therefore completely flat top of the pillers in the reaction chamber. But, even here it was difficult to resolve the particles well. Together with the fact that the density of particles varied across the microreactor, it made the SEM micrographs inaccurate for determining the total number of particles, and therefore verify the particle current measured during deposition. The reason for the lack of resolution, was probably a combination of organic contaminants on the microreactor surface from of air exposure, and vibrations from the turbopump used in the nanoparticle source. At a later stage the problem with the vibrations was solved by enabling easy disconnecting of the nanoparticle source from the analysis chamber, where the SEM micrographs are recorded.

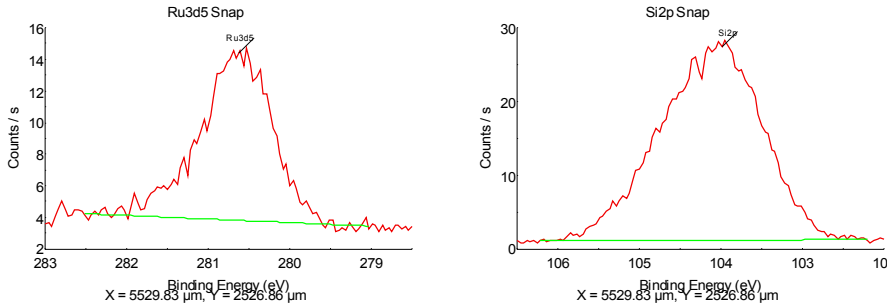

Figure 5.3: *Two examples of the XPS spectra recorded for the spatial image shown in Fig 5.4. The two bonding energies focused on corresponding to the Ru $3d_{5/2}$ peak (left) and the Si 2p peak (right)*

After deposition a microreactor was transferred to another UHV chamber for spatial X-ray photon spectroscopy (XPS) analysis. For a grid with a spacing of 0.2 mm times 0.2 mm, XPS spectra for the ruthenium $3d_{5/2}$ peak and the silicon[1] 2p peak (see Fig. 5.3) was recorded across the whole microreactor. The intensity of the ruthenium peak is shown as a function of position in Fig. 5.4. This clearly shows that there were problems with the beam of nanoparticles, being neither circular nor being positioned correctly. This was not expected, and made the particle number calculated from the current measured during deposition incorrect. A lot of the particles counted did not end up in the reaction chamber on the microreactor. This problem was fixed at a later stage by inserting a mask between the microreactor and the nanoparticle source, with the option of measuring the current of particles on either the microreactor or the mask. Helping with alignment and only counting particles deposited inside the microreactor.

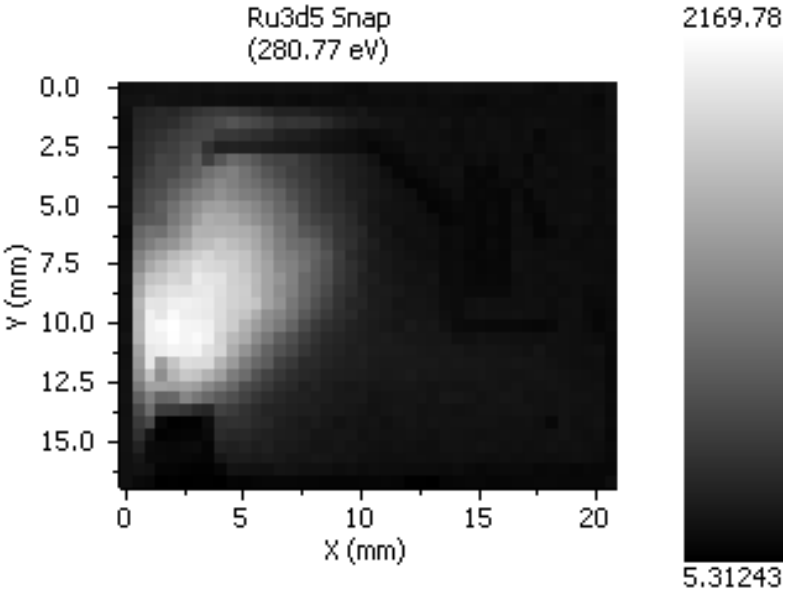

Figure 5.4: *Spatial XPS map of the total count in the Ru $3d_{5/2}$ peak shown in Fig. 5.3 on a microreactor with $3{\cdot}10^{10}$ 6 nm ruthenium nanoparticles deposited. The grid spacing of the XPS spectra was 0.2 mm in both directions.*

[1] As the top layer of the silicon microreactor was oxidized, the peak for SiO was used

5.3 Experimental results

5.3.1 Parameter study

In preparation for the study of size selected nanoparticles reactivity as a function of size, a single microreactor in which $3 \cdot 10^{10}$ 6 nm ruthenium nanoparticles were deposited was used for a parameter study.

As the catalyst loading was low, a microreactor with a narrow capillary was used, and as the stability of the nanoparticles was not a problem, the reactor was hot bonded. The first step after mounting the microreactor was to reduce the ruthenium[2] in pure hydrogen until all signals in the mass spectrometer were stable.

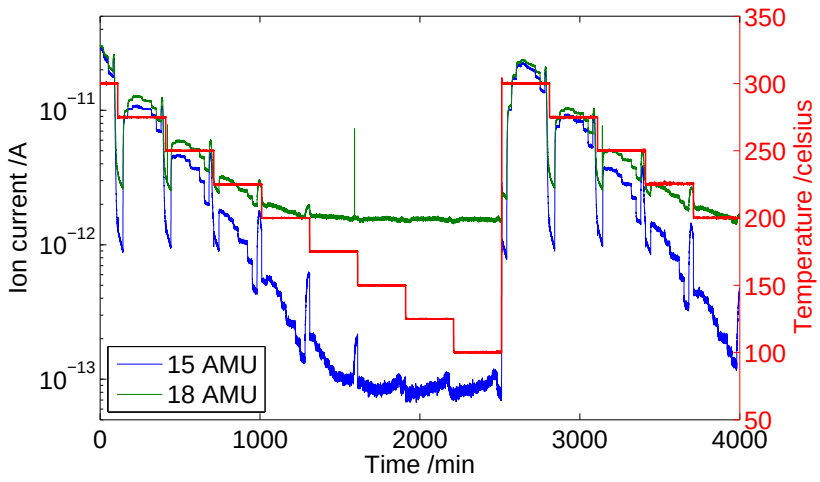

Figure 5.5: *The result of a parameter study for CO methanation on $3{\cdot}10^{10}$ 6 nm ruthenium nanoparticles. The temperature was stepped from 100 to 300℃ in steps of 25℃. At each temperature step the CO to H_2 ratio was varied from pure H_2 to almost 20% CO in H_2 in 8 steps. The order of magnitude higher background for the water signal (18 AMU) than for the methane signal (15 AMU) makes comparison of the two impossible at temperatures below 250℃ where the rate is considerably higher than the background, but at higher temperature the expected one to one ratio is seen.*

For the parameter study a large set of temperatures and CO to H_2 ratios were scanned while the ion currents corresponding to the molecules of interest were monitored. The results are shown in Fig. 5.5 where the AMU 15 and AMU 18 signals, corresponding to the methane and water produced, are plotted as a function of time

[2]The ruthenium particles produced in the nanoparticle source were initially metallic ruthenium, but during transfer and bonding of the microreactor, the particles were oxidized.

together with the temperature. Even at low temperature (175℃) a clear methane production can be seen, and at higher temperatures where the production of water is significantly higher than the background, a one to one ratio of water to methane is seen as expected. By taking the methane production at each set of parameters and plotting it in an Arrhenius plot (see Fig. 5.6) a much better overview is gained, and kinetic properties about the reaction can be extracted.

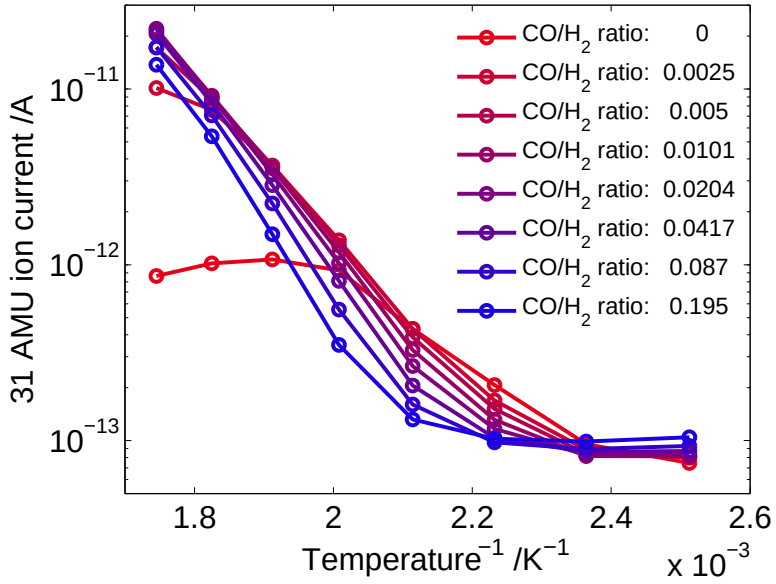

Figure 5.6: *An Arrhenius plot of the methane production from the parameter study data shown in Fig. 5.5. Each colored line correspond to a different CO to H_2 ratio. The reason a methane signal is seen for the line corresponding to pure H_2 is that the time at this gas composition was not long enough to remove the CO completely from the gas lines. This took a while as there were small dead volumes contributing with diffusion and desorption from the steel tubing which were not insignificant.*

Above the temperature, where the methane production is higher than the background, an Arrhenius behavior was seen for all the different CO and H_2 compositions with an apparent activation energy of 0.8 to 1.2 eV. The higher activation energy was measured for the gas compositions with a high amount of CO. This fits with the catalyst being CO poisoned as indicated by the fact that at a given temperature, the rate was higher the lower the CO to H_2 ratios was. The highest temperatures were an exception to this, here the rates for the low CO to H_2 ratios were limited as the CO was almost fully converted.

5.3.2 Particle size study

For the study of reactivity as a function of particle size, a series of microreactors were prepared with nanoparticles with sizes ranging from 3.2 to 9 nm. In order to be able to compare the results, all the samples were subjected to the exact same conditions. A long script was written with the purpose of measuring the reactivity at different temperatures and gas compositions, as well as the stability of the catalyst and the apparent activation energy. As earlier tests showed deactivation to some form of carbon growth at higher temperatures and higher CO to H_2 ratios, reactivation by treatment in pure O_2 at 200℃ at several points was introduced in the measurement series. H_2 alone was not able to remove the carbon species at pressures and temperatures achievable using this setup.

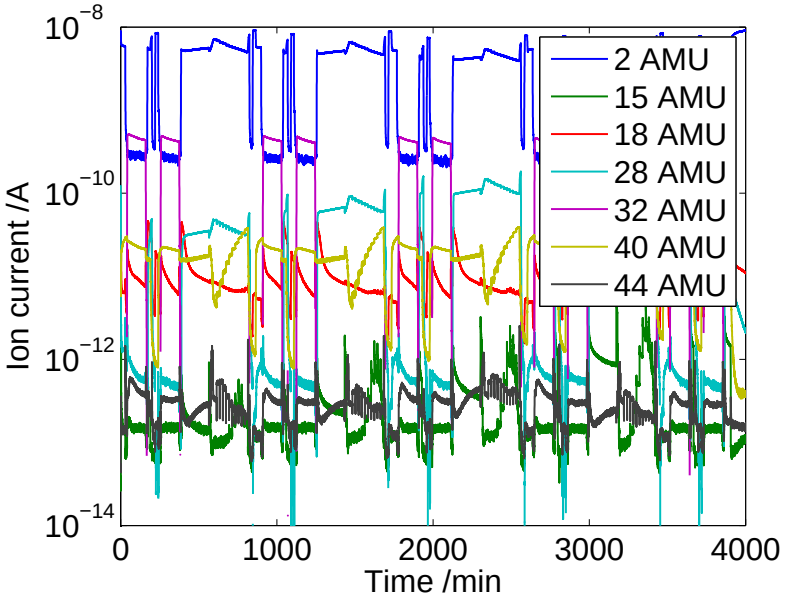

Figure 5.7: *Full mass spectrometer data as a function of time for a measurement on $1{\cdot}10^{10}$ 7 nm ruthenium nanoparticles in the study of reactivity as a function of nanoparticle size.*

The mass spectrometer data measured for such an experiment is shown in Fig. 5.7. This both shows the strength of having a fully automated setup allowing such comprehensive measurements, and also the need for thorough analysis afterwards to extract the relevant results. Figure 5.8 e.g., shows a plot with the methane signal extracted from the quick steps down in temperature plotted in an Arrhenius plot from which the apparent activation energy can be

calculated.

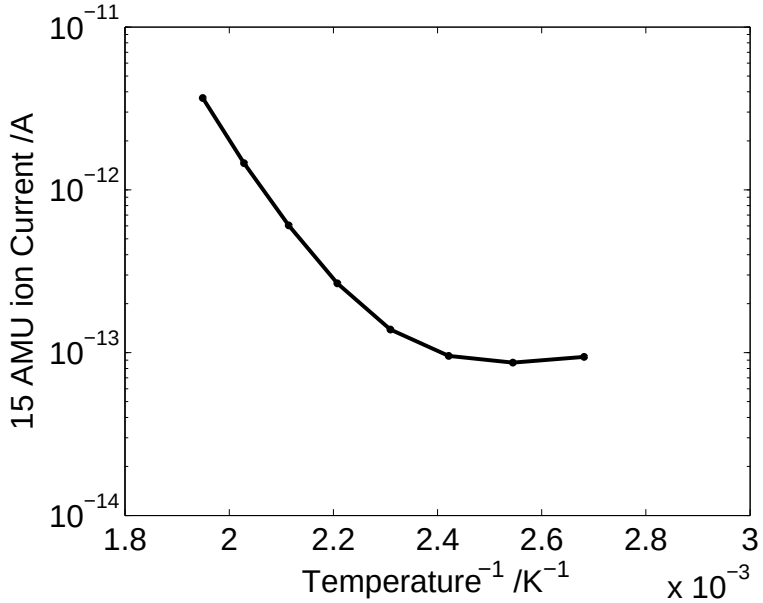

Figure 5.8: *An Arrhenius plot of a small sample of the data extracted from the fast steps down during the measurement shown in Fig. 5.7. The apparent activation energy found from this set of data was: E_a = 0.95 eV, which fits with values found in the literature [44, 48].*

For the comparison of the turn over frequency (TOF) of the CO methanation reaction on the nanoparticles as a function of particle size, the total number surface sites is needed for each sample, to convert the total rate measured into a TOF. By assuming that the nanoparticles were all perfect spheres with the given size, and the number of particles measured during the deposition was correct, a number for the total surface was calculated. Using this number together with the total methane production rate at 200℃, a TOF could be calculated for each sample. The result plotted as a function of particle size is seen in Fig. 5.9.

As the result did not seem to be very accurate (large unexplained jumps in TOF from size to size) together with the earlier discussed issues with the measurement of the number of particles, an attempt of calculating the surface area by another method was tried for a comparison. Figure 5.9 shows the ratio of the surface area obtained from a H_2 TPR after dosing CO (the details are discussed in the following section) to the surface area calculated from the number of particles. Again, with the apparent large uncertainty of the results and no clear trend in the TOF calculated from the H_2 TPR, it was

obvious that no clear conclusion to the reactivity as a function of particle size could be made with the current samples. And as changes to the nanoparticle source, correcting the nanoparticle beam and current measurement was planned, it was decided to postpone further testing until the modifications were implemented. At the time of writing the changes have been implemented and is in the process of being tested, opening up for a continuation of this study.

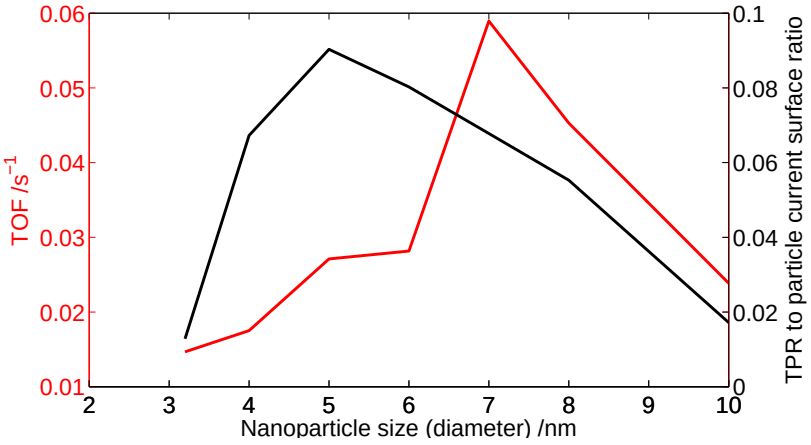

Figure 5.9: *(left y-axis): CO methanation TOF as a function of ruthenium nanoparticle size, with the ruthenium surface area calculated from the particle current measured during deposition. (right y-axis): Ratio of the surface area measured in H_2 TPR measurements after dosing CO to the surface area calculated from the particle current.*

5.3.3 H_2 TPR

Some effort was put into finding a good method for measuring the surface area of the ruthenium nanoparticles with the microreactor setup. CO TPD was tested as a method since we already had experience from UHV measurements on the ruthenium [49]. But even with very similar conditions to the UHV experiments, we never measured a CO signal in the mass spectrometer when expected. It was speculated that the reason for the problems was the very small volume of the microreactor causing multiple collisions of the desorbed molecules with the surface. The collisions result in readsorption and reaction causing carbon growth and diluting the signals too much for us to measure. Desorption of a full monolayer of molecules from the reactor chamber bottom corresponds to roughly 1 bar of gas because of the small volume.

Instead of a normal CO TPD, the heating step was performed in H_2, thereby reacting the CO off as methane instead of just desorbing.

Since methane is a much more stable molecule, it is much easier to measure in the mass spectrometer, as it will not adsorb on the way diluting the signal. Furthermore, the background in the mass spectrometer at 15 AMU was much lower than at 28 AMU, making much smaller signals of methane than CO measurable.

The experimental procedure for the TPR was the following. At elevated temperature (250℃), 1 bar of CO was led into the reactor to saturate the surface with CO for a couple of minutes, and the microreactor was then cooled down to 50℃ in CO. At 50℃ the CO was replaced by H_2 whereafter the microreactor was heated to 320℃ with a rate of roughly 1℃ /s while continuously measuring the methane signal in the mass spectrometer.

By comparing the surface area found by this method with the area found by the particle current measured during deposition (see Fig. 5.9), the much lower area of only a few percent found by the TPR method, indicates this method does not probe the full ruthenium surface, but only the step sites. If CO adsorbs on the full surface, but only dissociates at the steps leaving single C atoms [50], such that when the H_2 is introduced and temperature increased, methane can only be produced from the C on the steps, it would explain the low area measured. To get a better understanding of the mechanism behind the H_2 TPR measurements, a series of experiments were performed comparing the H_2 TPR after dosing CO, with H_2 TPR after dosing methane.

Figure 5.10 shows the results of six consecutive H_2 TPR measurements, every second measurement after dosing CO and the others after dosing methane. From this experiment a couple of things can be noted. The measurements were reproducible and features in the TPR can be resolved, even though a significant noise level is seen at these low ion currents. The number of methane molecules measured in both peaks are similar, indicating that both the CO and methane dose probes the same sites on the surface. Finally, a bit surprisingly the peak from the methane dose comes off at a higher temperature, suggesting that the adsorbed species are bound stronger. A likely reason for this is that the methane reacts when adsorbed, forming larger CH species that are more difficult to hydrogenate than the single C atoms.

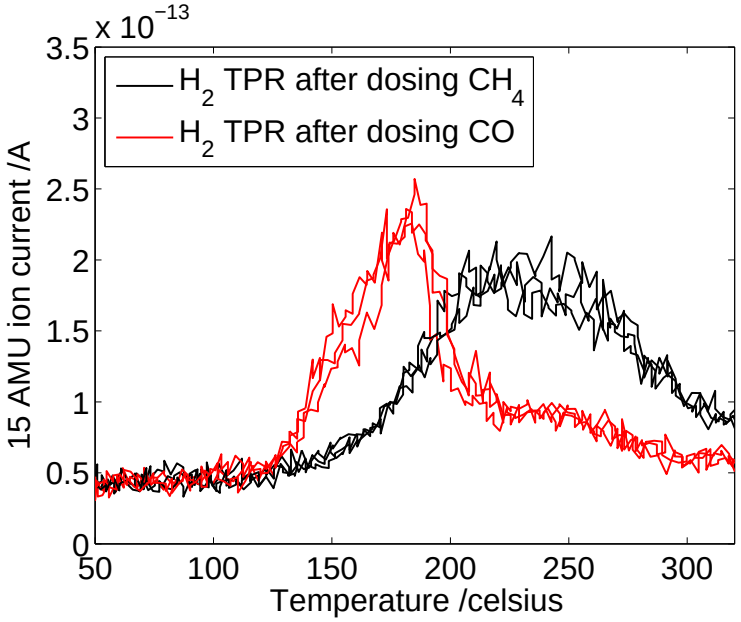

Figure 5.10: *The methane signal (15 AMU ion current) measured during H_2 TPR's after dosing either CO or CH_4 at 250℃ for 10 minutes.*

Figure 5.11 and 5.12 are the results from experiments where CO and methane was dosed at the same time, or one after the other, and where the dosing time was varied. By dosing both CO and methane at the same time, it is shown that CO does bind stronger than methane, thus blocking any methane from being adsorbed resulting in a TPR peak that was the same as for pure CO. The result from increasing the methane dose time, or dosing methane before or after CO, supports the idea that larger CH species which are harder to hydrogenate are formed, indicated by the later desorption. All the desorption peaks maintain a very similar total area except after increasing the time for the CO dose. After the long exposure to CO at high temperature, any subsequent TPR measurements show significantly lower methane signals. This must be an effect of blocking the active sites on the surface by strongly bound carbon species [51, 52], possibly graphite. Reactivation can be accomplished by treating in oxygen at high temperature producing CO_2 strengthening the claim of blocking by carbon species.

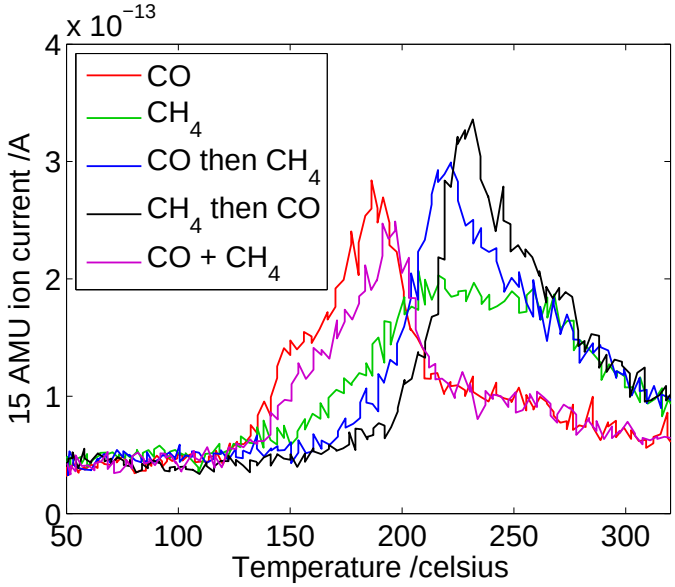

Figure 5.11: *The methane signal (15 AMU ion current) measured during H_2 TPR's after dosing combinations of CO and CH_4 at 250℃ for 10 minutes. For the two examples where one gas is dosed followed by the other, the total dosage time is double. The experiments were performed in the order shown in the legend without any cleaning of the catalyst in between.*

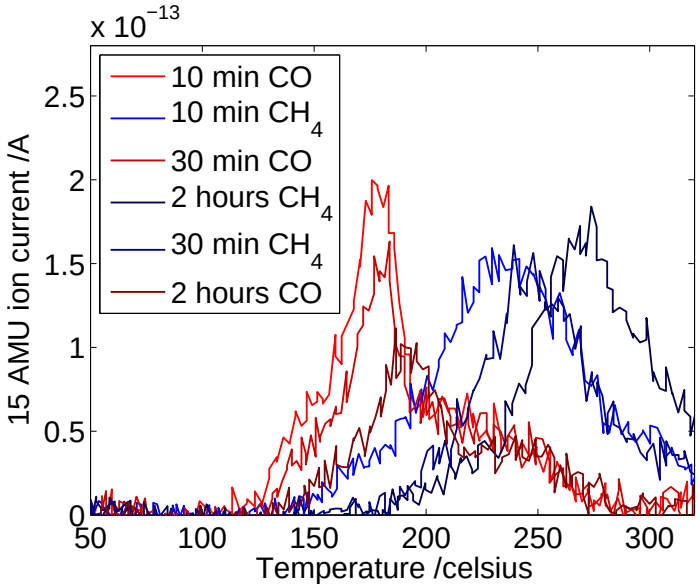

Figure 5.12: *The methane signal (15 AMU ion current) measured during H_2 TPR's after dosing either CO or CH_4 at 250℃ for various lengths of time. The experiments were performed in the order shown in the legend without any cleaning of the catalyst in between.*

The study of CO methanation on mass selected ruthenium nanoparticles presented in this chapter shows that measuring reactivity in the microreactor is possible. A parameter study found apparent activation energies from 0.8 to 1.2 eV depending on reaction conditions and a negative reaction order in CO concentration. Problems with estimating the surface area and therefore the TOF made comparisons between the samples with different particle size difficult.

Chapter 6

Other uses for the microreactor

In this chapter I will give an introduction to two other uses for the microreactor platform that were developed after initial testing of the system. Section 6.1 describes using the microreactors for photocatalytic testing, which can be performed without any modifications to the system. This is only a short description of how photocatalytic testing is performed and discussion of some of the experiments that have been done. Section 6.2 describes a modified version of the microreactor with a reaction chamber capable of liquid phase experiments with a gas flow similar to our standard microreactor. This two phase microreactor is still in the initial testing phase, so only a single measurement has been performed measuring water electrolysis.

6.1 Photocatalysis

By only looking at the dimensions of the microreactor, the advantage of using the microreactor system for photocatalysis becomes quite clear. The area open for illumination through the transparent pyrex lid[1] is the full reaction chamber area of 0.79 cm^2 and at the same time the reactor volume and related flow is only 236 nL and roughly $1 \cdot 10^{15}$ molecules per second. In other words, a microscopic volume and flow compared to a macroscopic illumination surface. This means that even for a catalyst with low activity, the reaction products can be measured as a function of time in a flow experiment.

[1] The pyrex lid has a transmission of above 90% at wavelengths down to around 300 nm.

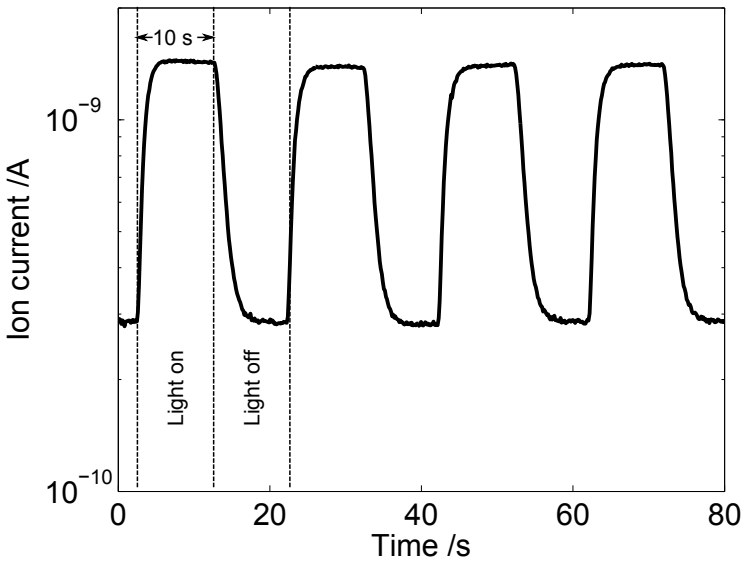

Figure 6.1: *Photocatalytic CO oxidation in the microreactor on P25 TiO_2. The UV light source was switched every 10 seconds. While the fast response time of the microreactor (a few seconds) gives very rapid changes in the CO_2 signal (44 AMU).*

Figure 6.1 shows the result of an experiment where TiO_2[2] was deposited in the microreactor[3] and then periodically illuminated by a UV light source while under a constant flow of a gas mixture of CO and O_2. The TiO_2 photocatalytically oxidizes the CO to CO_2 [53]. The CO_2 production can be calculated even with a quite high background in the mass spectrometer as the difference between the signal when the light is on and off eliminates the issue of having to estimate the background. From the figure, the high time resolution of the microreactor can be seen. Even with a 10 second time period between switching the light, only a fraction of this time is needed to reach the steady state level. The high time resolution makes detection of relative fast transient phenomenon possible, for example caused by mass transport effects in porus catalysts or photodesorption when illumination is switched on.

The high sensitivity of the microreactor from the high illumination area to volume ratio has several advantages, not only does it make measurements using catalysts with low activity possible, we have also taken advantage of it by measuring with light sources with large variation in light intensity. For example in an experiment with a monochromator in combination with a 1 kW Xenon arc lamp

[2]The commercial TiO_2 nanoparticles, P25 from Evonik where deposited in a similar manner to the $CuZnOAl_2O_3$ described in section 4.3.1.

[3]A microreactor with a wide capillary was chosen for the fast time response.

in order to measure a full action spectra with CO oxidation as a function of wavelength and the related quantum efficiency. In another experiment the microreactor was used to measure the reactivity as a function of light intensity over four order of magnitude, with the result that the reaction rate was of order 0.84 in light intensity and not 1 as expected.

The microreactor system has so far shown great versatility with respect to photocatalytic measurements, which was also the reason for developing the two phase reactor discussed in the next section, to be able to perform photoelectrocatalytic experiments.

6.2 Two phase microreactor

To perform liquid phase photocatalysis or any form of electrocatalytic experiments, it is necessary to have a liquid phase. To take advantage of the properties of the microreactor system while being able to do these kind of experiments, a new design was needed.

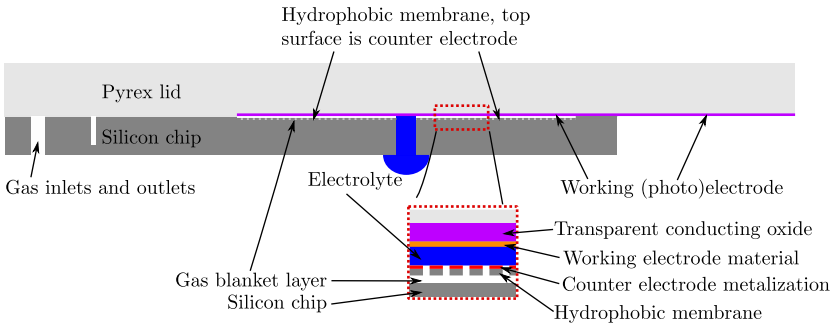

Figure 6.2: *Sketch of the design for the two phase microreactor setup for photoelectrocatalytic measurements.*

Figure 6.2 shows a sketch of the design we are currently working on finalizing. The currently missing parts are the photoelectrodes and the reference electrode. The basic concept of the design was to modify our standard microreactors such that the gas flow in the reaction chamber was moved below a gas permeable membrane blocking a liquid in the reaction chamber from entering the flow channels. Since the reaction chamber is only 3 μm deep, the diffusion distance for a reaction product through the electrolyte is maximum 3 μm. The short diffusion distance ensures that the time constant for measurements will be low, and no bubbles can be formed, causing problems for electric contact through the electrolyte.

For electrocatalytic experiments, the working and the counter electrodes could be placed on the pyrex lid and the reactor bottom,

contact to the botton one is possible through the silicon if the oxide layer is removed beforehand. For photoelectrocatalysis, the electrode on the pyrex lid would have to be transparent while still being conducting, the current candidate is indium tin oxide. As a reference electrode, Ag/AgCl is currently being tested.

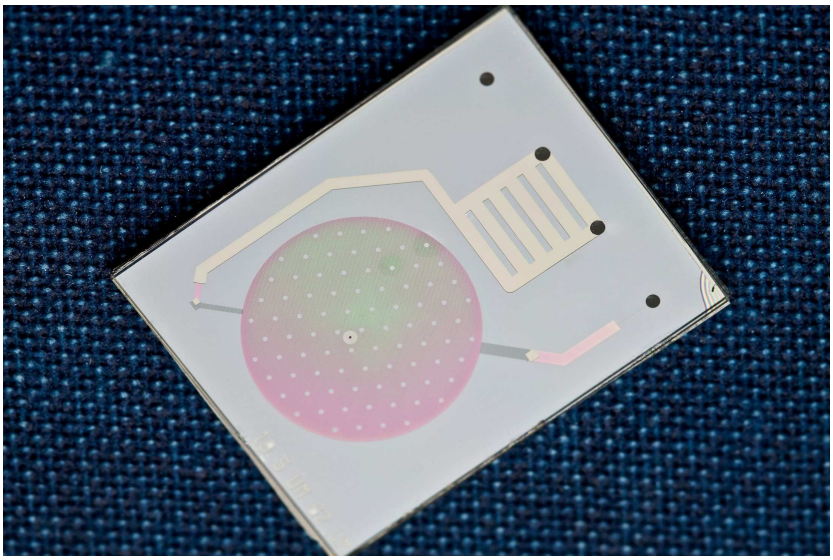

Figure 6.3: *A picture of a bonded microreactor. Because a SIO wafer is used, the main flow channels can only be etched down to a depth of 18 μm. To get a high enough flow conductance to use a similar main flow to the standard microreactor without getting a large pressure drop, the channels have been rearranged. The first inlet channel has been removed and a wide connection between the inlet and outlet has been made. The small dot slightly off center in the reaction chamber, is the injection hole for the electrolyte. The color difference seen in the reaction chamber is an artifact of the diffraction in the silicon membrane*

One complication with the design is that the electrolyte enters through a 100 μm wide hole etched through to the backside of the reactor, which during experiments is kept in constant contact with an electrolyte reservoir to keep the reaction chamber full. The complication comes from the fact that there are two barriers for the electrolyte: 1) from the reservoir to the reaction chamber, 2) from the reaction chamber to the flow channels. Since the electrolyte is supposed to fill the reaction chamber it has to overcome the barrier of the electrolyte injection hole, but it must on the other hand not surpass the barrier to the flow channels. Currently, it is a bit of a balance finding the optimal pressure in the system such that the electrolyte overcomes the first, but not the second barrier. A widening of the 100 μm wide electrolyte injection hole might resolve

this issue.

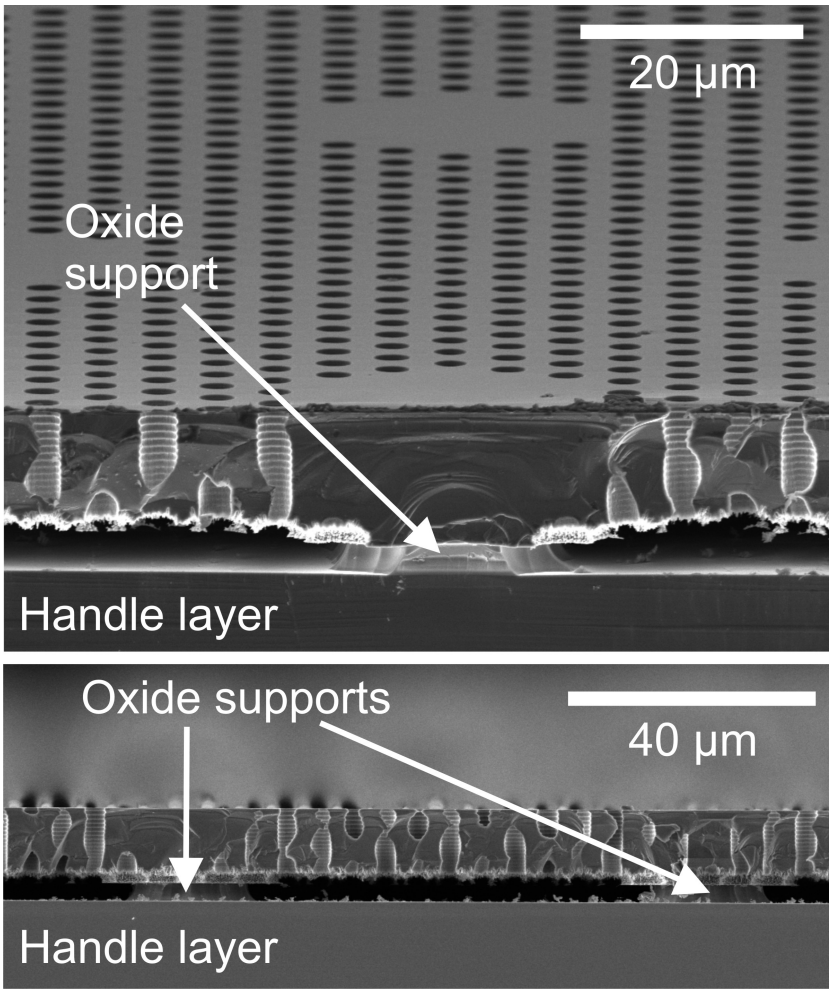

Figure 6.4: *SEM micrograph of a cut through the silicon membrane. The top surface will be coated in FDTS making the membrane hydrophobic, such that an electrolyte in the reaction chamber (on top of the membrane) can not enter the flow chamber (the gap between the two layers of silicon). The small 3 µm diameter holes etched through the membrane is what makes the membrane gas permeable.*

6.2.1 Silicon membrane

A key part of the two phase microreactor is the silicon membrane separating the flow chamber and the reaction chamber filled with an electrolyte. Figure 6.4 shows a SEM micrograph of a cut through a membrane. To fabricate the membrane a SOI[4] wafer is used instead of a standard silicon wafer, it has a 3 μm buried silicon oxide layer 15

[4]Semiconductor on insulator

μm below the surface. This buried oxide layer makes underetching possible by etching holes down to the oxide with a DRIE process followed by a HF dip removing the oxide exposed by the etched holes. In the figure, supporting pillars can also be seen, they ensure the thin and fragile membrane does not break during handling.

As the silicon membrane in itself is hydrophilic, and therefore not blocking water based electrolytes, a coating of FDTS[5] is applied to the membrane making the surface hydrophobic.

6.2.2 Electrolysis

The two phase microreactor was tested in a two electrode measurement of water electrolysis using 0.1 M $HClO_4$ as electrolyte. The electrodes sketched in Fig. 6.5 was made in the same way as the platinum RTD described in section 2.2.2, and to avoid degradation of the FDTS coating, the lid was cold bonded to a two phase microreactor.

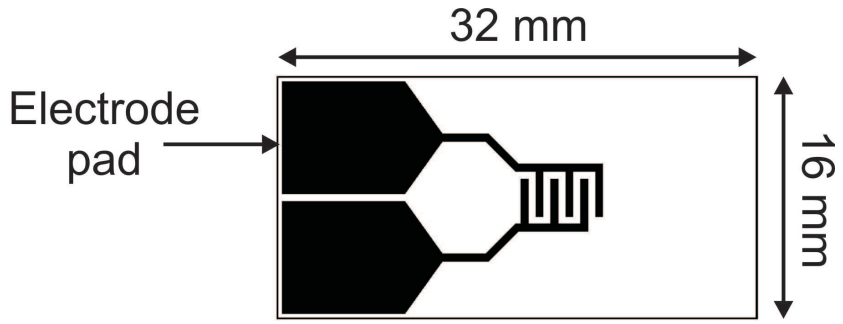

Figure 6.5: *Sketch of the layout for the electrodes for the water electrolysis experiment. The electrodes were made of a 100 μm platinum thin film.*

During the experiment a flow of N_2 was continuously led through the microreactor at a pressure of around 1.5 bar, keeping the electrolyte out of the flow chamber, but still inside the reaction chamber. The voltage difference between the two electrodes were scanned from -2 to 2 V at a rate of 20 mV/s while the current and the H_2 and O_2 signals were monitored. The results of the experiment plotted as a function of time can be seen in Fig. 6.6. At around 1.5 V difference between the two electrodes, both O_2 and H_2 are evolved, and as both electrodes are located in the reaction chamber of the microreactor, both signals are recorded simultaneously in the mass spectrometer. Only a slight asymmetry at low current is seen, caused by mass transport limitations in the reactor.

[5] Perfluorodecyltrichlorosilane

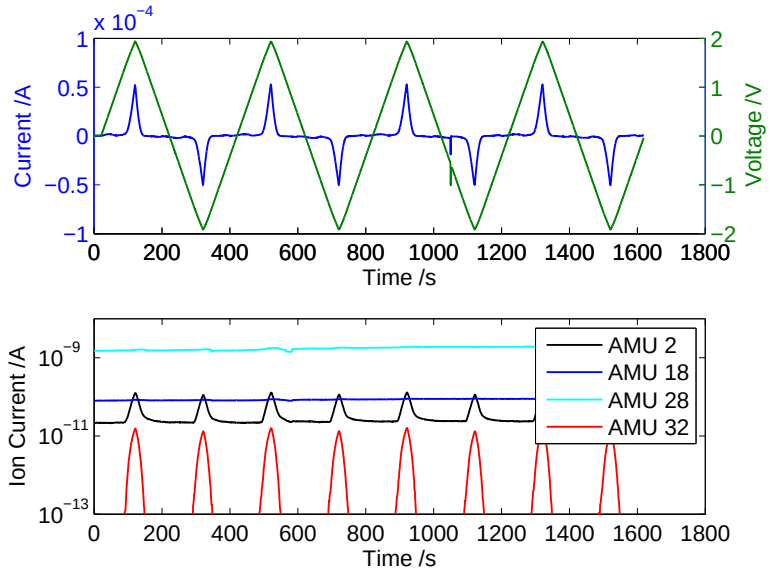

Figure 6.6: *The results of a two electrode water electrolysis experiment in the two phase microreactor where the voltage was scanned between -2 and 2 V with a rate of 20 mV/s with a 0.1 M $HClO_4$ electrolyte. (Top): The current passing through the two electrodes and the supplied voltage. (Bottom): The ion currents measured in the mass spectrometer.*

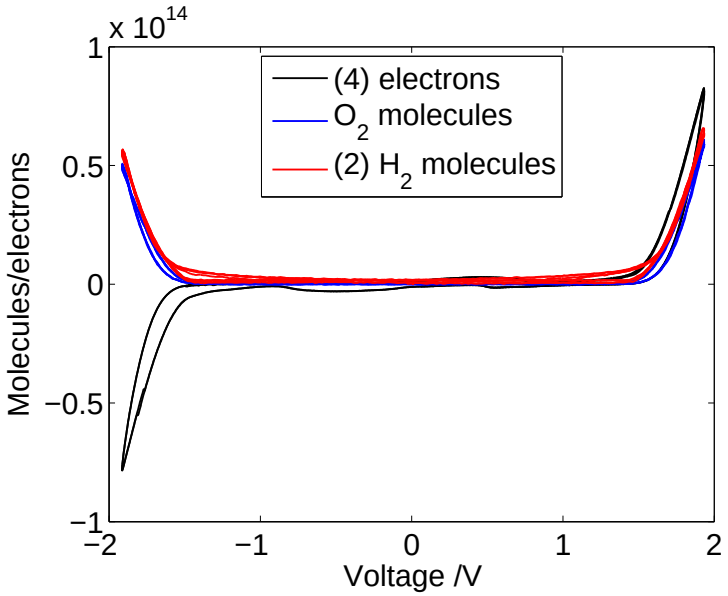

Figure 6.7: *IV plot of the current passing through the electrodes in the water electrolysis experiment shown in Fig. 6.6 together with the measured ion currents of O_2 and H_2 with the background subtracted. The signals plotted correspond to the number of molecules/electrons per reaction.*

Figure 6.7 is a plot of the same dataset, where the current is converted into number of electrons per reaction (4) and the O_2 and H_2 signals are converted to the number of O_2 and H_2 molecules being evolved per reaction (1 and 2). From this plot it can be seen that the O_2 and H_2 molecules are measured in stoichiometric amounts as expected, and the system is stable during several scans. Also the number of electrons is only slightly higher than expected from the amount of water splitting measured. The low leak current is possibly caused by recombination, since both O_2 and H_2 are evolved in the same chamber.

The experiment shows a good potential for the very small electrochemical cell, which has the big advantage that the reaction products are measured simultaneously with the current, thus, eliminating questions about the origin of measured features in the current. Currently planned are three electrode experiments with electrochemical reduction of CO_2 on Cu, as the reactor should be well suited to detect the reaction products as a function of voltage. Testing of photoelectrocatalysis is also planned.

Chapter 7

Conclusion and outlook

The chapters up until this point has described work done during my PhD, designing the microreactor system and the different catalytic reaction that was tested on it.

A lot of work was put into redesigning the previous setup used for microreactor testing and many improvements was made. The whole gas handling system was rebuilt, including the steel gas manifold for interfacing with the microreactor, and is now UHV compatible. The only exception is the O-rings, for which an argon flush was designed, eliminating most of the problems using non metal seals. At the same time the system was rebuilt, the different parts were all interfaced with a PC, and a LabVIEW program for control of the temperature, the gas system, and the mass spectrometer was written. This was perhaps the biggest improvement of the system. Now long measurement series can be scripted, for more efficient and precise use of the system.

The experiments with CO oxidation on platinum thin films successfully showed the high sensitivity of the microreactor, measuring activity on as little as 15 μm^2 platinum thin film catalyst. A study of the light off phenomenon showed promise as a method for determining the platinum surface area in the microreactor using light off at room temperature in extreme oxygen surplus.

The study of transients in methanol synthesis on a CuZnO catalyst with pretreatment in a CO and H_2 gas mixtures was able to reproduce results, showing a maximum in increased transient methanol production with a one to one ratio of CO to H_2 in the pretreatment gas. Understanding this effect proved difficult, but some results came out of experiments with the highly active state of the catalyst after pretreatment. It was shown that even two hours of pretreatment at 180℃, more pretreatment still had an effect, and at lower temperature, the activation of the catalyst happened slower.

The stability of the active state was also tested, and it was found that a quick increase to 240℃ in vacuum removed any evidence of the pretreatment. A surprising methanol production at 60℃ of the catalyst when in the highly active state was discovered, showing the great potential if the effect of the pretreatment can be stabilized. A study of formate TPD measurements as a method of probing the catalyst surface in order to find correlations with the transient methanol production was not concluded. But work with methanol synthesis in the microreactor is continued with among other things looking at the effect of the support.

The main goal, of looking at size selected nanoparticles to study the relation between particle size and its reactivity, was only partly completed. CO methanation on size selected ruthenium nanoparticles was successfully measured, and a parameter study showed a negative reaction order in CO concentration and an activation energy of 0.8-1.2 eV depending on the reaction conditions. Problems with the nanoparticle source made accurate estimation of the number of particles impossible, complicating comparisons from sample to sample. Tests with H_2 TPR measurements after dosing CO or methane at high temperature showed promise for determining the catalyst area by measuring the carbon deposited during dosing. It is still an open question if the TPR measurements probe the full surface or only the step sites. Recently the nanoparticle source has been modified to solve the problems with measuring the number of nanoparticles deposited, promising successful continuation of this work.

Collaboration with the group of Richard Palmer [54] and with the group of Ulrich Heiz [55] has also been started, with the purpose of using our microreactor system to measured the reactivity of size selected nanoparticles from the sources in the two groups. Initial tests looks promising.

The development of a new two has microreactor has been a great success. Initial tests with water electrolysis with simultaneous measurement of the produced H_2 and O_2 and the current showed a nice agreement between the different signals. Continued development of the system as a small cell for electrochemistry and photoelectrochemistry has a lot of potential.

Bibliography

[1] I. Chorkendorff and J Niemantsverdriet. *Concepts of modern catalysis and kinetics*. John Wiley & Sonds, 2003.

[2] U.S. Energy Information Administration. International energy outlook 2010, 2010.

[3] AT Bell. The impact of nanoscience on heterogeneous catalysis. *SCIENCE*, 299(5613):1688–1691, MAR 14 2003.

[4] Jens K. Norskov, Thomas Bligaard, Britt Hvolbaek, Frank Abild-Pedersen, Ib Chorkendorff, and Claus H. Christensen. The nature of the active site in heterogeneous metal catalysis. *CHEMICAL SOCIETY REVIEWS*, 37(10):2163–2171, OCT 2008.

[5] S Dahl, A Logadottir, RC Egeberg, JH Larsen, I Chorkendorff, E Tornqvist, and JK Norskov. Role of steps in N-2 activation on Ru(0001). *PHYSICAL REVIEW LETTERS*, 83(9):1814–1817, AUG 30 1999.

[6] G Wulff. On the question of speed of growth and dissolution of crystal surfaces. *ZEITSCHRIFT FUR KRYSTALLOGRAPHIE UND MINERALOGIE*, 34(5/6):449–530, MAR 1901.

[7] R. Imbihl, R. J. Behm, and R. Schloegl. Bridging the pressure and material gap in heterogeneous catalysis. *PHYSICAL CHEMISTRY CHEMICAL PHYSICS*, 9(27):3459, 2007.

[8] H Pfnur, G Held, M Lindroos, and D Menzel. Oxygen induced reconstruction of a close-packed surface - a LEED-IV study on ru(001)-p(2x1)o. *SURFACE SCIENCE*, 220(1):43–58, OCT 1989.

[9] BJ McIntyre, M Salmeron, and GA Somorjai. In-situ scanning-tunneling-microscopy study of platinum (110) in a reactor cell at high-pressures and temperatures. *JOURNAL OF VACUUM SCIENCE & TECHNOLOGY A-VACUUM SURFACES*

AND FILMS, 11(4, Part 2):1964–1968, JUL-AUG 1993. 39TH NATIONAL SYMP OF THE AMERICAN VACUUM SOC, CHICAGO, IL, NOV 09-13, 1992.

[10] KF Jensen. Microreaction engineering - is small better? *CHEMICAL ENGINEERING SCIENCE*, 56(2):293–303, JAN 2001. 16th International Symposium on Chemical Reaction Engineering, KRAKOW, POLAND, SEP 10-13, 2000.

[11] SK Ajmera, C Delattre, MA Schmidt, and KF Jensen. Microfabricated cross-flow chemical reactor for catalyst testing. *SENSORS AND ACTUATORS B-CHEMICAL*, 82(2-3):297–306, FEB 28 2002.

[12] G Kolb and V Hessel. Micro-structured reactors for gas phase reactions. *CHEMICAL ENGINEERING JOURNAL*, 98(1-2):1–38, MAR 15 2004.

[13] L Kiwi-Minsker and A Renken. Microstructured reactors for catalytic reactions. *CATALYSIS TODAY*, 110(1-2):2–14, DEC 15 2005.

[14] U Heiz and EL Bullock. Fundamental aspects of catalysis on supported metal clusters. *JOURNAL OF MATERIALS CHEMISTRY*, 14(4):564–577, FEB 21 2004.

[15] D. Wayne Goodman. Chemistry - Precious little catalyst. *NATURE*, 454(7207):948–949, AUG 21 2008.

[16] K Wong, S Johansson, and B Kasemo. Nanofabricated model catalysts - Manufacturing and model studies. *FARADAY DISCUSSIONS*, 105:237–246, 1996. Meeting on Catalysis and Surface Science at High Resolution, READING, ENGLAND, DEC 16-18, 1996.

[17] AS Eppler, G Rupprechter, L Guczi, and GA Somorjai. Model catalysts fabricated using electron beam lithography and pulsed laser deposition. *JOURNAL OF PHYSICAL CHEMISTRY B*, 101(48):9973–9977, NOV 27 1997.

[18] S Pratontep, SJ Carroll, C Xirouchaki, M Streun, and RE Palmer. Size-selected cluster beam source based on radio frequency magnetron plasma sputtering and gas condensation. *REVIEW OF SCIENTIFIC INSTRUMENTS*, 76(4), APR 2005.

[19] B Klipp, M Grass, J Muller, D Stolcic, U Lutz, G Gantefor, T Schlenker, J Boneberg, and P Leiderer. Deposition of mass-selected cluster ions using a pulsed arc cluster-ion source. *APPLIED PHYSICS A-MATERIALS SCIENCE & PROCESSING*, 73(5):547–554, NOV 2001.

[20] KF Jensen. Silicon-based microchemical systems: Characteristics and applications. *MRS BULLETIN*, 31(2):101–107, FEB 2006.

[21] AM Hynes, H Ashraf, JK Bhardwaj, J Hopkins, I Johnston, and JN Shepherd. Recent advances in silicon etching for MEMS using the ASE (TM) process. *SENSORS AND ACTUATORS A-PHYSICAL*, 74(1-3):13–17, APR 20 1999. Symposium H - Materials Aspects in Microsystem Technologies, STRASBOURG, FRANCE, JUN 16-19, 1998.

[22] G Wallis and Pomerant.di. Field assisted glass-metal sealing. *JOURNAL OF APPLIED PHYSICS*, 40(10):3946–&, 1969.

[23] K. M. Knowles and A. T. J. van Helvoort. Anodic bonding. *INTERNATIONAL MATERIALS REVIEWS*, 51(5):273–311, OCT 2006.

[24] TR Anthony. Anodic bonding of imperfect surfaces. *JOURNAL OF APPLIED PHYSICS*, 54(5):2419–2428, 1983.

[25] KB Albaugh. Electrode phenomena during anodic bonding of silicon to sodium borosilicate glass. *JOURNAL OF THE ELECTROCHEMICAL SOCIETY*, 138(10):3089–3094, OCT 1991.

[26] Pfeiffer Vacuum. *Mass spectrometer 2002-2004.*

[27] Honeywell, Sensing and Control. *Platinum RTDs, Temperature Sensors.*

[28] SL Firebaugh, KF Jensen, and MA Schmidt. Investigation of high-temperature degradation of platinum thin films with an in situ resistance measurement apparatus. *JOURNAL OF MICROELECTROMECHANICAL SYSTEMS*, 7(1):128–135, MAR 1998.

[29] A. Roth. *Vacuum Technology.* Elsevier, 3rd edition, 1990.

[30] J. O'Hanlon. *A User's Guide to Vacuum Technology.* Wiley, 3rd edition, 2003.

[31] M. S. Chen, Y. Cal, Z. Yan, K. K. Gath, S. Axnanda, and D. Wayne Goodman. Highly active surfaces for CO oxidation on rh, pd, and pt. *SURFACE SCIENCE*, 601(23):5326–5331, DEC 1 2007.

[32] A. M. Contreras, X. M. Yan, S. Kwon, J. Bokor, and G. A. Somorjai. Catalytic CO oxidation reaction studies on lithographically fabricated platinum nanowire arrays with different oxide supports. *CATALYSIS LETTERS*, 111(1-2):5–13, OCT 2006.

[33] S Johansson, E Fridell, and B Kasemo. Microreactor for studies of low surface area model catalysts made by electron-beam lithography. *JOURNAL OF VACUUM SCIENCE & TECHNOLOGY A-VACUUM SURFACES AND FILMS*, 18(4, Part 1):1514–1519, JUL-AUG 2000. 46th National Symposium of the American-Vacuum-Society, SEATTLE, WASHINGTON, OCT 25-29, 1999.

[34] PW Jacobs, SJ Wind, FH Ribeiro, and GA Somorjai. Nanometer size platinum particle arrays: Catalytic and surface chemical properties. *SURFACE SCIENCE*, 372(1-3):L249–L253, FEB 10 1997.

[35] JD Grunwaldt, AM Molenbroek, NY Topsoe, H Topsoe, and BS Clausen. In situ investigations of structural changes in Cu/ZnO catalysts. *JOURNAL OF CATALYSIS*, 194(2):452–460, SEP 10 2000.

[36] Peter C. K. Vesborg, Ib Chorkendorff, Ida Knudsen, Olivier Balmes, Jesper Nerlov, Alfons M. Molenbroek, Bjerne S. Clausen, and Stig Helveg. Transient behavior of Cu/ZnO-based methanol synthesis catalysts. *JOURNAL OF CATALYSIS*, 262(1):65–72, FEB 15 2009.

[37] GA Olah. Beyond oil and gas: The methanol economy. *ANGEWANDTE CHEMIE-INTERNATIONAL EDITION*, 44(18):2636–2639, 2005.

[38] PB Rasmussen, PM Holmblad, T Askgaard, CV Ovesen, P Stoltze, JK Norskov, and I Chorkendorff. Methanol synthesis on cu(100) from a binary gas-mixture of CO2 and H2. *CATALYSIS LETTERS*, 26(3-4):373–381, 1994.

[39] J Yoshihara and CT Campbell. Methanol synthesis and reverse water-gas shift kinetics over Cu(110) model catalysts: Structural

sensitivity. *JOURNAL OF CATALYSIS*, 161(2):776–782, JUL 1996.

[40] J Nerlov, S Sckerl, J Wambach, and I Chorkendorff. Methanol synthesis from CO2, CO and H-2 over Cu(100) and Cu(100) modified by Ni and Co. *APPLIED CATALYSIS A-GENERAL*, 191(1-2):97–109, JAN 24 2000.

[41] Y. Yang, C. A. Mims, R. S. Disselkamp, C. H. F. Peden, and C. T. Campbell. Simultaneous MS-IR Studies of Surface Formate Reactivity Under Methanol Synthesis Conditions on Cu/SiO2. *TOPICS IN CATALYSIS*, 52(10):1440–1447, SEP 2009.

[42] H Wilmer and O Hinrichsen. Dynamical changes in Cu/ZnO/Al2O3 catalysts. *CATALYSIS LETTERS*, 82(1-2):117–122, SEP 2002.

[43] Paul Sabatier and J.-B. Senderens. New methane synthesis. *COMPTES RENDUS HEBDOMADAIRES DES SEANCES DE L ACADEMIE DES SCIENCES*, 134:514–516, 1902.

[44] MA Vannice. Catalytic synthesis of hydrocarbons from H2-CO mixtures over group-8 metals .1. specific activities and product distributions of supported metals. *JOURNAL OF CATALYSIS*, 37(3):449–461, 1975.

[45] Haldor Topsoe A/S. *Low temperature methanation catalyst pk-7r*.

[46] M. P. Andersson, E. Abild-Pedersen, I. N. Remediakis, T. Bligaard, G. Jones, J. Engbwk, O. Lytken, S. Horch, J. H. Nielsen, J. Sehested, J. R. Rostrup-Nielsen, J. K. Norskov, and I. Chorkendorff. Structure sensitivity of the methanation reaction: H-2-induced CO dissociation on nickel surfaces. *JOURNAL OF CATALYSIS*, 255(1):6–19, APR 1 2008.

[47] T Zubkov, GA Morgan, and JT Yates. Spectroscopic detection of CO dissociation on defect sites on Ru(109): implications for Fischer-Tropsch catalytic chemistry. *CHEMICAL PHYSICS LETTERS*, 362(3-4):181–184, AUG 19 2002.

[48] IG Bajusz and JG Goodwin. Hydrogen and temperature effects on the coverages and activities of surface intermediates during methanation on Ru/SiO2. *JOURNAL OF CATALYSIS*, 169(1):157–165, JUL 1 1997.

[49] S. B. Vendelbo, M. Johansson, D. J. Mowbray, M. P. Andersson, F. Abild-Pedersen, J. H. Nielsen, J. K. Norskov, and I. Chorkendorff. Self Blocking of CO Dissociation on a Stepped Ruthenium Surface. *TOPICS IN CATALYSIS*, 53(5-6):357–364, MAY 2010.

[50] FM Hoffmann. The kinetics of CO dissociation on ru(001) - time-resolved vibrational spectroscopy at elevated pressures. *JOURNAL OF CHEMICAL PHYSICS*, 90(5):2816–2823, MAR 1 1989.

[51] DW Goodman and JM White. Measurement of active-carbon on ruthenium(110) - relevance to catalytic methanation. *SURFACE SCIENCE*, 90(1):201–203, 1979.

[52] T Zubkov, GA Morgan, JT Yates, O Kuhlert, M Lisowski, R Schillinger, D Fick, and HJ Jansch. The effect of atomic steps on adsorption and desorption of CO on Ru(109). *SURFACE SCIENCE*, 526(1-2):57–71, FEB 20 2003.

[53] Tracy L. Thompson and John T. Yates, Jr. Surface science studies of the photoactivation of TiO2-new photochemical processes. *CHEMICAL REVIEWS*, 106(10):4428–4453, OCT 11 2006.

[54] Prof. Richard Palmer. University of birmingham, uk.

[55] Prof. Ulrich Heiz. Technische universität münchen.

Paper I

Highly sensitive silicon microreactor for catalyst testing
Toke R. Henriksen, Jakob L. Olsen, Peter Vesborg, Ib Chorkendorff, and Ole Hansen
Review of Scientific Instruments **80**, 124101, (2009)

Highly sensitive silicon microreactor for catalyst testing

Toke R. Henriksen,[1,2] Jakob L. Olsen,[2] Peter Vesborg,[2] Ib Chorkendorff,[2] and Ole Hansen[1,2,a)]

[1]*Department of Micro- and Nanotechnology, Technical University of Denmark, DTU Nanotech Building 345 East, DK-2800 Kgs. Lyngby, Denmark*

[2]*Department of Physics, Danish National Research Foundation's Center for Individual Nanoparticle Functionality (CINF), Technical University of Denmark, Building 312, DK-2800 Kgs. Lyngby, Denmark*

(Received 14 July 2009; accepted 6 November 2009; published online 7 December 2009)

A novel microfabricated chemical reactor for highly sensitive measurements of catalytic activity and surface kinetics is presented. The reactor is fabricated in a silicon chip and is intended for gas-phase reactions at pressures ranging from 0.1 to 5.0 bar. A high sensitivity is obtained by directing the entire gas flow through the catalyst bed to a mass spectrometer, thus ensuring that nearly all reaction products are present in the analyzed gas flow. Although the device can be employed for testing a wide range of catalysts, the primary aim of the design is to allow characterization of model catalysts which can only be obtained in small quantities. Such measurements are of significant fundamental interest but are challenging because of the low surface areas involved. The relationship between the reaction zone gas flow and the pressure in the reaction zone is investigated experimentally. A corresponding theoretical model is presented, and the gas flow through an on-chip flow-limiting capillary is predicted to be in the intermediate regime. The experimental data for the gas flow are found to be in good agreement with the theoretical model. At typical experimental conditions, the total gas flow through the reaction zone is around 3×10^{14} molecules s^{-1}, corresponding to a gas residence time in the reaction zone of about 11 s. To demonstrate the operation of the microreactor, CO oxidation on low-area platinum thin film circles is employed as a test reaction. Using temperature ramping, it is found that platinum catalysts with areas as small as 15 μm^2 are conveniently characterized with the device. © *2009 American Institute of Physics.*
[doi:10.1063/1.3270191]

I. INTRODUCTION

In heterogeneous catalysis, the discovery, characterization, and optimization of catalysts require extensive experimentation and are critical steps in the development of new chemical processes. Traditionally, macroscale chemical reactors such as the idealized plug flow reactor have been used for catalyst testing.[1] As a supplement to these traditional reactors, microfabricated reactors have, in recent years, shown promise as versatile analytical tools for measuring catalytic activity. Microfabricated reactors, also known as microreactors, are chemical reactors with dimensions in the micrometer range. Pioneered by, among others, Jensen *et al.*, microreactors have been shown to offer a number of advantages compared to conventional macroscale reactors.[2–6] The temperature of a microreactor can be varied easily and quickly because of the small size. Due to the high surface-to-volume ratio, heat transfer to and from the reaction zone is greatly enhanced. This reduces thermal gradients in the reactor and makes accurate control of temperature possible, even for strongly exothermic reactions. Furthermore, the small dimensions of the reactor improve mass transfer and reduce concentration gradients. Small thermal and concentration gradients are favorable when determining kinetic data. Reaction parameters such as pressure, residence time, and flow rate are more easily controlled in reactions that take place in small volumes. In addition to these advantages, the small scale of the reactor improves safety of use for explosive mixtures and greatly reduces reactant gas consumption. Finally, it is possible to integrate heaters and sensors directly into microreactors using microfabrication technology.

Fundamentally, a microreactor consists of a system of microchannels in which the reactants will flow and react. The flow through the microchannels is mostly laminar, resulting in predictable and well-controlled flow patterns. Due to the small dimensions, the residence time of the reactant gas in the catalyst bed is typically low. Consequently, high space velocities can be obtained.

In combination with an appropriate instrument for gas composition analysis, it is possible to design microreactors which facilitate detection of very small amounts of gas phase products. This is a consequence of the low flow rate through the microchannel system. High sensitivity product detection under atmospheric pressure is useful in several respects. When investigating new, nonoptimized catalysts, the catalytic activity might be low, necessitating detection of small amounts of substances. Furthermore, some model catalysts, such as mass selected clusters and catalysts fabricated using electron-beam lithography (EBL), can only be obtained in small quantities. Thus, a sensitive experimental arrangement is required for measuring the catalytic activity of such samples.[7–9]

a)Electronic mail: ole.hansen@nanotech.dtu.dk.

A few microreactors for low-area catalyst characterization with gas-phase reactions have been reported in literature. Johansson *et al.*[9] demonstrated a Pyrex flow microreactor for measuring catalytic activity of nanofabricated model catalysts at atmospheric pressure. The microreactor had a reaction chamber volume of around 100 mm^3, a reaction zone gas flow of about 4×10^{16} molecules s^{-1}, and a gas residence time in the reaction zone of approximately 60 s. They observed CO oxidation on a platinum wire with a surface area of 0.3 mm^2. Jacobs *et al.*[10] measured ethylene hydrogenation at atmospheric pressure in a closed tank reactor. They detected catalytic activity on an EBL-nanofabricated platinum model catalyst with a total active surface area of 4 mm^2.

Our research group has previously fabricated microreactors and applied them in experiments concerning catalysis and surface science.[11–14] In this paper, we present a novel continuous-flow microreactor with a highly improved sensitivity for measurements of catalytic activity. The device is intended for gas-phase reactions at pressures in the range of 0.1–5.0 bar. The gas composition is analyzed using a quadropole mass spectrometer (QMS). As a characteristic feature, the microreactor presented here directs the entire reaction zone gas flow to enter the mass spectrometer. This increases the sensitivity considerably compared to traditional microreactors where only a small fraction of the gas flow is analyzed.

The microreactor is designed as an analytical tool for catalyst testing. In this context, the term *catalyst testing* covers measurements of catalytic activity, turnover frequency, apparent activation energy, and surface area, as a result of temperature programmed desorption and experiments with conversion rate as a function of temperature and gas phase stoichiometry. The high sensitivity of the reactor makes it especially well-suited for fundamental catalytic activity studies of model catalysts with low surface areas. A particularly important application is the characterization of mass selected metal clusters with a narrow size distribution. Such measurements are of significant interest for the purpose of correlating size and catalytic activity of clusters.[15–17] Often, a low density of clusters is desirable in these studies to suppress sintering effects. Ensembles of metal clusters can be produced with a magnetron sputtering cluster source, but only in small quantities per unit time, since the cluster beam intensity decreases with reduced spread in the cluster size. Thus, a highly sensitive measurement technique, like the one presented here, could substantially reduce the time consumption of such experiments.

Although the high sensitivity is particularly advantageous for fundamental studies involving small quantities of model catalysts, the microreactor is not restricted to such experiments. In addition to deposition from a cluster source, catalyst samples can be introduced into the reactor using a variety of other methods, including flame spray deposition,[18] dip-coating, spin coating, or manual deposition with a pipette. During catalyst deposition, a shadow mask can be used to confine deposition to the reaction chamber area. Any catalyst, which can be deposited with these methods and which can fit in the reaction chamber, can be tested with the device.

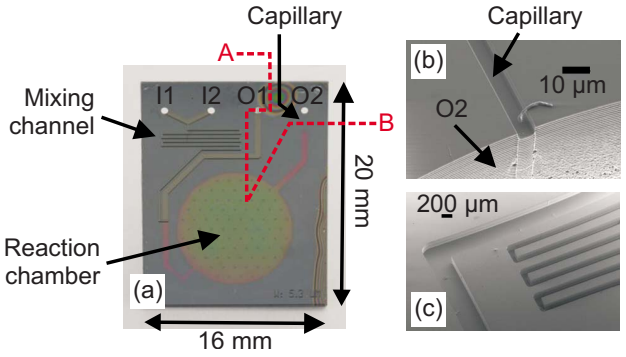

FIG. 1. (Color online) (a) Photograph of reactor showing the two inlets I1 and I2 and the two outlets O1 and O2. The dashed red line signifies the cross section shown in the process flow in Fig. 2. (b) Scanning electron micrograph of the junction between the capillary and the outlet O2. (c) Scanning electron micrograph of the mixing channel.

For example, many industrial catalysts with promoters, metal alloys, oxides, and supports can be conveniently tested with the microreactor.

In the work presented here, CO oxidation on circular platinum thin films of different areas is employed as a test reaction. The aim of these experiments is to demonstrate the operation of the reactor and the ability to characterize low-area catalysts. While platinum thin films are not used as CO oxidation catalysts for practical purposes, they are often used as model systems and for test reactions in fundamental catalysis studies.[19,20] Platinum thin films produced using electron-beam (e-beam) physical vapor deposition (PVD) and a lift-off process in acetone are used in this work because this is a convenient way of preparing catalysts with well controlled surface areas in the range 10–10 000 μm^2. The relation between the area of the catalyst circle and the lowest temperature at which catalytic activity can be detected in the QMS is investigated with reference to determining the sensitivity of the microreactor.

II. EXPERIMENTAL

A. Microreactor design

The microreactor directs the entire gas flow through the catalyst bed to a QMS, ensuring that almost all reaction products are present in the analyzed gas flow. Thus, unnecessary dilution of products is avoided, resulting in a high sensitivity. This concept places the following demands on the microreactor design: (1) the flow rate through the catalyst bed must be small, since gas can only be allowed to enter the QMS at a low rate. (2) Because of the low gas flow rate, the reaction zone volume must be small to ensure a relatively short gas residence time.

The microreactor consists of a microchannel system which has been formed in a silicon chip using reactive ion etching (RIE) and deep RIE (DRIE). DRIE is a technique with which deep and narrow structures with vertical sidewalls can be etched in silicon.[21] The chip has dimensions of 16×20 $mm^2\times350$ μm, as shown in Fig. 1. The channel system includes two inlets (I1 and I2), through which two different reactant gas mixtures can be introduced and mixed on-chip. In addition, two outlets (O1 and O2) are included in

the chip. The inlets and outlets all consist of 600 μm diameter holes which extend from the front side to the back of the chip. The two inlets are connected to a mixing channel of depth 250 μm. To make certain that the two reactant gas mixtures are properly mixed when entering the reaction zone, the mixing channel has a long meander structure and a width of only 150 μm. The mixing channel connects to O1 through a channel with the same depth as the mixing channel. To achieve a high flow conductance, this channel has a width of 500 μm. The gas flow through the mixing channel enters the chip through I1 and I2 and leaves the microreactor through O1. This gas flow is typically on the order of 10 Nml min^{-1} (4.1×10^{18} molecules s^{-1}).

A channel leads from the mixing channel to a circular reaction chamber with a diameter of 1.0 cm, and another channel leads from the reaction chamber to O2. These two channels as well as the reaction chamber all have depths of only 3 μm. In experiments, the catalyst is contained within the reaction chamber, and the chemical reaction occurs here. Gas flows from the mixing channel into the reaction chamber and proceeds to O2. The low depth yields a reaction chamber volume of only 240 nl. The purpose of the shallow channel connecting the mixing channel to the reaction chamber is to limit back-diffusion of reaction products to the mixing channel. O2 is connected to a QMS, which analyzes the composition of the gas leaving the reaction chamber. Thus, the entire gas flow through the reaction chamber, and consequently almost all reaction products, enter this QMS. Only reaction products which might back diffuse from the reaction chamber into the mixing channel can elude the QMS.

The QMS is a vacuum system from which gas can only be pumped at a limited pumping speed. For this reason, the connection between the reaction chamber and O2 includes an on-chip flow-limiting capillary with a low flow conductance. The capillary has a width of 5 μm, a depth of 3 μm, and a length of 1500 μm. To facilitate optimal detection, these dimensions of the capillary have been chosen to obtain a gas flow through the reaction chamber of around 3×10^{14} molecules s^{-1} and a resulting QMS pressure of around 10^{-7} mbar under typical experimental conditions.

In the experimental setup, the absolute pressure at O1 can be varied in the range of 0.1–5.0 bar. The absolute pressure at O2 is at vacuum level since this outlet is connected to the QMS. It follows that there is a pressure difference of the order of 1 bar across the system. Since the flow conductance of the capillary is much lower than the conductance of any other part of the channel system, almost the entire pressure drop occurs across the capillary. Consequently, the pressure in the reaction chamber is expected to be very close to the controlled pressure at O1.

The gas flow through the reaction chamber is only around 0.01% of the flow through the mixing channel because the flow resistance of the capillary is much higher than that of the mixing channel. This difference in magnitudes of the gas flows is desirable for the following reasons. Since the gas flow through the reaction chamber constitutes the entire flow entering the QMS, this flow determines the pressure in the QMS. Only when the reaction chamber gas flow has an approximate magnitude of 10^{14} molecules s^{-1} will the QMS pressure be compatible with mass spectrometer operation. Concerning the mixing channel, such a low gas flow would be difficult to control with off-the-shelf mass flow controllers (MFCs) and highly impractical when changing the composition of the gas mixture introduced through the inlets. The volume of the exterior gas supply system connected to I1 and I2 in the experimental setup is much larger than the volume of the microchannel system itself. When changing the composition of the gas entering the chip, one, therefore, has to wait for the old gas to be fully washed away from the exterior tubing by the new gas. Until then, the composition of the gas entering the chip does not resemble the one specified by the user. Thus, a relatively high mixing channel gas flow is required to ensure a short gas residence time in the exterior tubing and a practical time-scale for changes of the gas mixtures. For these reasons, O1 has been included in the chip to generate a bypass gas flow on the order of 10^{18} molecules s^{-1}. A gas flow of this magnitude can readily be controlled with off-the-shelf MFCs.

In summary, reactant gases are introduced into the reactor through the two inlets. The reactant gas mixture flows through the mixing channel to O1, where it is vented to the atmosphere. However, around 0.01% of the mixing channel gas flow proceeds to the reaction chamber, where the reactants can react and form products under influence of the catalyst. The resulting gas mixture flows from the reaction chamber through the capillary and enters the QMS, where the gas composition is analyzed.

The large area of the reaction chamber increases the amount of catalyst which can fit at the floor of the reaction chamber for a given density. This is favorable for the purpose of obtaining a reasonably high reaction rate when the turnover frequency is low or when a low catalyst density is required to avoid sintering. The circular shape is an advantage since it makes confinement of the catalyst deposition to the reaction chamber easier than it would be, if for instance a long, narrow meander geometry of the same large area were used. When depositing metal clusters from a magnetron sputtering cluster source, the large, circular shape makes it fairly easy to align a shadow mask. When depositing a catalyst manually with a pipette, the high area and circular shape also ease the process. In addition, with a circular design liquid catalyst suspensions deposited in the reactor form a relatively uniform loading. Finally, the circular shape allows easy use of the "locally cooled anodic bonding" method which has been developed for low-temperature sealing of the microreactor.[22] This bonding method is very useful for catalysts, such as gold clusters, which are likely to sinter at elevated temperatures.

After deposition of catalyst in the catalyst bed, the reactor is sealed with a Pyrex lid, using anodic bonding.[23] During the bonding process, the Pyrex-lid and the floor of the reaction chamber will be attracted toward each other by a strong electrostatic force. Because of the low depth-to-diameter ratio of the reaction chamber, the attractive force might cause the Pyrex-lid to get into intimate contact with the floor of the reaction chamber during the anodic bonding. If this happens, attractive surface forces will quickly cause the entire reaction chamber to collapse, permanently bonding the lid to the re-

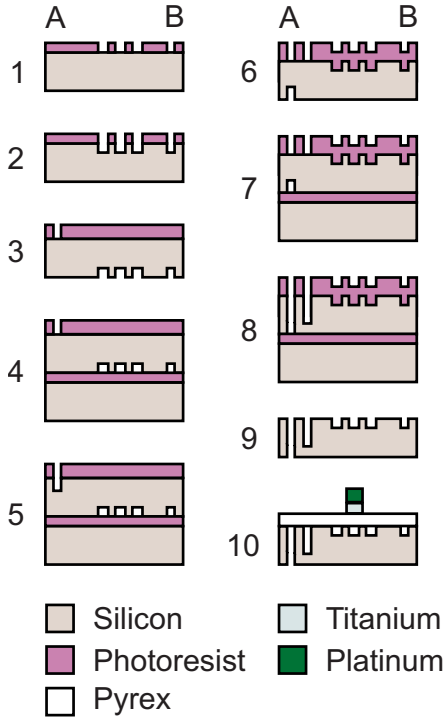

FIG. 2. (Color online) Fabrication sequence for the microreactor. (1) Reaction chamber, shallow channels, and capillary are defined in photo resist; (2) etching of the reaction chamber, shallow channels, and capillary; (3) inlet and outlet holes are defined in photoresist from back; (4) handle wafer mounting; (5) etching of inlet and outlet holes; (6) inlet and outlet holes and mixing channel are defined from front side; (7) handle wafer mounting; (8) etching of inlet and outlet holes and mixing channel; (9) removal of remaining photoresist and handle wafer; and (10) reactor sealed with Pyrex lid with integrated temperature detector using anodic bonding.

action chamber floor.[24–26] To avoid such a collapse, the reaction chamber contains 200 μm diameter silicon pillars which are spaced 1 mm apart. These pillars prevent the lid from getting into contact with the reaction chamber floor during the bonding process.

B. Microreactor fabrication

The microreactor is fabricated using micromanufacturing batch techniques. With these processes, large numbers of reactors can be produced in a short time and at relatively low cost. The silicon chips are fabricated using ultraviolet (UV) lithography, RIE, and DRIE. These are all standard microfabrication processes. The fabrication sequence for the silicon chips is shown in Fig. 2. The starting point is a 350 μm thick silicon wafer. First, what will later become the substrate front side is covered with a 1.5 μm thick layer of AZ5214 photoresist (a photosensitive, etch resistant polymer). A pattern containing the reaction chamber and the capillary is then defined in the polymer using UV lithography, and the wafer is etched to a depth of around 3.0 μm through a RIE process. This pattern also includes the two microchannels leading from the mixing channel to the reaction chamber and from the reaction chamber to the capillary, respectively. After etching the low flow part of the channel system, the polymer mask is removed in acetone. A 9.5 μm thick layer of AZ4562 photoresist is then applied to the back of the wafer, and a pattern containing the in- and outlet holes is defined using UV lithography. Now, the front of the wafer is bonded to a handle wafer using photoresist as an adhesive. This is done to protect this side of the wafer, which might otherwise become damaged along the edge during the subsequent DRIE process. The pattern is then etched using DRIE to a depth of around 100 μm, followed by removal of the remaining photoresist and the handle wafer in acetone. The front of the wafer is now covered with a 9.5 μm thick layer of AZ4562 photoresist, and a pattern containing the mixing channel is defined using UV lithography. Again, before the subsequent DRIE process, the side of the wafer not covered by photoresist is bonded to a handle wafer. At this point in the process flow, the handle wafer is required since the in- and outlet holes will now be etched all the way through the wafer. In the DRIE tool helium gas is used to cool the back of the wafer during etching. If no handle wafer were used, the helium gas would leak into the plasma chamber through the in- and outlet holes. The mixing channel pattern is now etched using DRIE until it reaches the in- and outlet holes at a depth of approximately 250 μm. Afterwards, the remaining photoresist and the handle wafer are removed in acetone. As a final fabrication step, the chip is thermally oxidized with an oxide thickness of 50 nm. The wafer is sawn into small chips, each containing one microreactor.

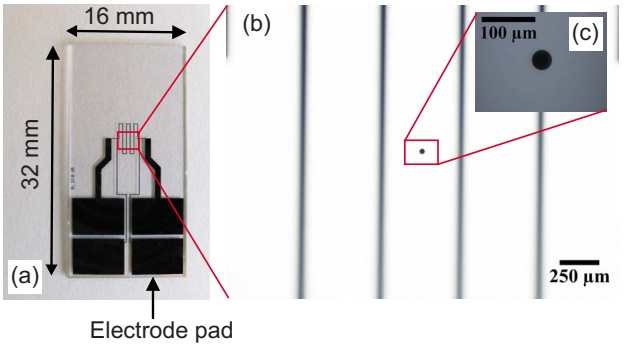

FIG. 3. (Color online) (a) Photograph of the Pyrex lid with integrated platinum thin film RTD. The temperature is determined with a four-point-probe measurement of the resistance of the meander path in the center of the lid. (b) Magnification of the center of the meander path. The platinum catalyst circle is visible in the center. (c) Magnification of the catalyst circle. This particular circle has a diameter of 36 μm.

To prepare the microreactor for a catalyst test experiment, a catalyst material can be deposited in the reaction chamber using one of the deposition methods described earlier. The microchannel system is subsequently sealed with a Pyrex lid using anodic bonding. This concludes the preparation procedure, and catalyst testing can be initiated. The total preparation time before measurements can be commenced depends on the catalyst deposition method, but is usually around one hour. In the experimental results presented in this article, the catalyst is incorporated on the Pyrex lid surface as a thin film. Thus, no additional catalyst is deposited in the reaction chamber prior to bonding in these specific experiments.

The side of the Pyrex-lid facing the silicon chip includes a circular platinum thin film, as seen in Fig. 3. This platinum circle acts as a catalyst in the test reaction. A number of

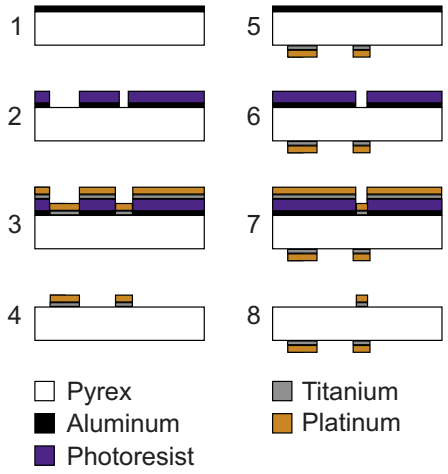

FIG. 4. (Color online) Fabrication sequence for the Pyrex lid. (1) Aluminum thin film deposition on front side; (2) RTD is defined in photoresist and aluminum; (3) titanium and platinum thin film deposition; (4) lift-off of titanium and platinum and removal of aluminum; (5) aluminum thin film deposition on back; (6) catalyst circle is defined in photoresist and aluminum; (7) titanium and platinum thin film deposition; and (8) lift-off of titanium and platinum and removal of aluminum.

different lids with platinum circle areas ranging from 15 μm^2 to 5000 μm^2 is fabricated. By performing measurements with different platinum circle areas, it is possible to investigate the relation between the catalyst area and the lowest temperature at which catalytic activity can be detected. The other side of the lid is equipped with an integrated four-point probe resistive temperature detector (RTD) consisting of a structured platinum thin film. The positions of the RTD and the catalyst circle both match with the center of the reaction chamber. The Pyrex lid has dimensions of 16×32 $mm^2 \times 500$ μm.

The lid is fabricated using UV lithography, PVD, and lift-off processes in acetone. These are all standard microfabrication processes. The fabrication sequence for the lid is shown in Fig. 4. The starting point is a 500 μm thick Pyrex wafer. First, what will later become the RTD side of the lid is covered with a 10 nm thick aluminum thin film using e-beam PVD. The aluminum layer acts to promote adhesion between photoresist and the wafer. In addition, the aluminum layer reflects UV light and thus prevents reflections from the chuck in the exposure tool during the lithography process. This is important since the Pyrex wafer is transparent to UV light. A 1.5 μm thick layer of AZ5214 photoresist is now spun on top of the aluminum, and a pattern containing the RTDs is subsequently defined in the polymer using UV lithography. As a part of the lithography-process the photoresist is developed in an aqueous NaOH-solution. During this development process, the aluminum below the exposed parts of the photoresist is also etched away. A 10 nm thick titanium thin film is then deposited on the RTD side using e-beam PVD. This titanium layer serves as an adhesion layer between the Pyrex substrate and the platinum thin film which is deposited next. Now, a 100 nm thick platinum thin film is deposited using e-beam PVD. The polymer mask and the metal on top of it are subsequently lifted off in acetone using ultrasound. This is followed by removal of the remaining aluminum in an aqueous solution of NaOH. The RTD has now been formed on top of the Pyrex lid. Afterwards, the catalyst circle is formed on the opposite side of the lid. This is done by processing the back of the wafer in exactly the same way as the front side, while using a different mask when exposing the polymer to UV light. Hence, the catalyst circle consists of a 100 nm thick platinum thin film in addition to a 10 nm thick titanium thin film in between the platinum and the Pyrex substrate. Finally, the Pyrex wafer is sawn into small chips, each containing one lid. Before the measurements, the RTDs are annealed at 400 °C.

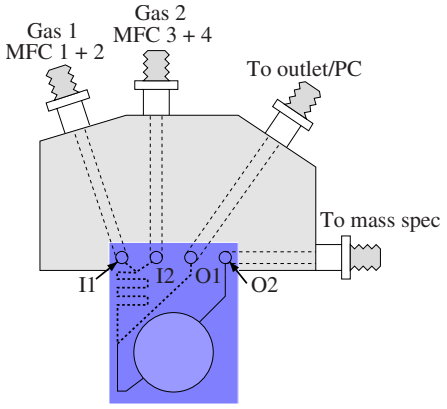

FIG. 5. (Color online) Sketch of the stainless steel manifold fixture for the microreactor. Gas lines machined in the interior of the fixture connect the inlets and outlets of the microreactor to MFCs, a PC, and a QMS.

C. Experimental setup

The gas handling system is made from 1/4 in. stainless steel tubing with welded VCR® (Swagelok) fittings as connections. The microreactor is mounted in a stainless steel manifold fixture with welded VCR® fittings, and the gas lines are connected to the microreactor through this fixture. A sketch of the arrangement is shown in Fig. 5. The gas lines are machined in the interior of the fixture, and tight connections between the steel block and the microreactor are ensured by using Kalrez perfluoroelastomer O-rings.

Since the O-rings are made from an elastomer, a small amount of gas diffusion from the surrounding air into the system is unavoidable, particularly at elevated temperatures. This gives rise to unwanted background signals of O_2 and N_2, complicating analysis of the reaction products and source gas species. To mitigate this problem, a continuous flow of argon is introduced in the volume surrounding the O-rings. Thus, any unwanted background due to diffusion through O-rings will be in the form of argon.

The reactor is heated from the silicon side using an external resistive heating element covering the outline of the reaction chamber. The temperature is measured with four point measurements of the resistance of the integrated RTD. The gas flow to the two inlets is controlled by four MFCs allowing mixing of up to four different gases. Outlet 1 is connected to a pump via a pressure controller (PC). This makes experiments at absolute pressures from 0.1 to 5.0 bar possible. The gas flows, the PC, and the temperature are all controlled with a LabVIEW program. The temperature is

controlled using a PID algorithm, allowing temperature changes of up to 1 K/s and constant temperatures within 0.1 K. Time resolved gas detection is performed with a QMS (Balzers QMA 125) equipped with a secondary electron multiplier.

III. RESULTS AND DISCUSSION

A. Gas flow

The pressure difference between the reaction chamber and O2 gives rise to a gas flow through the capillary, and the magnitude of the gas flow depends on the exact value of the reaction chamber pressure as well as the temperature. The absolute gas flow through the capillary is an essential design parameter for the following reasons. The reaction chamber and the capillary are connected in series, so the flows through them are the same. Consequently, the residence time of the gas in the reaction chamber can be derived from the capillary flow. Furthermore, knowledge of the gas flow is important for interpretation of experimental results, for instance for determining absolute reaction rates. Finally, when designing the microreactor, the capillary dimensions must be chosen carefully to ensure that the flow to the QMS facilitates optimal gas composition analysis. Gas flows through narrow capillaries with vacuum pressure at one end are nontrivial since the small cross sectional dimensions might be comparable to the mean free path of the gas, resulting in a nonviscous flow regime. It follows that it is of interest to measure the capillary gas flow using an absolute method.

To characterize the relation between the pressure in the reaction chamber and the gas flow through the capillary, a microreactor is mounted in the manifold fixture to allow flow from a fixed volume to the QMS. This is done by sealing up the gas lines in the interior of the fixture from the external pump system. Thus, a fixed volume constituted by the microchannel system in the reactor and the gas lines in the interior of the fixture is hermetically sealed. The only path by which gas can leave the volume is by entering the QMS through the on-chip capillary. In this experiment, a Baratron (MKS Inc. type 211, 0–1 bar range), which measures the pressure inside the fixed volume, is installed in the fixture. At the onset of the experiment, the fixed volume contains atmospheric air at atmospheric pressure, and the QMS is at vacuum pressure. The fixed volume is 11.2 ml, and the experiment is carried out at room temperature. The pressure is plotted as a function of time in Fig. 6(a). As gas flows through the capillary, the pressure in the fixed volume decreases, and the flow is obtained from

$$\dot{N}(t) = \frac{V}{k_B T}\frac{dp_v(t)}{dt}, \tag{1}$$

where $\dot{N}(t)$ is the net number of gas molecules crossing a cross section of the capillary per unit time, $p_v(t)$ is the pressure in the fixed volume, V is the volume, k_B is the Boltzmann constant, T is the temperature of the fixed volume, and t is time. In the experiment the microreactor has a capillary depth of 3.0 μm. In Fig. 6(b), $\dot{N}$ is plotted as a function of the pressure in the fixed volume.

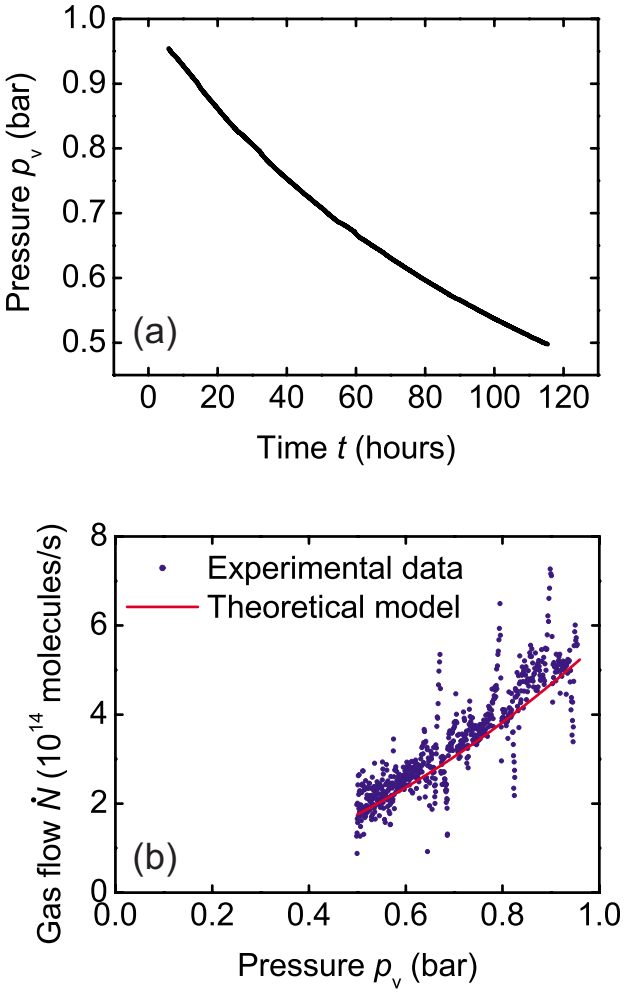

FIG. 6. (Color online) (a) Measured pressure p_v in the fixed volume as a function of time. (b) Experimentally measured flow as a function of the reaction chamber pressure p_v (blue circles). The red curve is the theoretically predicted flow as a function of p_v.

The gas flow through the capillary is now described with a theoretical model for comparison with the experimental results. The width of the capillary is very small compared to the widths of the channel leading from the mixing channel to the reaction chamber and the channel leading from the reaction chamber to the capillary. Consequently, the flow resistances of the latter two channels as well as that of the reaction chamber can be safely neglected when predicting the flow entering the QMS. Thus, in this discussion only the flow resistance of the capillary is considered.

Gas flow in a tube of characteristic cross sectional width d can be characterized by the Knudsen number λ/d, where λ is the mean free path of molecules in the gas. If $\lambda/d < 0.0091$, the flow is viscous, if $0.0091 < \lambda/d < 1$, the flow is intermediate, and if $\lambda/d > 1$, the flow is molecular.[27,28] The capillary has a rectangular cross section with dimensions 5×3 μm^2. However, when attempting to predict the relation between the capillary gas flow and the pressure in the reaction chamber, it is convenient to treat the capillary as having a circular cross section. The advantage of this approximation is that for a circular cross section analytic expressions for the flow exist for all three flow regimes. In

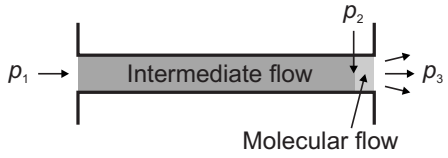

FIG. 7. Sketch of the capillary showing the reaction chamber side (left) and the QMS side (right). The reaction chamber pressure is p_1, and the QMS pressure is p_3. The regions with intermediate and molecular flow are indicated. At the position where the pressure is p_2, the gas flow changes from intermediate to molecular.

this discussion, a circular cross section of diameter $d=4.4\ \mu$m and thus of the same area as the actual rectangular cross section will be assumed.

For air at room temperature, the mean free path is given by[27]

$$\lambda = \frac{6.7 \times 10^{-3}\ \text{Pa m}}{p}, \tag{2}$$

where p is the pressure. For a capillary diameter of 4.4 μm, this means that the flow is intermediate at atmospheric pressure, and that the transition from intermediate to molecular flow occurs at a pressure of around 1.5×10^3 Pa. In Fig. 7, the capillary is shown schematically with the two flow regimes. The inlet pressure is p_1, and at the pressure p_2 the flow changes from intermediate to molecular. The pressure in the QMS is denoted p_3.

In the intermediate flow regime, the gas flow through a tube of length ℓ with circular cross section is[27]

$$\dot{N} = c\frac{p_1 - p_2}{k_B T}, \tag{3}$$

with

$$c = \frac{\pi}{128}\frac{\bar{p}d^4}{\eta\ell} + \frac{1}{3}\sqrt{\frac{\pi}{2}}\frac{d^3}{\ell v}\frac{1+\frac{dv\bar{p}}{\eta}}{1+1.24\frac{dv\bar{p}}{\eta}}, \tag{4}$$

where η is the viscosity of the gas, $\bar{p}=(p_1+p_2)/2$, $v=\sqrt{m/(k_B T)}$, and m is the mass of a single gas molecule. In the molecular flow regime[29]

$$\dot{N} = \frac{1}{3}\sqrt{\frac{\pi}{2}}\frac{d^3}{\ell v}\frac{p_2 - p_3}{k_B T}. \tag{5}$$

Using Eq. (2), the expressions Eqs. (3) and (5) can be combined to obtain an analytical expression for the flow that includes both the intermediate and the molecular flow regimes. In addition, an analytical expression for the fraction of the capillary length where the flow is intermediate can be obtained. For atmospheric air at $T=295$ K and at $p_v>0.5$ bar, the flow is intermediate in more than 98% of the length of the capillary, according to this calculation. In Fig. 6(b), the theoretically predicted gas flow as a function of the pressure in the fixed volume is plotted with $T=295$ K, $\eta=17.8\times10^{-6}$ Pa s, and $m=4.81\times10^{-26}$ kg (the average molecular mass in the air). Both the intermediate and the molecular flow regimes are taken into account when calculating this gas flow. A good agreement with the experimental data is observed. It is emphasized that the expected gas flow plotted in Fig. 6(b) is generated from a purely theoretical model, and that the experimental data are not considered when making this prediction. Thus, the theoretical model presented here is not a fit to experimental data but rather a prediction based entirely on the capillary dimensions, the temperature, and the properties of the gas.

Based on these results, the capillary gas flow at typical experimental conditions can be inferred. It appears from Fig. 6(b) that, at approximately atmospheric pressure in the reaction chamber, the capillary gas flow is around 6×10^{14} molecules s^{-1} at room temperature. At the same pressure and a typical reactor temperature of 250 °C, the theoretical model predicts a flow of around 3×10^{14} molecules s^{-1}, corresponding to a gas residence time in the reaction chamber of around 11 s.

During operation, gas is pumped out of the QMS by a turbo pump. In steady state, the amount of gas flowing through the capillary equals the amount pumped by the turbo pump. The pressure p_{ms} in the QMS is then given by

$$p_{\text{ms}} = \frac{k_B T_{\text{ms}}}{S}\dot{N}, \tag{6}$$

where T_{ms} is the temperature of the gas in the QMS, $\dot{N}$ is the number of gas molecules pumped by the turbo pump per unit time, and S is the gas volume pumped by the turbo pump per unit time. S is referred to as the pumping speed. It is clear from Eq. (6) that the gas flow through the capillary determines the pressure in the QMS. Since the gas flow in turn is determined by the capillary dimensions, these dimensions must be chosen to facilitate a suitable QMS pressure. During the experiment, p_{ms} is continuously measured with an ion gauge and is in the range $2-10\times10^{-7}$ mbar. These pressures are well-suited for QMS analysis suggesting that the capillary dimensions are appropriate. Using Eq. (6), the effective pumping speed is determined to be approximately 38 l/s. This is reasonable, since the geometric pump aperture is about 9 cm^2 giving a maximum theoretical pumping speed of ~106 l/s.

Although the experimental data in Fig. 6(b) are in good agreement with the theoretical prediction, pronounced deviations appear at $p_v=67$ kPa, $p_v=80$ kPa, and $p_v=90$ kPa. These deviations derive from the numerical differentiation of the pressure with respect to time in Eq. (1). The deviations are caused by distinct periods of time in the originally measured values of $p_v(t)$ characterized by a relatively abrupt increase of about 200 Pa in p_v followed by a corresponding decrease back to the original level 5–8 h later. These "bumps" in the measured values of $p_v(t)$ are caused by unstable performance of the Baratron. In spite of this effect, the quantitative agreement between experimental data and the theoretical prediction clearly suggests that the gas flow can be understood in terms of the theoretical model outlined above.

It is noted that other desired values of the capillary flow resistance can easily be obtained by fabricating microreactors with other capillary dimensions. This could be favorable for some experiments. For a constant inlet pressure, an in-

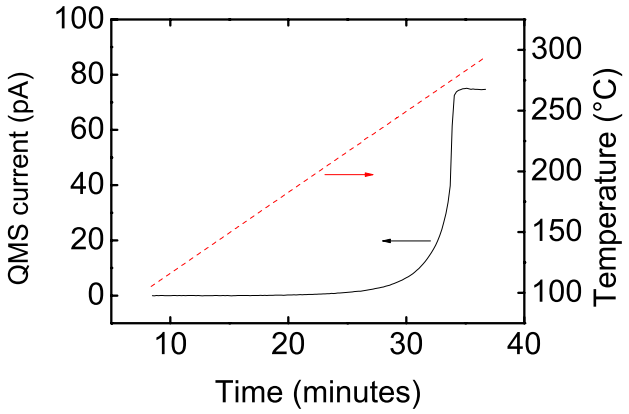

FIG. 8. (Color online) Experimental data from oxidation of carbon monoxide in the microreactor using a platinum thin film catalyst. The measured temperature (red, dashed curve, right ordinate axis) and the CO_2 signal in the QMS (black, solid curve, left ordinate axis) are plotted as a function of time. The catalyst area is 515 μm^2, and the CO_2 content is measured using the mass 44 signal in the QMS.

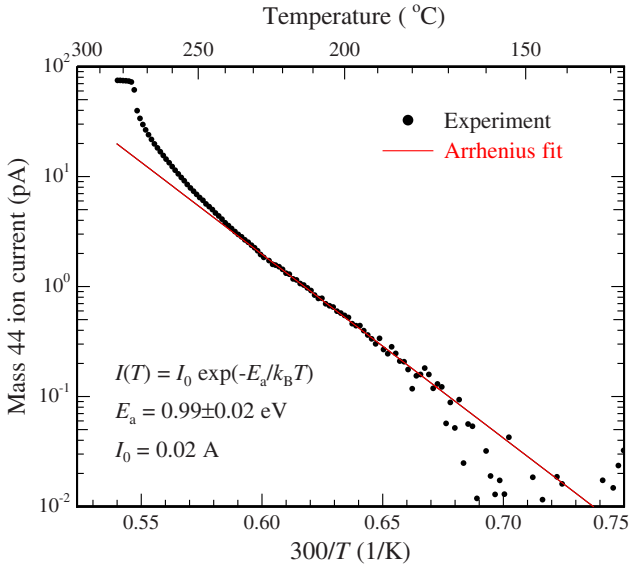

FIG. 9. (Color online) Arrhenius plot of the mass 44 (CO_2) signal plotted in Fig. 8 (black circles). The catalyst area for this experiment is 515 μm^2 platinum. A linear fit of the part of the experimental data, where the reaction exhibits Arrhenius behavior, is also shown (red line). The slope of the fit corresponds to an apparent activation energy of 0.99 eV.

crease of the capillary width would for example result in a shorter reaction chamber residence time.

B. Oxidation of carbon monoxide

To demonstrate the operation of the microreactor, CO oxidation on platinum thin film circles is used as a test reaction. In particular, the experiments are performed to test the ability to measure catalytic activity of catalysts with low surface areas. Since the main purpose of the reactor design is to improve sensitivity to enable studies on low density mass selected clusters, this is essential information on reactor performance. A gas mixture consisting of CO and O_2 is used, and the platinum circles have different areas ranging from 15 to 5000 μm^2. The reaction is run at a pressure of 1.00 bar in a surplus of oxygen, with an O_2:CO ratio of 20:1 and with a total flow rate of 8.4 Nml min^{-1} through the mixing channel. After mounting in the manifold fixture, the reactor is heated to 400 °C in the reaction gas, until any organic contaminants have been burned away, and the gas system has stabilized. The experiments consist of repeatedly ramping the temperature from 80 to 350 °C at a rate of 400 K/h, activating the CO oxidation

$$2CO(g) + O_2(g) \rightarrow 2CO_2(g). \tag{7}$$

Figure 8 shows the temperature and the CO_2 signal in the QMS, both as a function of time, during a single temperature ramp. This experiment is carried out with a catalyst area of 515 μm^2, and the CO_2 content in the QMS is measured using the mass 44 signal. As the temperature is increased, the CO_2 signal rises exponentially until a "light off" phenomenon is seen, and full conversion of CO to CO_2 takes place. In Fig. 8, the background of CO_2 from reactions on the filament in the QMS has been subtracted. The CO and O_2 signals are measured simultaneously with the CO_2 signals at mass 28 and 32, respectively. Both signals drop as the CO_2 content increases in accordance with the stoichiometry of the reaction.

At low conversion, the CO_2 reaction rate $\dot{N}_{CO_2}$ (the number of CO_2 molecules produced in the reaction chamber per unit time) is[1]

$$\dot{N}_{CO_2} \simeq A r_0(p_{CO}, p_{O_2}, p_{CO_2}) \exp\left(\frac{-E_a}{k_B T}\right), \tag{8}$$

where A is the area of the platinum circle, E_a is the apparent activation energy, and p_{CO}, p_{O_2}, and p_{CO_2} are the partial pressures in the reaction chamber of CO, O_2, and CO_2, respectively. $r_0(p_{CO}, p_{O_2}, p_{CO_2})$ is a parameter which depends on the partial pressures and the catalyst. The data from Fig. 8 are shown as an Arrhenius plot in Fig. 9. Here, it can be seen that at low temperature and low conversion the rate follows an Arrhenius behavior as expected, with an apparent activation energy E_a of 0.99 eV. For all the samples, the reactivity exhibited Arrhenius behavior with apparent activation energies in the range 0.91–1.40 eV with the highest values found for the measurements with smaller catalyst areas. Contreras *et al.*[30] performed experiments with CO oxidation on a 15 nm thick platinum thin film deposited using PVD on a silicon(100) wafer with native oxide. At temperatures below "light off," these authors measured an apparent activation energy of 1.17 eV, within range of the values found in this work.

The microreactor and the corresponding experimental arrangement are designed to facilitate high sensitivity characterization of catalytic reactions. The sensitivity of the setup is now evaluated by considering the smallest catalyst area for which catalytic activity can be detected. The criterion for detection of catalytic activity is that the product QMS current I_p must be distinguishable from the background in the QMS. Thus, I_p must be higher than some threshold value I_t, which is determined by the QMS background. For the CO oxidation measurements described here, I_t is defined to be 1.0 pA,

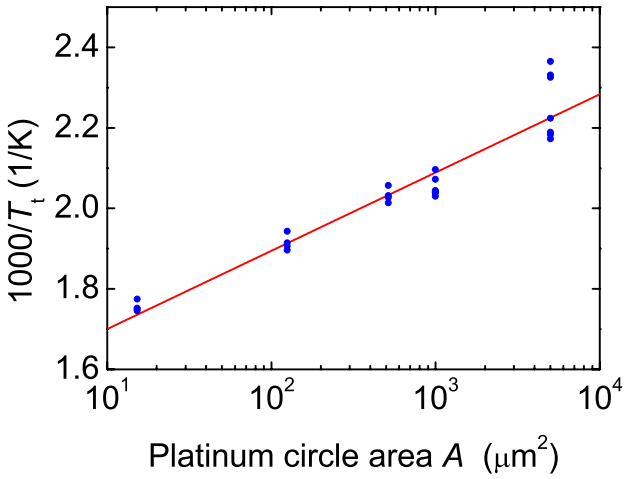

FIG. 10. (Color online) The inverse of the lowest temperature at which CO oxidation can be detected plotted as a function of catalyst area. Experimental data from all measured samples are shown (blue circles). The abscissa axis has logarithmic scale. The linear fit (red line) yields an apparent activation energy of 1.02 eV.

since this is significantly higher than the background. The product current increases linearly with the reaction rate $\dot{N}_p$ in the reaction chamber. It follows that the criterion for detection is satisfied when

$$\dot{N}_p > \dot{N}_t, \tag{9}$$

where $\dot{N}_t$ is the reaction rate which causes a product current I_t.

From Eqs. (8) and (9), it follows that for a given area the temperature must exceed a certain threshold temperature T_t before product formation can be detected. T_t is the temperature which causes a reaction rate $\dot{N}_t$. Only if the temperature is higher than T_t, will the catalytic activity be high enough to cause a QMS product signal distinguishable from the background. In view of Eqs. (8) and (9), the threshold temperature can be predicted.

$$\dot{N}_t = Ar_0 \exp\left(\frac{-E_a}{k_B T_t}\right) \Rightarrow \frac{1}{T_t} = \frac{k_B}{E_a}\left(\ln A - \ln\frac{\dot{N}_t}{r_0}\right). \tag{10}$$

Assuming that $\dot{N}_t/r_0$ may be considered constant, only A and T_t vary in the CO oxidation experiments. Thus, the inverse threshold temperature plotted against the logarithm of the area should yield a straight line with a slope of k_B/E_a. Figure 10 shows the experimental data from CO oxidation in the microreactors. The inverse of the lowest temperature at which CO_2 formation can be detected is plotted against the platinum circle area (logarithmic scale). In the data evaluation, the threshold current I_t is defined to be 1.0 pA, which is significantly above the background (see Fig. 9). From the slope of the best linear fit to the data, an apparent activation energy of 1.02 eV is found. This is within range of the values found from the individual Arrhenius plots.

It appears from Fig. 10 that even for the smallest catalyst area of 15 μm^2, conversion into CO_2 can be detected at a temperature of ~300 °C. This temperature can easily be reached with the experimental setup. An area of 15 μm^2 is considerably lower than catalyst areas for other high-sensitivity chemical reactors reported in literature.[9,10] The experimental data thus demonstrate the high sensitivity of the microreactor and the capability to measure reactivity of small amounts of catalyst.

IV. CONCLUSIONS

The microfabricated chemical reactor presented here facilitates highly sensitive catalyst testing. An integrated capillary limits the gas flow through the catalyst bed to around 3×10^{14} molecules s^{-1} at typical experimental conditions, making it possible to direct the entire reaction zone gas flow to enter a QMS. This prevents unnecessary dilution of the reaction products and causes almost all the products to enter the gas analysis tool, thus ensuring a high sensitivity. The microreactor can be employed as a platform for testing of a wide variety of different catalysts, including industrial catalysts. However, the primary aim of the device is to allow measurements of catalytic activity and surface kinetics of model catalysts, which can only be obtained in small quantities, thus necessitating high sensitivity to low surface areas. In particular, the reactor is well-suited for characterization of mass selected metal clusters from a sputtering cluster source.

The relationship between the reaction zone gas flow and the pressure in the reaction chamber has been investigated with a theoretical model, which predicts the gas flow in the capillary to be in the intermediate flow regime. The theoretical model is in good agreement with experimental results. CO oxidation on low-area platinum thin films was carried out in the reactor as a test reaction to demonstrate the operation of the device. The experimental data show that for this reaction and under the conditions used in these experiments, catalysts with surface areas as low as 15 μm^2 can be conveniently characterized with the microreactor. This catalyst area is considerably lower than for other high-sensitivity chemical reactors reported in literature.

ACKNOWLEDGMENTS

Center for Individual Nanoparticle Functionality (CINF) is sponsored by The Danish National Research Foundation.

[1] I. Chorkendorff and J. Niemantsverdriet, *Concepts of Modern Catalysis and Kinetics* (Wiley, New York, 2003)
[2] K. F. Jensen, Chem. Eng. Sci. **56**, 293 (2001).
[3] S. K. Ajmera, C. Delattre, M. A. Schmidt, and K. F. Jensen, Sens. Actuators B **82**, 297 (2002).
[4] G. Kolb and V. Hessel, Chem. Eng. J. **98**, 1 (2004).
[5] K. Jähnisch, V. Hessel, H. Lowe, and M. Baerns, Angew. Chem. Int. Ed. **43**, 406 (2004).
[6] L. Kiwi-Minsker and A. Renken, Catal. Today **110**, 2 (2005).
[7] K. Wong, S. Johansson, and B. Kasemo, Faraday Discuss. **105**, 237 (1996).
[8] A. S. Eppler, G. Rupprechter, L. Guczi, and G. A. Somorjai, J. Phys. Chem. B **101**, 9973 (1997).
[9] S. Johansson, E. Fridell, and B. Kasemo, J. Vac. Sci. Technol. A **18**, 1514 (2000).
[10] P. W. Jacobs, S. J. Wind, F. H. Ribeiro, and G. A. Somorjai, Surf. Sci. **372**, L249 (1997).
[11] U. Quaade, S. Jensen, and O. Hansen, Rev. Sci. Instrum. **75**, 3345 (2004).
[12] O. Younes-Metzler, J. Svagin, S. Jensen, C. H. Christensen, O. Hansen, and U. Quaade, Appl. Catal., A **284**, 5 (2005).
[13] O. Younes-Metzler, J. Johansen, S. Thorsteinsson, S. Jensen, O. Hansen, and U. Quaade, J. Catal. **241**, 74 (2006).
[14] R. Z. Sørensen, A. Klerke, U. Quaade, S. Jensen, O. Hansen, and C. H.

Christensen, Catal. Lett. **112**, 77 (2006).
[15] U. Heiz and E. L. Bullock, J. Mater. Chem. **14**, 564 (2004).
[16] K. Judai, S. Abbet, A. S. Worz, U. Heiz, and C. R. Henry, J. Am. Chem. Soc. **126**, 2732 (2004).
[17] D. W. Goodman, Nature (London) **454**, 948 (2008).
[18] S. Thybo, S. Jensen, J. Johansen, T. Johannessen, O. Hansen, and U. Quaade, J. Catal. **223**, 271 (2004).
[19] S. Johansson, E. Fridell, and B. Kasemo, J. Catal. **200**, 370 (2001).
[20] M. Roumanie, C. Delattre, F. Mittler, G. Marchand, V. Meille, C. de Bellefon, C. Pijolat, G. Tournier, and P. Pouteau, Chem. Eng. J. **135**, S317 (2008).
[21] A. M. Hynes, H. Ashraf, J. K. Bhardwaj, J. Hopkins, I. Johnston, and J. N. Shepherd, Sens. Actuators, A **74**, 13 (1999).
[22] P. C. K. Vesborg, J. L. Olsen, T. R. Henriksen, I. Chorkendorff, and O. Hansen, "Anodic bonding with cooling of heat sensitive areas," Rev. Sci. Instrum. (submitted).
[23] G. Wallis and D. I. Pomerantz, J. Appl. Phys. **40**, 3946 (1969).
[24] W. P. Shih, C. Y. Hui, and N. C. Tien, J. Appl. Phys. **95**, 2800 (2004).
[25] P. Mao and J. Y. Han, Lab Chip **5**, 837 (2005).
[26] K. M. Knowles and A. T. J. van Helvoort, Int. Mater. Rev. **51**, 273 (2006).
[27] A. Roth, *Vacuum Technology*, 3rd ed. (Elsevier, Amsterdam, 1990).
[28] U. Quaade, S. Jensen, and O. Hansen, J. Appl. Phys. **97**, 044906 (2005).
[29] J. O'Hanlon, *A User's Guide to Vacuum Technology*, 3rd ed. (Wiley, Hoboken, New Jersey, 2003).
[30] A. M. Contreras, X. M. Yan, S. Kwon, J. Bokor, and G. A. Somorjai, Catal. Lett. **111**, 5 (2006).

Paper II

Anodic bonding with cooling of heat-sensitive areas
Peter C. K. Vesborg, Jakob L. Olsen, Toke R. Henriksen, Ib Chorkendorff, and Ole Hansen
Review of Scientific Instruments **81**, 016111, (2010)

Note: Anodic bonding with cooling of heat-sensitive areas

Peter C. K. Vesborg,[a] Jakob L. Olsen, Toke R. Henriksen,[b]
Ib Chorkendorff, and Ole Hansen[b]
Department of Physics, CINF, Technical University of Denmark (DTU), Building 312, Fysikvej, DK-2800 Kgs. Lyngby, Denmark

(Received 26 August 2009; accepted 3 December 2009; published online 26 January 2010)

Anodic bonding of silicon to glass always involves heating the glass and device to high temperatures so that cations become mobile in the electric field. We present a simple way of bonding thin silicon samples to borosilicate glass by means of heating from the glass side while locally cooling heat-sensitive areas from the silicon side. Despite the high thermal conductivity of silicon, this method allows a strong anodic bond to form just millimeters away from areas essentially at room temperature. © *2010 American Institute of Physics.* [doi:10.1063/1.3277117]

The highly useful phenomenon—that silicon (with a thin oxide layer) may form an impressively strong bond to glass when the two materials are brought into intimate contact under the influence of strong electric fields and high temperature, anodic bonding (also known as "Mallory bonding," named after the company where it was invented and patented[1])—has been known and used for many years.[2]

The process is particularly useful for microelectromechanical system (MEMS) pressure sensors and other transducers and in weather sealing of solar cells because the bond hermetically seals the surfaces together.[3] In our research group we use the process for sealing μ-reactors for catalyst characterization;[4] however for this application the high temperatures needed for successful anodic bonding may cause catalysts to sinter or otherwise lose activity. An example of this is Au-based catalysts, which are notorious for deactivating since activity is dependant on very small Au particle size. This paper describes a practical way to overcome this issue by locally cooling the chip while the rest of it bonds. This method has proven practical and reliable in our implementation and could be useful for many other MEMS applications.

In brief, anodic bonding works by applying a large (~kV) negative bias on the glass with respect to the silicon while at the same time heating the stack such that cations in the glass become somewhat mobile. The electric field set up over the interface causes migration of ions (typically Na^+ for normal glass types) away from the interface, which sets up an intrinsic electrostatic attraction between the silicon and the glass. No external force is therefore required as the internal forces set up by this field are very strong (pressure in the GPa range).[3,5] True chemical bonds are formed between the Si and the glass permanently bonding the two surfaces. A schematic of the process is shown in Fig. 1. The downside of the technique is the inherent necessity of elevated temperatures to give the cations reasonable mobility in the glass.[6] In some applications a typical bonding procedure for borosilicate-type glass (e.g., Pyrex) to silicon (e.g., 30 min at 350 °C) may well exceed the thermal budget of parts of the device. In such cases the traditional remedy is to use glass types that conduct at lower temperatures. A typical strategy might be a lithium doped glass-ceramics,[7] but generally the process still does not work below perhaps 160 °C),[7,8] and differences in thermal expansion coefficients might be problematic for these glass types, while conventional borosilicate glass is well matched to Si. Another method is low-temperature soldering with, e.g., In/Sn eutectic mixtures;[9] however necessary measures to avoid oxidation of the solder make this method unsuited for general use in open air, and the minimum temperature for this method is also ~160 °C. Devices may also be sealed with adhesives, but (un)cleanliness and leakage makes this unattractive.

Conventional (hot) anodic bonding is shown in Fig. 1, while the locally cooled-bonding method we have developed may be seen in cross section in Fig. 2. There are a few key differences to note. First, since it is the glass (not the silicon) that needs to be warm we apply heat from the glass side. The heater also serves as high tension cathode. Second, the heater only touches the glass where bonding is needed and heat is acceptable. Third, we have introduced a heat sink (cold finger), which also serves as electrical connection to ground, and the heat sink only touches the silicon in the areas where low temperature (and not bonding) is needed. In our setup, the cold finger supporting the silicon and the hole in the heater are both cylindrical, giving the advantage of radial symmetry (no corners with stress concentration) when parts of the system heat and cool.

As a practical method for heating the top electrode, we use two commercial 150 W incandescent lamps with quartz envelopes (Osram) embedded in holes in the top electrode, which is made of aluminum for its high thermal conductivity. Quartz is insulating well above the relevant temperatures, so the power supply for the filaments does not need galvanic isolation and is indeed grounded in our setup. The heat sink is machined from copper and has internal channels for coolant flow. It is kept at a constant temperature (typically 6–12 °C, but this could well be lower if needed) using a commercial circulating cooling bath. Thermal contact between the silicon and the Cu pillar may be assured with conventional heat sink compounds or a thin indium foil. For our conditions (1 kV potential drop and 475 °C cathode temperature), bonding is normally complete within 20–25 min.

[a]Electronic mail: peter.vesborg@fysik.dtu.dk.
[b]Also at Dept. of Micro- and Nanotechnology, Technical University of Denmark, DTU Nanotech Building 345 East, DK-2800 Kgs. Lyngby, Denmark.

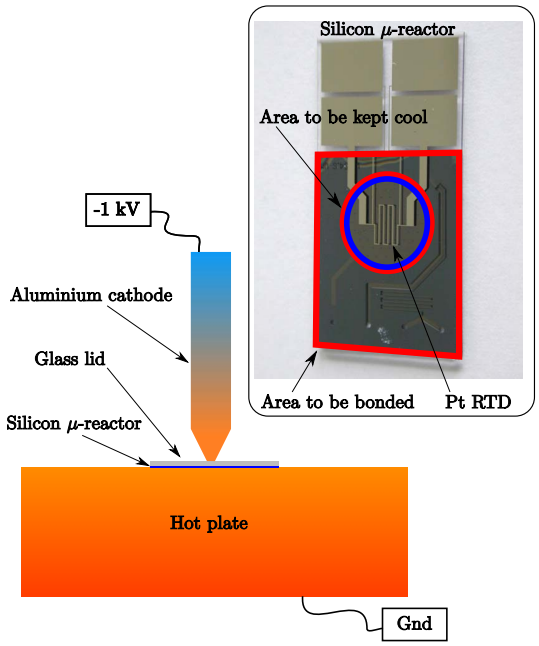

FIG. 1. (Color online) Cross section of a typical hot anodic bonding setup. The glass-silicon assembly is supported on a grounded hotplate and is contacted by a high tension cathode from above. The inset shows a photograph of our μ-reactor and highlights the areas to be bonded as well as the central reactor area, which is to be kept cold during bonding (inner blue circle). In the center of the circle (and reactor), the meander platinum RTD structure on the inside of the glass lid may be seen.

In order to find out what the temperature inside the reactor is during bonding, we have performed a direct measurement inside the reactor using resistive temperature detection (RTD) and also carried out a finite-element-type

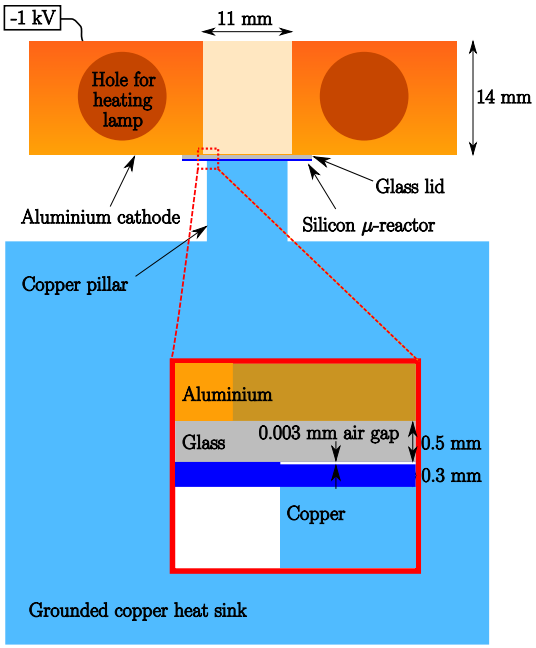

FIG. 2. (Color online) Cross-sectional view showing the locally cooled-bonding setup. The grounded Cu pillar is kept cold and acts as a heat sink during bonding, while the cathode is kept at high temperature so that it simultaneously supplies the high voltage and heats the glass. Over the Cu cold finger a cylindrical hole is drilled in the cathode, so only a minimum of heat is transferred to the central (reactor) part of the chip.

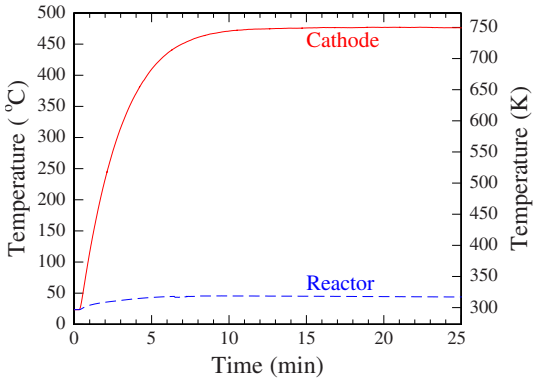

FIG. 3. (Color online) Thermocouple measurement of the aluminum cathode temperature and RTD measurement of the reactor chamber temperature.

calculation using the COMSOL MULTIPHYSICS 3.5 software package. For the four-point RTD measurement, we have used our standard RTD μ-reactor lids, which incorporate a 100 nm thick platinum four terminal resistor structure and contact pads for making the four connections, as may be seen in Fig. 1 and detailed in Ref. 4. For the purpose of measuring the temperature inside the μ-reactor during bonding, we turned the lid "upside down" so that the Pt RTD was inside the μ-reactor. As a result, the measured RTD temperature corresponds to the temperature inside the reactor. The temperature of the aluminum top cathode was also recorded using a K-type thermocouple. The measurements are plotted in Fig. 3. It is seen that the cathode stabilizes at ~475 °C, while the RTD temperature inside the reactor only reaches 45 °C.

In the finite element analysis (FEA), the real bonding arrangement was approximated with an axially symmetric geometry similar to the actual setup.The steady state temperature distribution was computed. The geometry of the FEA and the predicted temperature distribution are shown in Fig. 4. In the bonding setup a thermal contact resistance is expected between the aluminum and Pyrex. This was represented in the simulations by a narrow subdomain along the aluminum-Pyrex interface, giving rise to a thermal contact resistance of 5×10^{-5} m^2 K W^{-1}. In the FEA a constant tem-

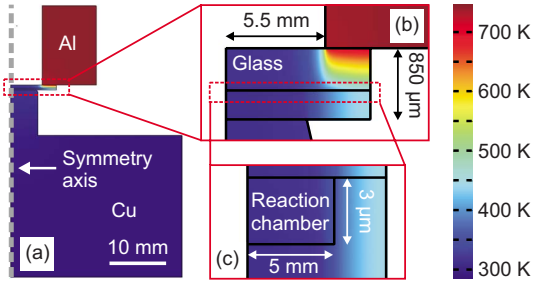

FIG. 4. (Color online) Geometry and color plot of the calculated steady state temperature distribution from the FEA. The geometry is an axially symmetric approximation of the real cooled-bonding setup. (a) The entire geometry with equal scale on both coordinate axes. The vertical dashed gray line signifies the symmetry axis. The silicon and the glass chip are stacked between the aluminum cathode and the copper heat sink. (b) Magnification of the silicon and glass chip. A high temperature gradient is observed in the part of the Pyrex lid outside the reaction chamber. (c) Magnification of the reaction chamber. The temperature in the chamber is seen to be close to room temperature as a result of the cooled-bonding fixture. Note that in (b) and (c) the scaling of the x-axis and the y-axis is different.

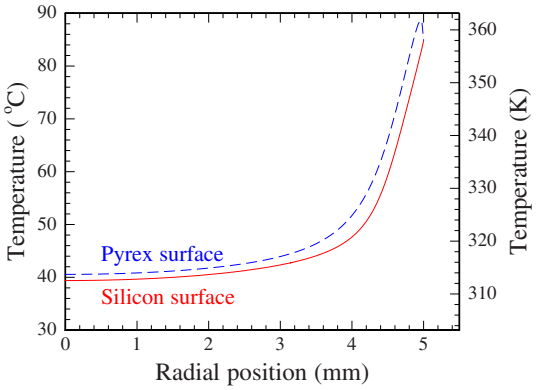

FIG. 5. (Color online) Steady state temperature distribution in the reaction chamber as computed in the FEA. The temperature in the chamber as a function of radial position is shown. The radial position is the distance from the center axis of the chamber (the symmetry axis). In the plot, the temperature in the top of the chamber adjacent to the Pyrex is shown (blue dashed curve) as well as the temperature in the bottom of the chamber adjacent to the silicon (red full curve).

perature of 475 °C was applied to the right boundary of the aluminum block. The bottom of the copper block was set to a constant temperature of 12.5 °C, and the reaction chamber was treated as containing atmospheric air. The FEA gives detailed information about the thermal gradients from which, e.g., heat fluxes and thermal expansion can be extracted. Figure 5 shows the temperature in the reaction chamber as a function of radial position according to the FEA. It is seen that the predicted temperature is below 90 °C everywhere and below 50 °C within the central 8 mm diameter circle in the chamber. In the center of the chamber the FEA predicts a temperature of around 40 °C, which is in good agreement with the experimental result 45 °C (Fig. 3).

For evaluation of the scalability of the method, it is useful to consider a design where the radial distance between heater and cold finger edges is sufficient to ensure that a region (outside the cooled air-gap region) of purely radial heat flow exists. In the present system such a region would be the cylindrical cross section with a radius of ~5.2 mm (to good approximation). In that region the ratio of heat flows in glass $P_{G,r}$ and silicon $P_{Si,r}$ is $P_{G,r}/P_{Si,r}=(\varkappa_G h_G)/(\varkappa_{Si} h_{Si})$, while the total heat flow is $P_{tot}=P_{G,r}+P_{Si,r}$; here and below $\varkappa_i$ and h_i are the thermal conductivities and material thicknesses, respectively. Then, by continuity, in the reactor region the heat flow in the glass will be directed through the air film in the reactor and cause a (mean) temperature difference $\Delta T=P_{G,r}h_{air}/(\varkappa_{air}\pi a^2)$ between top and bottom of the reactor; a is the radius of the reactor chamber. It follows that ΔT will increase approximately linearly with reactor height; in the present design $\Delta T \simeq 4$ K at $h_{air}=3$ μm, and if arbitrarily the upper acceptable limit is $\Delta T_{max}=60$ K, then the upper limit on the reactor chamber height is $h_{air} \leq 45$ μm, with all other parameters unchanged. The limit on reactor chamber height may be lifted if forced convection cooling is applied to the glass lid surface through the center bore of the heater.

An increase in the thickness of the glass wafer is also seen to cause an increase in ΔT, but at the same time the heater temperature must be increased since $P_{Si,r}$ must be maintained to keep the temperature T_B at the bonding interface fixed.

In the heater and cold finger regions, the heat flow is three-dimensional. The transition to a radial heat flow in the heater region takes place on a length scale that is approximately h_G+h_{Si}, while at the cold finger the transition takes place on a length scale of approximately h_{Si} since here, the main heat flow is in silicon. It follows that the radial distance between heater and cold finger edges must fulfill $\Delta r_{hc} \gtrsim h_G+2h_{Si}$. Moreover, in the region directly above the cold finger, the length scale of the temperature variation is h_{Si}, and thus the cold finger radius must fulfill $r_{Cu} > h_{Si}$, say, $2h_{Si}$. A minimum applicable chip size could then be estimated from $2r_{min} \sim 2(2h_{Si}+h_G+2h_{Si}+w_H)$, where w_H is the width of the glass-heater contact; this probably has to fulfill $w_H > h_G+h_{Si}$, making $2r_{min} \sim 2(5h_{Si}+2h_G)=5.5$ mm with a cold finger radius $r_{Cu}=0.7$ mm. This design was verified by FEA.

With the current design, the temperature T_{Rc} in the center of the reactor (on the silicon side) is almost entirely controlled by the Cu cold finger $T_{Rc} \simeq T_L+R_{Cu}P_{tot}$, where T_L is the cold finger temperature (we have used $T_L=12$ °C) and $R_{Cu}=L_{Cu}/(\varkappa_{Cu}\pi r_{Cu}^2)+1/(4\varkappa_{Cu}r_{Cu})$ is the thermal resistance of the cold finger of length L_{Cu} including thermal spreading resistance to the Cu bulk. It follows that the reactor temperature is linearly dependent on the cold finger temperature, linearly dependent on the total heat flow, and strongly dependent on the cold finger geometry. This also emphasizes the importance of ensuring good thermal contact between silicon and the cold finger; thus we use thermogrease at that junction.

By heating from the glass side of the glass-silicon stack and providing efficient local cooling, we have shown that silicon may be anodically bonded to glass successfully while keeping small (<1 cm) areas at ambient temperatures. This is highly useful for any MEMS or lab-on-a-chip devices, which contain heat-sensitive components such as polymeric structures or coatings, antibodies, or other biomolecules or sensitive metallic structures. The method may be scaled down to bond individual chips as small as ~5.5 mm in diameter while keeping 1.4 mm diameter regions cold. Even smaller dimensions are possible with thinner silicon and Pyrex. Cavities up to ~45 μm deep may be used in the existing setup, while still keeping the reactor temperature below 100 °C. Finally, it should be possible to locally cool multiple areas/chips simultaneously when bonding whole wafers.

CINF is funded by the Danish National Research Foundation.

[1] P. R. Mallory, U.S. Patent No. 3397278 (1969).
[2] G. Wallis and D. Pomerantz, J. Appl. Phys. **40**, 3946 (1969).
[3] K. M. Knowles and A. T. J. van Helvoort, Int. Mater. Rev. **51**, 273 (2006).
[4] T. R. Henriksen, J. L. Olsen, P. C. K. Vesborg, I. Chorkendorff, and O. Hansen, Rev. Sci. Instrum. **80**, 124101 (2009).
[5] T. R. Anthony, J. Appl. Phys. **54**, 2419 (1983).
[6] K. B. Albaugh, J. Electrochem. Soc. **138**, 3089 (1991).
[7] S. Shoji, H. Kikuchi, and H. Torigoe, Sens. Actuators, A **64**, 95 (1998).
[8] Y. Huang, Z. Cui, G. Xiping, L. Changjiu, and G. Zhenan, J. Non-Cryst. Solids **354**, 1407 (2008).
[9] C. Lee, W. Huang, and J. Shie, Sens. Actuators, A **85**, 330 (2000).

Paper III

Gas-phase photocatalysis in μ-reactors
Peter C.K. Vesborg, Jakob L. Olsen, Toke R. Henriksen, Ib Chorkendorff, and Ole Hansen
Chemical Engineering Journal **160**:738 - 741, 016111, (2010)

Chemical Engineering Journal 160 (2010) 738–741

Contents lists available at ScienceDirect

Chemical Engineering Journal

journal homepage: www.elsevier.com/locate/cej

Gas-phase photocatalysis in μ-reactors

Peter C.K. Vesborg[a,*], Jakob L. Olsen[a], Toke R. Henriksen[a,b], Ib Chorkendorff[a], Ole Hansen[a,b]

[a] CINF, Dept. of Physics, Building 312, Fysikvej, Technical University of Denmark, DTU, DK-2800 Kgs. Lyngby, Denmark
[b] Dept. of Micro- and Nanotechnology, Technical University of Denmark, DTU Nanotech, Building 345 East, DK-2800 Kgs. Lyngby, Denmark

ARTICLE INFO

Article history:
Received 22 March 2010
Accepted 30 March 2010

Keywords:
Microreactor
Nanoreactor
Photocatalysis
Photooxidation
Methanol oxidation
CO oxidation
TiO_2
P25
W 2730X

ABSTRACT

Gas-phase photocatalysis experiments may benefit from the high sensitivity and good time response in product detection offered by μ-reactors. We demonstrate this by carrying out CO oxidation and methanol oxidation over commercial TiO_2 photocatalysts in our recently developed high-sensitivity reactors. We demonstrate that the system exhibits great versatility in terms of photocatalyst, illumination source and target reaction.

1. Introduction

Photocatalysis is the conversion of chemicals to other chemicals over a semiconducting catalyst which is activated by band-gap excitation as opposed to conventional catalysis where reactions are thermally activated. Photocatalysis may be used for elimination of unwanted chemicals such as pollutants in air or waste water by mineralizing, e.g. organics down to CO_2 and H_2O [1–3]. The second main use of photocatalysis is (solar) energy harvesting since a photocatalyst, unlike a thermal catalyst, may convert reactants to products of higher energy thereby storing some of the energy from the absorbed photons in chemical bonds [4].

The merits of μ-reactors in the study of catalysis have been broadly demonstrated [5–7], but only comparatively little work has been done to use the benefits of μ-reactors in the study of photocatalytic reactions [8–11]. We have recently reported the development of a new μ-reactor fabricated in silicon and sealed with a Pyrex lid [12]. Compared to previously published photochemical "micro"-reactors which typically are based on one or more channels of 10–1000 μm in depth and width [10] our reactors are quite different with their large frontal area combined with their *very* shallow chambers (3 μm depth) and resulting small volumes. This new design features a large frontal area of 0.78 cm^2 – useful for photocatalyst illumination – while keeping the total reactor volume down to ~240 nl giving very short time constants and high sensitivity due to the integrated direct quadropole mass spectrometer (QMS) interface. In this paper we demonstrate that these μ-reactors can be very useful in characterizing photocatalysts.

Focusing on the technique two commercial photocatalysts, P25 and W 2730X TiO_2-catalysts (both from Evonik—formerly Degussa) are used to photooxidize CO and methanol. CO oxidation has previously been established as a useful probe reaction for gas-phase photocatalysis [13,14] and methanol is a commonly used sacrificial reductant in photoelectrochemical studies [2].

2. Experimental

The μ-reactor system (fabrication, gas handling system, QMS detection, etc.) has been described in a previous publication [12]. Briefly, the reactors are planar (16 by 20 mm^2 by 0.35 mm silicon (+0.5 mm Pyrex lid)) with a circular active area of 10 mm diameter and a reactor volume of roughly 240 nl. Up to four simultaneous gas streams can be led to the reactor via two inlets (I1 and I2, Fig. 1C) and the reactor effluent is led to a quadropole mass spectrometer (QMS) for detection through a capillary (which limits the reactor flow to ~10^{15} molecules/s) via O2. The bypass flow which never enters the circular reactor area exits via O1. This bypass flow is normally chosen to be on the order of 10 sccm to get good regulation using off-the-shelf mass flow controllers.

Fig. 1A and B are cross-sections of the μ-reactor showing the two basic ways photocatalyst may be loaded into the reactor and that

* Corresponding author.
E-mail addresses: petervesborg@gmail.com, peter.vesborg@fysik.dtu.dk (P.C.K. Vesborg).

1385-8947/$ – see front matter © 2010 Elsevier B.V. All rights reserved.
doi:10.1016/j.cej.2010.03.083

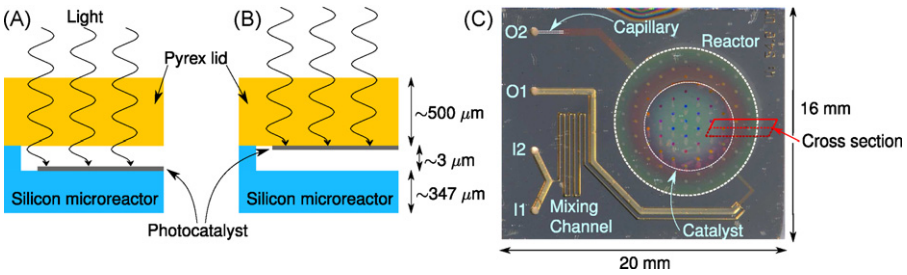

Fig. 1. Partial cross-sections of two different μ-reactors loaded in two different ways and a photograph of a μ-reactor. Sketch A shows that when photocatalyst is deposited on the silicon reactor the illumination is frontal – i.e. light is incident from the same side as the reactants – while sketch B shows that photocatalyst deposited on the Pyrex lid (as in the examples in this paper) is effectively illuminated from behind. Sketch C shows a top view of the reactor where main parts are indicated. Gas is let in via I1 and I2 and out via O1 and O2. O1 goes to a pressure controller and O2 leads from the reactor to the mass spectrometer. The location of the cross-sectional cut shown in A and B is also indicated in C.

they allow for both front-side and back-side illumination. The light sources available range from small, cheap LEDs directly over the reactor to a large Xe-arc broadband source (Newport model 66942 1 kW OF) which may or may not be filtered or passed through a monochromator before light is guided to the reactor with a fiber bundle terminated with a collimating optic. In the present paper we excite the photocatalysts using a small 4 W Hg lamp (UVP model UVGL-15). Regardless of the light source used the incident spectrum and intensity is recorded by replacing the reactor with the measurement head of a calibrated spectroradiometer (International Light model RPS-900R). The measured spectrum incident on the reactors in the present paper is shown in Fig. 2. Since some of the light is lost passing through the Pyrex lid due to reflection and absorption for the deeper UV we include the transmittance spectrum of the 0.5 mm Pyrex lids used to seal our reactors in Fig. 3. Even though Pyrex starts absorbing light at ~330 nm the lids are sufficiently transparent that experiments down to well below 300 nm are possible.

For the experimental examples presented in this paper the P25 and W 2730X photocatalysts are loaded onto the Pyrex lids which are subsequently bonded to the silicon reactors. This corresponds to sketch B of Fig. 1 and the photocatalyst is effectively illuminated from "behind". One advantage of depositing the photocatalyst on the glass lid is that it may be characterized by transmission UV–vis spectroscopy before measurements begin. The catalyst is deposited by spin coating. The suspension is made by sonication and the Pyrex area for deposition (circular, 8 mm diameter) is masked by "Blue Tape" (SWT20, Nitto Scandinavia AB). The thickness of the catalyst layer is controlled by the concentration of the suspension and the number of depositions in the spin coater. Once the catalyst is deposited (and possibly characterized by UV–vis or other techniques) the lid is anodically bonded to the reactor [15,12]. During anodic bonding the temperature of the catalyst is kept well below 100 °C using a special "locally-cooled anodic bonding" method [16].

Once the reactor is bonded it is mounted in the gas manifold fixture and the target gas mixture flow is started. It takes a while for the reactor and catalyst to dry (as evidenced by the $m/Z = 18$ signal in the QMS) and since trace water in our experience inhibits CO oxidation over TiO_2 care is taken that the chip is dry before experiments are started. Sometimes cycles of illumination and/or heating to ~100 °C are used to speed up the drying process. For methanol oxidation careful drying is not relevant since the reaction itself evolves water.

In general, the experiment consists of supplying the relevant reactant gas mixture to the μ-reactor and pulsing the light on and off while monitoring the relevant masses with the QMS. This procedure is conducted for all wavelengths and intensities of interest. Generally, illumination causes only negligible (<4 K) increase in reactor temperature, since the metallic gas manifold to which the reactor is clamped acts as a massive heat sink.

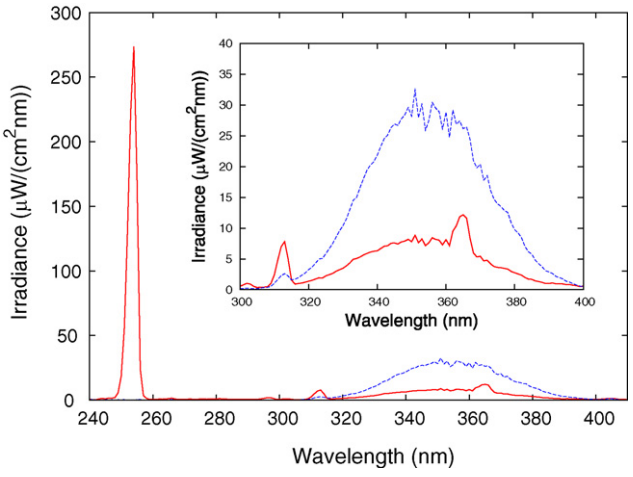

Fig. 2. Measured irradiation on the μ-rectors from the 4 W Hg lamp used in this paper. The lamp can be used in "short" wave mode (solid, red curve) and in "long" wave mode (dashed, blue curve). In the "short" wave mode the spectrum is dominated by the narrow Hg-line at 253.6 nm. (For interpretation of the references to color in this figure legend, the reader is referred to the web version of the article.)

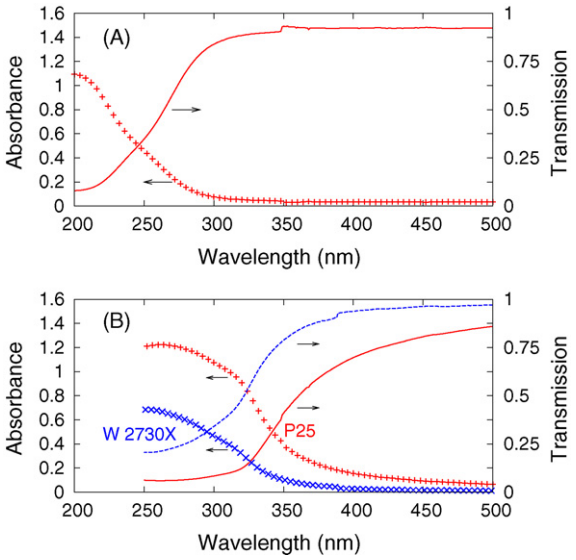

Fig. 3. (A) Measured absorbance and resulting transmission of a Pyrex lid. Above ~330 nm transmission is essentially flat at 0.92. (B) Absorbance and transmission of the TiO_2 samples studied measured against a blank Pyrex lid in the reference beam (A). The P25-based sample (red curves) has more absorption and scattering than the W 2730X-based sample (blue curves). The increased scattering of P25 is most pronounced at the higher wavelengths.

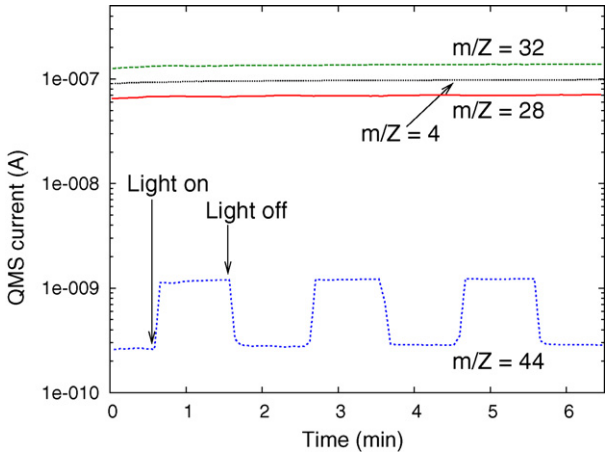

Fig. 4. Representative photooxidation experiment using "long" wave illumination (Fig. 2). QMS-current as a function of time. He, CO, O_2 and CO_2 (m/z: 4, 28, 32, 44) each sampled at 0.5 Hz are plotted. The CO_2 signal increases when the light is on and vice versa. The other channels are almost unaffected due to low turnover (<1%).

This method is also suited for long-term stability testing by leaving the light source on for prolonged periods before pulsing the light to measure photo activity. The setup is automated with LabVIEW (National Instruments) so that light sources, gas pressure and feed gas composition may be automatically scanned during longer experiments.

3. Photooxidation experiments

The photooxidation experiments presented in this letter serve to exemplify the method. For these experiments two reactors were prepared. Each was spin coated three times (6000 RPM, 10 s) with a $5\%_{mass}$ suspension in water (18 MΩ cm, "Millipore") of P25 and W 2730X, respectively. The resulting thickness was estimated by cross-sectional scanning electron microscopy to be approximately 400 nm on average in the case of the P25 catalyst and since the tapped density of P25 according to the data sheet is 130 g/l this corresponds to an upper limit of about $400 \times 10^{-7} \times 0.4^2 \times \pi\,\mathrm{cm}^3 \times 0.13\,\mathrm{g/cm}^3 = 2.6\,\mu\mathrm{g}$ of P25 in total in the μ-reactor.

3.1. CO photooxidation over P25

Oxidation of CO is, in principle, a very simple reaction: $CO(g) + 1/2(O_2)(g) \rightarrow CO_2(g)$. Fig. 4 shows time traces of the main components of the CO oxidation reaction gas: $m/z = 4$ (He used as internal reference), $m/z = 28$ (CO), $m/z = 32$ (O_2), $m/z = 44$ (CO_2). The nominal feed gas composition is 6:6:2 (He, O_2, CO) by volume and the total pressure is fixed at 1 bar. It is obvious from the time trace in Fig. 4 when the light is switched on and off. The reason that $m/z = 44$ does not drop to zero when the light is off is background reaction on the filament of the mass spectrometer—not dark reaction in the reactor. Fig. 5 shows the another experiment where the QMS is sampling mass 44 at 10 Hz and the light is toggled every 10 s. It is seen that the system reaches 90% of steady-state level in less than 2 s after the light is toggled. This high time-resolution is a key feature inherent in our μ-reactor design and allows for e.g. very fast experiments where illumination wavelength is scanned.

In order to confirm that photooxidation is indeed responsible for the signals, an experiment of heating the loaded reactors to about 100 °C in the dark was also tried, but no measurable dark activity was seen for these catalysts. As a further check, an empty reactor (without photocatalyst) was also tested and as expected this had no activity whatsoever under illumination or under heating.

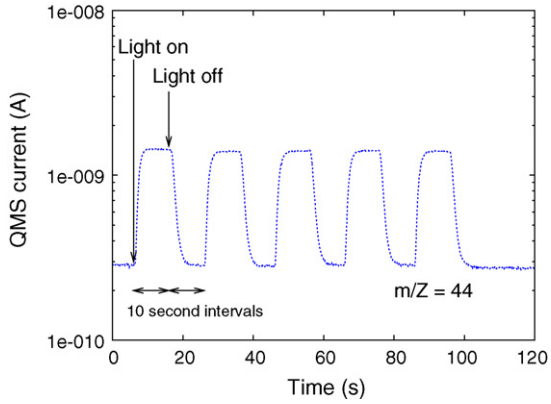

Fig. 5. Time trace of CO_2 signal sampled at 10 Hz and 10 s light on-off cycles using "short" wave illumination (Fig. 2). The very fast time response of the reactor is evident.

3.2. Methanol photooxidation

Methanol oxidation is slightly more complicated (and interesting) than CO oxidation. For instance it may be oxidized completely (mineralized): $CH_3OH(g) + (3/2)O_2(g) \rightarrow CO_2(g) + 2H_2O(g)$. Or it may oxidize partially to methanal ("formaldehyde" – CH_2O) or to methanoic acid ("formic acid" – HCOOH). In order to carry out the methanol photooxidation experiments a bubbler made of stainless steel filled with 2 ml of HPLC-grade methanol (Sigma–Aldrich) was inserted after one of the four MFCs supplying gas to our μ-reactor. The concentration of methanol is then conveniently adjusted by the ratio of clean helium to methanol-saturated helium (at the bubbler temperature which is monitored) controlled by the two corresponding MFCs. For the measurements presented in Figs. 6 and 7 the nominal ratio of partial pressures in the feed are 6:6:0.085 (He, O_2, MeOH) corresponding to about $0.7\%_{volume}$ of methanol. An experiment with about five times higher methanol concentrations was also tested, but resulted in a similar turnover as estimated by the $m/z = 44$ signal and is omitted here. For all experiments the methanol signal is monitored by the strongest feature in the cracking pattern at $m/z = 31$.

Figs. 6 and 7 both show methanol oxidation data, but with P25 and W 2730X and long and short wave illumination, respectively. The data clearly demonstrates that the photooxidation of methanol under these conditions takes *much* more time to reach

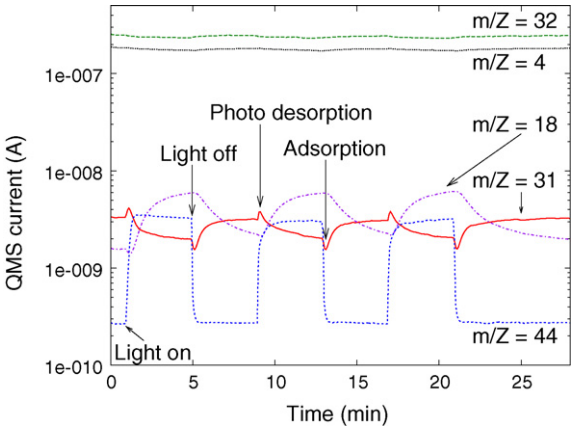

Fig. 6. Photooxidation of methanol over P25 photocatalyst using "long" wave illumination (Fig. 2). $m/z = 31$ is the main signal from methanol and $m/z = 18$ is the main peak from water. It is clear, that while the CO_2 signal responds quickly to illumination the metanol signal (and the water signal in particular) takes much longer to respond. Notable photo-desorption (and re-adsorption upon switching off the light) of methanol is observed.

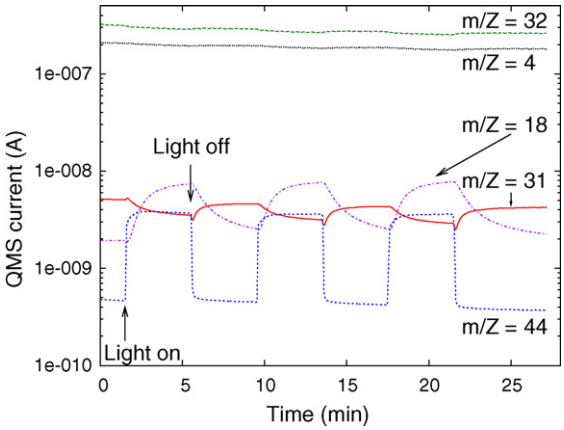

Fig. 7. Photooxidation of methanol over W 2730X photocatalyst using "short" wave illumination (Fig. 2). The overall picture is very similar to the P25 data (Fig. 4). However, the phenomenon of photo-desorption and re-adsorption is much less pronounced.

steady state when the light is toggled than it does with CO oxidation. The methanol signal and particularly the water signal both take many minutes to fully respond when the light is toggled. Another clear feature of the data is the apparent photo-desorption (and re-adsorption) of methanol when the light is toggled although it is less pronounced with the W 2730X reactor (Fig. 7). This phenomenon can only be resolved thanks to the fast time-resolution of the μ-reactor so even for this (somewhat slow to reach steady state) reaction the time-resolution is a useful feature.

A mass scan from m/z of 1–50 was also carried out to look for other (by)products and intermediates of methanol oxidation (such as formic acid), but nothing (that could not be assigned to cracking of water, methanol or CO_2) was detected in noteworthy concentrations so methanol seems to mineralize fully under these conditions.

4. Discussion

As illustrated by the examples of the previous section, the μ-reactor presented here is a versatile tool for characterization of photocatalytic performance. We show data for CO oxidation and methanol oxidation, but other reactions such as methane oxidation and ethanol oxidation have also been performed successfully. At present, experiments must be carried out in the gas-phase, but we are working on a liquid-capable version of the μ-reactor which would be suited for e.g. water-splitting experiments.

Compared to conventional, macroscopic batch reactors (generally hundreds of milliliters in volume and employing gas-chromatographic product detection) the μ-reactors are fundamentally different. The internal volume is smaller by about 10^6 times and this enables *flow* measurements instead of batch experiments. This gives a tremendous advantage in terms of time-resolution compared to batch reactors. Time-resolution is useful for studying transient phenomena (such as photoadsorption/desorption (see Fig. 6)) or recording temperature programmed desorption (TPD) spectra, but it also means that a series of measurements (e.g. the performance of a sample over a range of wavelengths—"action spectrum") can be recorded very fast (future publication).

The freedom to deposit the photocatalyst on either the Pyrex lid or the silicon reactor itself enables easy comparison between performance under frontal or back-illumination (Fig. 1). It is expected that for thin films of photocatalyst the performance should be the same regardless of illumination orientation, but for thick films, frontal illumination should give higher turnover (future publication).

Finally, the lower limit on illumination wavelength imposed by the transmission of the Pyrex lid is not really a hard limit. The optical absorbtion shown in Fig. 3 is for our standard lids which are 0.5 mm thick, but we have successfully "thinned" them to less than 100 μm in thickness by etching one side in dilute HF. This procedure results in significantly increased transmission in the 200–250 nm range making measurements on photocatalysts with a band-gap up to 6 eV practical.

5. Conclusion

We have shown that gas-phase photochemistry may be conveniently investigated using our silicon μ-reactors due to the transparency of the Pyrex lids in the relevant wavelength range. We carried out mineralization of methanol as a general representative of such reactions, but in principle anything of interest that has a practical vapor pressure could be substituted for methanol in the bubbler. The photocatalytic oxidation of CO has become the "standard" test reaction in our group since it is convenient to do and has near-instant response to illumination which allows for mass-transport studies in thick, mesoporous systems.

To our knowledge, the combination of excellent time-resolution (which gives mechanistic information on absorption/desorption and mass transport) and versatile high-sensitivity detection offered by on-line QMS is far better than anything achievable with more conventional "macro" reactors with $\sim 10^6$ larger reactor volumes and gas chromatograph product detection.

Acknowledgements

CINF is funded by the Danish National Research Foundation.

References

[1] U. Diebold, The surface science of titanium dioxide, Surface Science Reports 48 (5–8) (2003) 53–229.
[2] O. Carp, C.L. Huisman, A. Reller, Photoinduced reactivity of titanium dioxide, Progress in Solid State Chemistry 32 (1–2) (2004) 33–177.
[3] A. Fujishima, X. Zhang, D.A. Tryk, TiO_2 photocatalysis and related surface phenomena, Surface Science Reports 63 (12) (2008) 515–582.
[4] A. Fujishima, K. Honda, Electrochemical photolysis of water at a semiconductor electrode, Nature 238 (5358) (1972) 37–38.
[5] K.F. Jensen, Microreaction engineering—is small better? Chemical Engineering Science 56 (2) (2001) 293–303.
[6] S.K. Ajmera, C. Delattre, M.A. Schmidt, K.F. Jensen, Microfabricated cross-flow chemical reactor for catalyst testing, Sensors and Actuators B-Chemical 82 (2–3) (2002) 297–306.
[7] P. Mao, J.Y. Han, Fabrication and characterization of 20 nm planar nanofluidic channels by glass–glass and glass–silicon bonding, Lab on a Chip 5 (8) (2005) 837–844.
[8] R. Gorges, S. Meyer, G. Kreisel, Photocatalysis in microreactors, Journal of Photochemistry and Photobiology A: Chemistry 167 (2–3) (2004) 95–99.
[9] Y. Matsushita, T. Ichimura, N. Ohba, S. Kumada, K. Sakeda, T. Suzuki, H. Tanibata, T. Murata, Recent progress on photoreactions in microreactors, Pure and Applied Chemistry 79 (11) (2007) 1959–1968.
[10] E.E. Coyle, M. Oelgemoeller, Micro-photochemistry: photochemistry in microstructured reactors. The new photochemistry of the future? Photochemical & Photobiological Sciences 7 (11) (2008) 1313–1322.
[11] Y. Matsushita, N. Ohba, S. Kumada, K. Sakeda, T. Suzuki, T. Ichimura, Photocatalytic reactions in microreactors, Chemical Engineering Journal 135 (Suppl. 1) (2008) S303–S308.
[12] T.R. Henriksen, J.L. Olsen, P.C.K. Vesborg, I. Chorkendorff, O. Hansen, Highly sensitive silicon microreactor for catalyst testing, Review of Scientific Instruments 80 (2009) 124101.
[13] A. Linsebigler, G. Lu, J. Yates, Photocatalysis on TiO_2 surfaces—principles, mechanisms, and selected results, Chemical Reviews 95 (3) (1995) 735–758.
[14] J.T. Yates Jr., Photochemistry on TiO_2: mechanisms behind the surface chemistry, surface science 603 (10–12) (2009) 1605–1612, special Issue of Surface Science dedicated to Prof. Dr. Dr. h.c. mult. Gerhard Ertl, Nobel-Laureate in Chemistry 2007.
[15] G. Wallis, D. Pomerantz, Field assisted glass–metal sealing, Journal of Applied Physics 40 (10) (1969) 3946–3949.
[16] P.C.K. Vesborg, J.L. Olsen, T.R. Henriksen, I. Chorkendorff, O. Hansen, Anodic bonding with cooling of heat-sensitive areas, Review of Scientific Instruments 81 (2010) 016111.

Paper IV

Quantitative Measurements of Photocatalytic CO-Oxidation as a Function of Light Intensity and Wavelength over TiO2 Nanotube Thin Films in μ-Reactors

Peter C.K. Vesborg, Su-il In, Jakob L. Olsen, Toke R. Henriksen, Billie L. Abrams, Yidong Hou, Alan Kleiman-Shwarsctein, Ole Hansen, and Ib Chorkendorff

Journal of Physical Chemistry, Accepted 2010

ohio2/yjy-yjy/yjy-yjy/yjy99907/yjy2086d07z | xppws | 23:ver.3 | 5/8/10 | 4:39 | Msc: jp-2010-00552x | TEID: drh00 | BATID: 00000

Quantitative Measurements of Photocatalytic CO-Oxidation as a Function of Light Intensity and Wavelength over TiO_2 Nanotube Thin Films in μ-Reactors

Peter C. K. Vesborg,*,† Su-il In,† Jakob L. Olsen,† Toke R. Henriksen,‡ Billie L. Abrams,† Yidong Hou,† Alan Kleiman-Shwarsctein,† Ole Hansen,†,‡ and Ib Chorkendorff†

CINF, Department of Physics, Building 312, Fysikvej Technical University of Denmark, DTU DK-2800 Kgs. Lyngby, Denmark, and DTU Nanotech, Department of Micro- and Nanotechnology, Building 345 East, Technical University of Denmark, DK-2800 Kgs. Lyngby, Denmark

Received: January 20, 2010; Revised Manuscript Received: April 30, 2010

Gas-phase photooxidation of CO over TiO_2 catalysts (P25 and TiO_2 nanotubes) in μ-reactors with quantitative product detection was used to study turnover as a function of illumination intensity over 4 orders of magnitude. Turnover was found to be of order 0.84 in illumination intensity. A CO photooxidation action spectrum was also recorded for TiO_2 nanotubes. The action spectrum was used to calculate both the incident photon to product efficiency (IPPE) and the absorbed photon to product efficiency (APPE). The wavelength dependence of the IPPE was found to follow the absorption spectrum while the APPE was found to have a peak around 345 nm with a value of about 0.8%.

1. Introduction

In photoelectrocatalysis, it is a well established practice to measure photocurrent to estimate activity. Provided that it can be *proved* which reaction takes place at the photoelectrode and counter electrode (e.g., evolution of oxygen and hydrogen in the common case of water splitting), the current measured by the potentiostat gives a highly sensitive and convenient measure of photoactivity. However, in the case of photocatalysis where chemicals are converted into other chemicals on the photocatalyst surface, the absence of external current makes it much more problematic to quantify the photocatalytic activity. For both liquid and gas phase reactions, it is necessary to quantify product molecules, which is much harder than measuring a current. The problem of product detection is particularly difficult when, for example, the activity dependence on wavelength (action spectrum) is sought. Many wavelengths must be tested to give a reasonable resolution in the action spectrum, and monochromatic light sources tend to be weaker than broad band light sources. In practice, this often makes measurement of action spectra very time-consuming.

In this paper, we demonstrate how our μ-reactor system presents a novel and superior alternative to the traditional approach to such measurements. The traditional procedure is to place a macroscopic amount (1−1000 mg) of photocatalyst in a macroscopic (batch) reactor (1−1000 mL) made of glass, quartz, or metal and use a gas chromatograph (GC) to analyze small samples of the reactor content at suitable time intervals under illumination.[1,2] Some groups even employ reactors of several liters and other detection schemes (e.g., photoacoustic).[3,4] Other groups use flow (single pass) reactors, but these are also typically larger than 100 mL.[5]

Some groups have studied photocatalysis in small (millimeter size) flow reactors,[6−9] and our group has recently developed a μ-reactor with quadropole mass spectrometer (QMS) detection[10] and shown its suitability for (thermal) heterogeneous catalysis as well for as photocatalysis.[11] In the following, we present (i) how quantitative photocatalytic experiments may be carried out using our μ-reactor platform, (ii) how the large dynamic range of the reactor and QMS detector allows fast studies of photocatalytic turnover rate as a function of illumination intensity over 4 orders of magnitude and discuss how the results relate to the literature, and (iii) how the μ-reactor system can be used to record a detailed action spectrum of a photocatalyst in an automated fashion in only 2 h and calculate quantum efficiencies (incident photon to product efficiency, IPPE) and (absorbed photon to product efficiency, APPE).

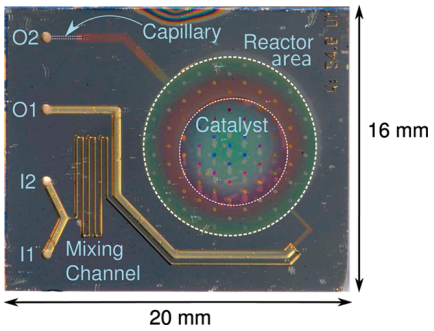

Figure 1. Photograph of a μ-reactor. I1 and I2 are gas inlets, and O1 is the outlet for the bypass flow. A small amount of gas (5×10^{14} or 5×10^{15} molecules/s depending on the type of reactor) is continually drawn from the reactor area via the flow-limiting capillary through O2 to the mass spectrometer for detection.

2. Quantitative Measurements in μ-Reactors

2.1. The μ-Reactor. There is no general consensus about what the term μ-reactor covers. We use the term to cover "chemical reactors with dimensions in the micrometer range". The general merits of such systems have been demonstrated by other groups.[12,13] Our μ-reactors seen in Figure 1 (described in detail elsewhere[10]), briefly, are 16 × 20 mm^2 chips fabricated from 350 μm thick silicon substrates and permanently sealed with a 500 μm thick Pyrex lid using anodic bonding[14] with local

* To whom correspondence should be addressed. E-mail: peter.vesborg@fysik.dtu.dk.
† DTU-CINF.
‡ DTU-Nanotech.

10.1021/jp100552x

cooling of the catalyst[15] (the catalyst is kept well below 100 °C during bonding). Each chip contains a circular reactor area of 0.78 cm^2, yet it has a total volume of only 240 nL (3 μm depth). Gas is continually led from the reactor area via a flow-limiting capillary to a QMS (Balzers model QMA125 with axial ionization and a secondary electron multiplier (SEM) detector) for instantaneous detection. This combination of a large area for illumination, with a fast time response (of this flow reactor) and a high sensitivity, makes the μ-reactor well suited for gas-phase photocatalytic studies.[11] Two kinds of chips with different capillary widths are available. These have an order of magnitude different flow conductance so that the flow through the reactor can be either $\sim 5 \times 10^{14}$ or $\sim 5 \times 10^{15}$ molecules/s depending on the experiment. The gas source, which feeds the reactor with this tiny flow, is the bypass flow channel. This can accommodate up to 20 mL/min, enabling conventional mass flow controllers to be used for gas supply,[10] and the reactor flow is independent of the main channel flow (it depends only on the main channel pressure which is fixed by a pressure controller within the useful range 0.05 to 5 bar). In the experiments, presented in this paper, the pressure is fixed at 1.00 bar and the feed gas composition is 3:3:1 ($He/O_2/CO$) by volume.

In this study, the samples are prepared by depositing the photocatalyst on the Pyrex lid (of the μ-reactor) before it is bonded onto a silicon chip to complete the loaded μ-reactor. The sample μ-reactor is then mounted in a gas manifold fixture, and the reactant gas mixture flow is started. The μ-reactor is subsequently heated to ~100 °C, until it is completely dry as evidenced by the water signal at $m/z = 18$, and no experiments are carried out before the water signal has reached a steady background level and the photoactivity has stabilized. This is important, because we have found photooxidation of CO to be inhibited by water as was also reported by Einaga et al.[16] In general, once the samples have been mounted and dried, the photocatalytic performance is very stable over time and reproducible, even if the reactor is dismounted and then remounted months later. Since the μ-reactor is a flow reactor, the typical experiment consists of toggling a light source on and off while recording all relevant masses with the QMS as a function of time (equivalent to measuring a photocurrent under chopped light).

2.2. Calibration Procedures. The raw data obtained from the μ-reactor setup consist of time series of currents, one for each m/z value being scanned. What is sought is the ability to convert from measured QMS currents to molecular flows (ampere → molecules/s). There are four steps to perform to convert from QMS currents to molecular flows, but step 1 must, in principle, only be done once and then only steps 2−4 (which are very quick) have to be performed with every new μ-reactor:

1. Measure the molecular flow of a "reference" μ-reactor by pumping down a known volume fitted with a baratron through the capillary of the reference μ-reactor. Call this flow R_{flow}. The unit is molecules/s. The details of this procedure may be found in ref 10.
2. Find the molecular flow of the sample μ-reactor, S_{flow} [molecules/s]. This is conveniently done by comparing the QMS current of a suitable gas component (this *inert* internal reference is typically He measured at $m/z = 4$) of the sample μ-reactor with the reference μ-reactor using the same gas mixture. This gives the relation

$$S_{flow} = R_{flow}\frac{S_{QMS}(inert)}{R_{QMS}(inert)} \quad (1)$$

where $(S_{QMS}(inert))/(R_{QMS}(inert))$ is the ratio of measured QMS currents [ampere/ampere] of the inert gas in the sample μ-reactor to the reference μ-reactor. This simple method of swapping the sample with the reference reactor is much faster and more convenient than doing a pump-down experiment (step 1) with every sample μ-reactor.

3. Measure the QMS signal for every interesting component, n, in a known gas mixture to find a set of calibration constants, C_n, (sensitivity factors):

$$C_n = S_{flow}\frac{f(n)}{S_{QMS}(n)} \quad (2)$$

where $f(n)$ is the fraction of the nth component of the gas ($\Sigma f(n) = 1$, where summation is over all components) and $S_{QMS}(n)$ is the QMS current measured for the nth component. Each calibration constant is the ratio of the molecular flow to the measured QMS current of a given gas, n. They capture differences in ionization probabilities and so on. In general, calibration constants are almost equal to each other (within 50%), except for He which has a low ionization cross section.

4. Now the molecular flow of each gas component, n, is given by

$$S_{flow}(n) = C_n S^*_{QMS}(n) \quad (3)$$

where $S^*_{QMS}(n)$ is the QMS signal that has been corrected for background in the QMS (including cracking and reaction on the filament). In the case of CO (photo)oxidation, this is easy, since there is no reaction in the dark (verified in separate experiments), so the dark CO_2 signal ($m/z = 44$) is the background and in the above equation $S^*_{QMS}(CO_2) = S_{QMS}(CO_2) - S_{QMS\text{-}dark}(CO_2)$.

The order of magnitude for molecular chip flow (S_{flow}) is 5×10^{14} molecules/s, that is, 10^{-9} mol/s for μ-reactors with the small capillary and ~10 times higher for μ-reactors with the large capillary.

Implicit in the calibration is the assumption that the QMS is linear (i.e., a 10 times reduction in pressure of a given gas component in the QMS results in a signal that is exactly 10 times lower). A linearity calibration of the mass spectrometer has been carried out, and we have no reason to suspect any nonlinearity leading to a systematic instrumental error. We also note that we generally see mass balance for carbon and oxygen: $CO + CO_2 =$ constant and $2O_2 + CO + 2CO_2 =$ another constant.

3. Samples and Sample Preparation

Sample "A" was simply P25 (AEROXIDE P25, Evonik (formerly Degussa)) spin coated in a masked 8 mm disk on a Pyrex lid by the method given in ref 11. The resulting film thickness was estimated to be 225 ± 25 nm by SEM on similarly prepared samples. The lid was then bonded (as explained in section 2) to a wide-capillary silicon chip to complete the μ-reactor.

Sample "B" consisted of an 8 mm diameter disk of TiO_2 nanotubes (TiO_2 NTs) formed on the Pyrex lid by potentiostatic anodization of a metallic titanium film[17,18] (400 nm thick, 8 mm diameter) which was deposited on the Pyrex lid using electron beam evaporation. TiO_2 NTs have attracted much attention in recent years[19] due to their favorable combination of photocata-

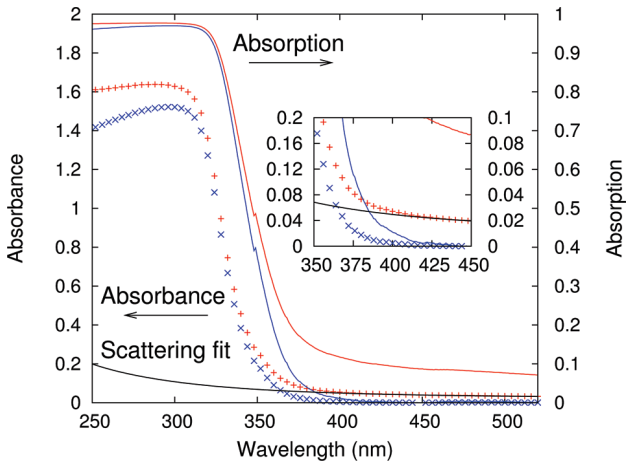

Figure 2. Absorbance ($A = \log(I_0/I)$) of sample "B" (red plus signs, left ordinate) measured against a blank Pyrex lid in the reference beam. The black curve is a fit ($A_{scattering} = C_1/\lambda^4 + C_2$) to the data above 400 nm as a simple model of the scattering losses. Subtraction of the fit from the absorbance is plotted with blue crosses and represents the "scattering corrected" absorbance. The right ordinate is the resulting absorption ($1 - I/I_0$), red and blue solid curves. Again, the blue curve is the "scattering corrected" data. The inset shows a close-up of the band edge region. For instance, it can be read off the blue curve that only below 385 nm does the nanotube film absorb more than 2% of the incident photons. Scattering (black line) is probably overestimated at short wavelengths, since scattered photons have a high absorption probability due to short absorption length, but the error due to this is insignificant since raw and corrected absorbance remain essentially equal at short wavelengths (both above 95%).

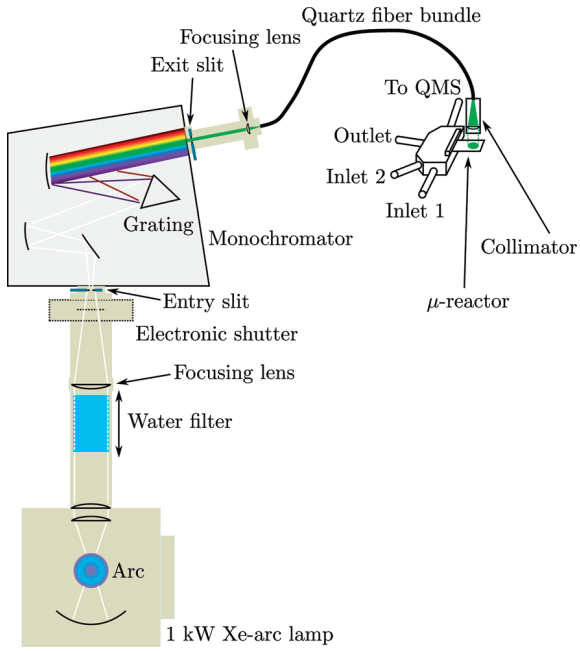

Figure 3. Schematic of the monochromated Xe-arc source used for measuring action spectra. The irradiance of the system at all relevant settings (choice of wavelength, slits, and grating) is measured by putting the measuring head of a calibrated spectroradiometer in the place of the μ-reactor. This irradiance measurement is carried out immediately before or after the actual measurement on the μ-reactor.

lytic performance and mass transport properties. Prior to anodization, the samples were cleaned with acetone and ethanol followed by a deionized water rinse. The anodization was performed using a two-electrode cell with the titanium film as the working electrode and carbon paper as the counter electrode. The anodization was complete within ~1 h at a constant applied voltage of 10 V at room temperature in an electrolyte mixture of $0.3\%_{mass}$ NH_4F (98% + ACS reagent, Sigma Aldrich) and $2\%_{volume}$ H_2O in ethylene glycol (99%, Sigma-Aldrich).[20] In order to get complete anodization without loss of electrical contact, the so-called "bottom contact" method[21] was used. After growing the TiO_2 NT film, the lid was annealed in a furnace at 723 K for 2 h. The resulting film consisted of ordered arrays of nanotubes of about 400 nm length (thickness of the film), ~30 nm in outer diameter, and ~20 nm in inner diameter (estimated from scanning electron micrographs of similarly prepared samples). X-ray diffraction (XRD) peaks in the annealed film were all assigned to anatase, but of course XRD cannot rule out that some TiO_2 might remain amorphous after annealing.[22]

F2 Figure 2 shows the UV−vis spectrum of the TiO_2 NT sample "B" measured (with a Cary model 1E spectrophotometer) against a blank Pyrex lid. Thus, the resulting apparent absorption is only due to absorption and scattering of the TiO_2 film; the absorption due to the Pyrex itself is therefore not contributing to the measured absorbance in the figure. Figure 2 also shows a fit of the scattering background of the form $A = C_1/\lambda + C_2$, where C_1 and C_2 are fitted using the Levenberg−Marquardt method. (Since the characteristic feature size is $r \lesssim 30$ nm for both P25 and TiO_2 NTs, then $2\pi r/\lambda \ll 1$ for $\lambda > 400$ nm and thus Lorentz−Mie scattering reduces to Rayleigh scattering in a first approximation.) The scattering was fitted in the (near) above-gap region 400−600 nm (3.1−2.07 eV) since the anatase nanotubes have a band gap, $E_g \approx 3.2$ eV. Figure 2 shows the resulting "corrected" absorption data for the sample (where the fitted scattering component has been subtracted). The scattering correction will be needed for the discussion of absorbed photon to product efficiency and action spectra (section 6). After UV−vis characterization, the lid was bonded to a narrow-capillary silicon chip. The samples both have the photocatalyst sitting on the glass lid so they are both illuminated "from behind" with respect to the reactant gas mixture flowing through the reactor as explained elsewhere.[11] (An investigation of frontal illumination versus back-illumination will be published (in preparation).)

4. Light Sources

Two very different light sources are used in this work. The first is a high-power UV-LED source (Hamamatsu model LC-L2) fitted with a focusing lens assembly (Hamamatsu L10561-220) suited for areas of 8 mm in diameter. The peak wavelength is ~367 nm, and the fwhm (full width at half-maximum) is ~9 nm. In our setup, an average irradiance on the sample μ-reactor of ~645 mW/cm^2 at full power was measured using a calibrated spectroradiometer (International Light model RPS-900R). The LED unit may be electronically tuned down to 10% of full power. Combination with simple neutral density (ND) filters of optical density 1.0 and 2.0 (Newport Corp.) makes a few extra orders of magnitude in light intensity available. A range of combinations of filters and power settings were measured using the spectroradiometer to calibrate for the exact extinction of the individual ND filters (which at 367 nm is not exactly equal to their nominal values).

F3 The second light source is shown in Figure 3. The main components include an (ozone free) 1 kW Xe-arc source (Newport model 66924) equipped with a water filter to eliminate unwanted long-wave light, and for this study it was fitted with a monochromator (Newport Cornerstone 260) and appropriate optics for F-number matching. The output is coupled via a quartz fiber bundle through a collimating lens onto the sample μ-reactor.

ohio2/yjy-yjy/yjy-yjy/yjy99907/yjy2086d07z | xppws | 23:ver.3 | 5/8/10 | 4:39 | Msc: jp-2010-00552x | TEID: drh00 | BATID: 00000

The μ-reactor and catalyst are kept at room temperature in all experiments, since the μ-reactor is clamped to a metallic gas interface manifold which acts as a heat sink measured $\Delta T < 4$ K at full power illumination[11] (250 mW with the Hamamatsu LED). As a case in point, assume that an optical power, P, is absorbed in the TiO_2 film on the Pyrex lid, then the maximum temperature rise of the film can be estimated by the heat conductance of the gas film: $\Delta T = (h_{air}/\kappa_{air})P/A$, where A is the illuminated area, h_{air} is the reactor height, and κ_{air} is the heat conductivity of the reactant mixture. With $\kappa_{air} = 0.025$ W/(mK), $h_{air} = 3$ μm, and $P/A = 250$ mW/0.50 cm^2, we find $\Delta T = 0.6$ K, and in the experiments presented in this paper the temperature rise is even less because the helium content of the reaction mixture has high heat conductivity.

5. Intensity Dependence

5.1. Motivation. The high sensitivity of the μ-reactor system which enables flow experiments where steady state conditions can be ensured is a great advantage compared to batch reactors. This merit, in combination with the fact that the QMS offers a very wide dynamic range (ratio of minimum detectable signal to maximum practical conversion which is limited by "full conversion"), makes the μ-reactor platform highly suited for investigations of how the photocatalytic conversion scales with illumination intensity. It is of interest to know how well a given photocatalyst performs as a function of illumination intensity for at least three reasons. The first reason is practical: In a given photocatalytic converter where higher conversion is needed, would it be more economical to increase photocatalyst amount/surface area, or would a more powerful light source with the same amount of photocatalyst be the better choice? The second reason is that when trying to characterize the photocatalytic performance as a function of illumination wavelength (action spectrum) it may be important to correct measured turnover for intensity variation when the tunable light source does not provide the same irradiance at different wavelengths. For example, when using an Xe-arc lamp with a monochromator to record action spectra, as is commonly done in many laboratories and as we do in section 6, the irradiance on the sample will often vary by an order of magnitude (or more) as the wavelength is scanned, so that, effectively, *two* parameters (wavelength *and* irradiance) are scanned simultaneously; if the turnover is not linear in irradiance for a given sample, then the action spectrum must be corrected for that. The third reason for measuring intensity dependence is that it gives mechanistic insight about the sample. For example, it is often claimed that in the limit of low light intensity (where mass transport is not a limiting factor) turnover should scale linearly with incident photon flux. Furthermore, it is claimed that at higher irradiance levels turnover becomes proportional to (irradiance)$^{0.5}$ due to substantial carrier recombination. Experimental support for this was found by Egerton and King[23] by oxidizing isopropanol to acetone over rutile TiO_2 and commercial pigments in the liquid phase while varying irradiance over 5 orders of magnitude. Later, however, Ohko et al.[1] studied the same reaction in gas phase over a TiO_2 thin film at very low light intensities (45 μW/cm^2 down to 36 nW/cm^2, with the latter corresponding to only 6.6×10^{10} photons/(cm^2 s)) and found (as long as the isopropanol concentration was above 10 ppmv) turnover to be proportional to (irradiance)$^{0.8}$ over their 3.5 orders of magnitude in irradiance.

Given that our μ-reactor setup uses a mass spectrometer (as opposed to a gas chromatograph) for detection and that one should always choose to use probe reactions with a well-defined stoichiometry,[22] we have chosen photooxidation of CO. Photooxidation of CO has previously been established as an interesting probe reaction for photocatalysis over TiO_2. It has been studied over single crystals at low temperatures[24] and over powders at room temperature.[16,25] For plain TiO_2, Einaga et al.[16] observe that water vapor inhibits photooxidation of CO. We have also observed this inhibiting effect[11] and therefore take great care to dry our reactors until activity is stable before performing any measurements as explained in section 2. In addition to pure TiO_2, refs 16, 24, and 25 also study platinized TiO_2, and in the case of Einaga et al.[16] also the effect of water vapor and of light intensity, and find that platinized systems are less sensitive to water than plain TiO_2 is.

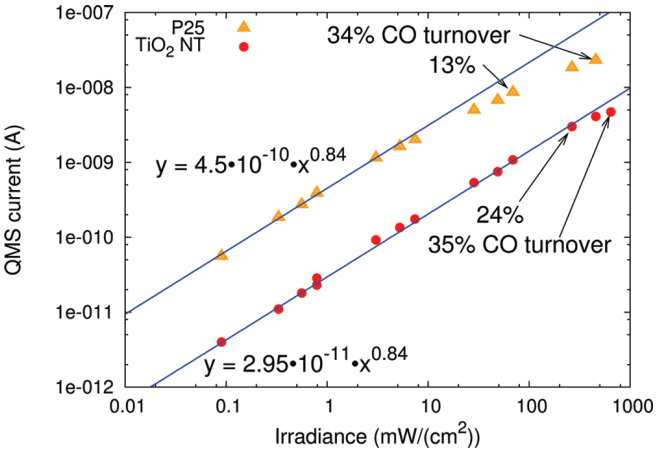

Figure 4. Background-corrected $m/z = 44$ (CO_2) QMS signal as a function of measured irradiation on the reactor with $\lambda = 367$ nm peak wavelength. For the nanotube μ-reactor (sample "B"), it is seen that, except for the highest illumination intensities where the effective feed gas composition is altered by high turnover in the reactor (final two data points where well over 10% of the CO is photooxidized to CO_2), the turnover versus illumination intensity is very well described by a power function. The apparent slope (power) is 0.84, meaning that a doubling of the light intensity only results in a factor 1.79 times more turnover. This relation holds true over 4 orders of magnitude of light flux, from moderate to very high flux (90 to 645 mW/cm^2 = 1.7×10^{14} to 1.2×10^{18} photons/(cm^2 s)). Also in the case of P25 (sample "A"), it seems that the turnover is proportional to illumination intensity to the power of about ~0.84. At intensities above ~5 mW/cm^2, however, the power law fails (or changes to a lower power), but it cannot be ruled out that this is due to transport limitations in the P25 film.

5.2. Results. In order to be able to study illumination intensity dependence over a large range of intensities, we have used our Hamamatsu LED unit (section 4) because it is fairly monochromatic at 367 nm and it can provide a high irradiance over the reactor area.

Two μ-reactors, "A" with P25 and "B" with TiO_2 NTs (section 3), were used for the experiments. For both samples, the light intensity is almost constant over the thickness of the sample because the photocatalyst layers are very thin and because of the proximity of the 367 nm central wavelength to the band edges. Especially for the nanotube μ-reactor, its absorption edge is at ~380 nm, so in simple transmission only about 10% is absorbed at 365 nm (see Figure 2). This means that for both samples the excitation rate should be approximately constant everywhere in the photocatalyst layers. Figure 4 shows data for measured CO_2 production (measured as the $m/z = 44$ QMS current where the constant background signal has been subtracted) as a function of measured irradiance (centered at 367 nm) for the two different μ-reactors from 90 to 645 mW/cm^2. For comparison, integration of the AM1.5G spectrum (ASTM G173-03 solar spectrum) in the 10 nm interval from

365 to 374 nm gives 0.67 mW/cm^2. The data are presented in a log−log plot, so if turnover were proportional to illumination intensity the data would fall on lines of slope 1. For the nanotube μ-reactor, it is remarkable that the turnover versus intensity falls on a straight line over 4 orders of magnitude (of course, as a substantial fraction of the available CO is converted in the final couple of data points, the linearity fails). Turnover is *not* proportional to irradiance (slope $\neq$ 1), but rather to irradiance raised to the 0.84 power (the reaction is of order 0.84 in irradiance). For P25, the same slope is seen at moderate irradiance up to about 1 mW/cm^2, but above 5 mW/cm^2 the slope is lower. This could be due to a change in mechanism, but it could just as well be due to transport limitations.

To ensure that the slope of 0.84 is not somehow an artifact of the illumination wavelength being close to the band edge, a similar experiment (not shown) was conducted with a mercury lamp at 254 nm (strong line in the Hg spectrum) with the nanotube sample, although the illumination could only be varied over 1 order of magnitude for practical reasons. The result under those conditions of much higher photon energy was that the turnover seemed proportional to irradiance to the 0.75 $\pm$ 0.06 power.

5.3. Discussion. As mentioned in the above motivation, the nonlinearity of photocatalytic conversion in irradiance for CO oxidation and other gas (and liquid) phase photocatalytic reactions over TiO_2 have previously been reported in literature. Peral and Ollis[26] note for acetone oxidation in gas phase that $r \propto I^{0.7\pm0.1}$ (I is irradiance, and r is rate) over 1 order of magnitude and conclude that they are in the "transition regime" between the values of 0.5 (recombination dominated) and 1.0 (light limited). Aguado et al.[27] report that for one of three different colloids they test for formic acid decomposition in liquid phase they find that $r \propto I^{0.78\pm0.2}$ (the two other colloids have even lower exponents). Einaga et al.[16] studying CO oxidation at high light intensities (~1−10 W/cm^2) find that $r \propto I^{\sim0.7}$ for TiO_2 (and $r \propto I^{\sim0.5}$ for platinized TiO_2). Hwang et al.[28] find $r \propto I^{0.73\pm0.1}$ for CO oxidation over platinized TiO_2 (~0.03−3 mW/cm^2). Even Ohko et al.[1] who measure isopropanol oxidation in the gas phase over 3 orders of magnitude at what they call "extremely low" light intensities and arrive at $r \propto I^{0.8\pm0.04}$ conclude that they are in a "transition region" between the two asymptotic values.

Considering that Ohko et al.[1] measure $r \propto I^{0.8\pm0.04}$ with I from 36 nW/cm^2 to 45 μW/cm^2 and that we measure $r \propto I^{0.84\pm0.03}$ with I from 90 μW/cm^2 to 645 mW/cm^2 (albeit for a different kind of TiO_2 film and a different reaction), it seems unreasonable that the combined 7 orders of magnitude in light intensity where $r \propto I^{\sim0.8}$ is just a "transition region" between the low light limit where supposedly $r \propto I$ and the recombination dominated region where supposedly $r \propto I^{0.5}$. A related question is whether anyone has really ever measured $r \propto I^{1.0}$.

Egerton and King[23] show that only one pigment (out of the three commercial pigments plus rutile that they test) shows $r \propto I^1$ at low light intensities, and this conclusion is based on only two data points; the rest of the data for that pigment at higher intensities show $r \propto I^{\sim0.5}$ as does the data for the other two pigments. We hesitate to conclude that turnover can never be truly proportional to incident photon flux, but it appears that it is hard to find a (TiO_2-based) photocatalyst and a probe reaction where this can be measured in practice.

6. Action Spectra

Another great benefit of the fast response and low detection limit offered by the μ-reactor platform in photocatalysis is the collection of action spectra. "Chemical", photocatalytic action spectra are useful and complement traditional "electrical", photoelectrocatalytic action spectra. This is because reactivity is measured under true zero-bias conditions without the influence of the solid−liquid junction on band structure and without possible artifacts due to non-faradaic photocurrent.

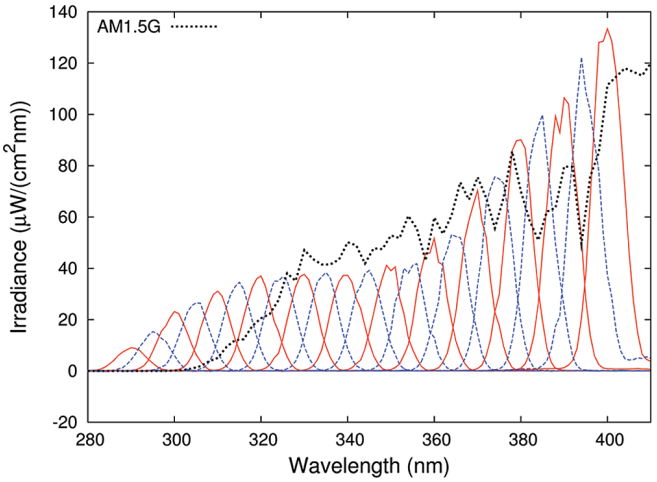

Figure 5. Irradiance spectra measured at the μ-reactor surface for all the monochromator settings used for recording action spectrum. For clarity, every other wavelength measurement (290, 300, 310, etc.) is plotted with solid, red and every other wavelength (295, 305, 315, etc.) in dashed, blue. Note that in the wavelength interval (310−370 nm) the irradiance is constant within a factor 2. AM1.5G (dotted, black line) is included for comparison.

Most tunable and monochromatic sources provide only modest irradiation levels; thus, the measurement of photocatalytic action spectra with traditional large volume (batch) photoreactors and gas chromatographic product detection can take many hours of illumination to obtain a quantifiable product concentration at every wavelength. This long time scale can complicate the measurements due to adsorption of both reactants and products during the measurement, not least because of the unfavorable ratio between active catalyst area and reactor inner surface area that is typical of large reactors. In the case of the μ-reactor, the same measurement can be quite fast because the μ-reactor has sufficient sensitivity that flow experiments are possible. In this section, we present an action spectrum for the TiO_2 nanotube sample "B" measured from 290 to 400 nm in 5 nm intervals, all recorded in 135 min using an automated LabVIEW program.

The raw measurements of the monochromated output of the Xe light source at every wavelength used in the study are presented in Figure 5 (for a description of the light source, see section 4). With this instrumental configuration, the fwhm is on the order of 9 nm and the peak irradiance is around 40 μW/(cm^2 nm) for central wavelengths in the relevant range (~300−370 nm). As a reference, AM1.5G is also shown in Figure 5 and it is seen that its irradiance is of the same order of magnitude as the monochromator output. No effort was made to keep irradiance constant over the wavelength interval. Given the results from the previous section, such extra refinements might be relevant for highly accurate characterization, but for the purpose of demonstrating the technique it was considered unnecessary, not least because irradiance is constant to within a factor of 2 in the 310−370 nm interval.

For photon-to-product molecule efficiency calculations, it is the number of incident photons (not incident power) that is the relevant parameter. The conversion, photon flux = power flux/(photon energy), has been carried out, and the result is plotted

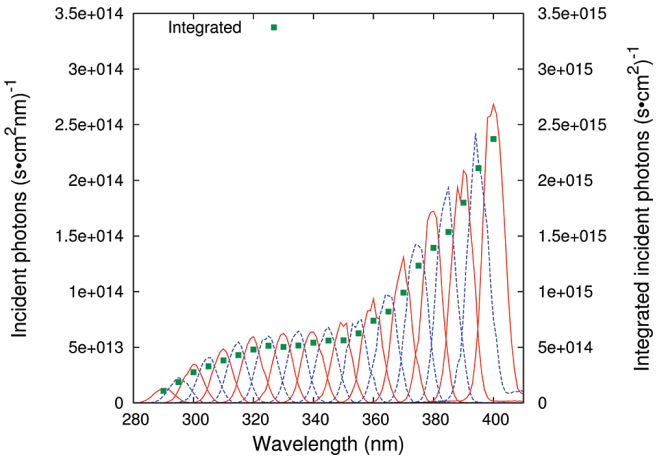

Figure 6. Data from Figure 5, but converted to photon flux density (instead of energy flux density). The green squares show the integrated photon flux density at each monochromator setting (second ordinate). This flux density is on the order of 5×10^{14}/(cm^2 s) in the relevant wavelength range < 375 nm.

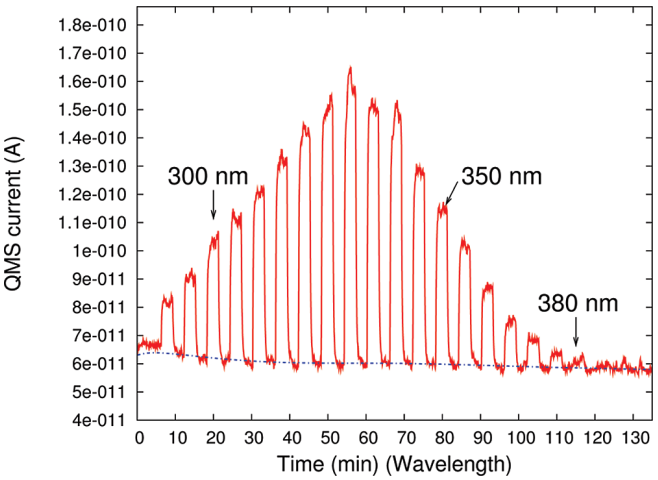

Figure 7. Raw CO_2 ($m/z = 44$) action spectrum data. The wavelength is incremented in 5 nm steps from 290 nm every 12 min while the shutter is toggled every 6 min. The dashed blue line shows the fitted background signal in the QMS.

F6 in Figure 6 which also includes the integrated photon flux density for every monochromator setting in units of photons/(cm^2 s). The light output from the monochromator is moderate, for example, at 350 nm the integrated flux density of 6×10^{14} photons/cm^{2}s which corresponds to 325 μW/cm^2 (Figure 6).

Having calibrated photon fluxes, the next step is to mount a μ-reactor and measure turnover at each monochromator setting. The resulting time trace of the $m/z = 44$ signal (CO_2) is plotted F7 in Figure 7. In this case, the light is on for 6 min, off for 6 min and the wavelength is changed every 12 min. Raw data such as those shown in Figure 7 may be converted to more useful units of CO_2 molecules/s versus wavelength by applying the QMS calibration procedure explained in section 2. Applying this calibration and taking an average figure for CO_2 turnover at F8 each wavelength gives the data presented in Figure 8. This figure shows the calibrated CO_2 turnover at every wavelength and, for convenience, also integrated incident photons/s and the estimated number of absorbed photons at each monochromator setting (both right ordinate). The integrated number of incident photons is, of course, simply the data from Figure 6 multiplied by the geometric area of the photocatalyst in the μ-reactor, in this case $\pi(0.4\text{ cm})^2 = 0.50$ cm^2. The number of absorbed photons is calculated as the incident photons multiplied by the

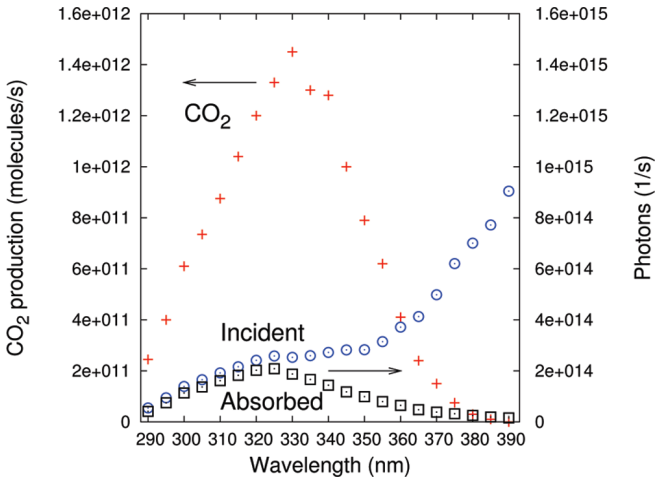

Figure 8. Background corrected CO_2 (From Figure 7) converted to units of molecules/s as described in section 2 (red + symbols). Also shown (right ordinate) is the integrated incident and absorbed photons/s (data from Figure 6 multiplied by the active photocatalyst area).

probability that a photon (which has made it through the Pyrex lid) is absorbed: $\Phi_{abs} = \Phi_0(1 - P_{Pyrex}(\lambda))P_{Sample}(\lambda)$, where Φ_0 is the incident light flux, $P_{Pyrex}(\lambda)$ is the fraction of photons absorbed by the 500 μm thick Pyrex lid, and $P_{Sample}(\lambda)$ is the probability that a photon (which reaches the sample) is absorbed by the sample. $P_{Sample}(\lambda)$ is estimated as the "scattering corrected" absorbance of the TiO_2 film as explained in section 3, and $P_{Pyrex}(\lambda)$ (which includes reflection losses) is found by measuring a blank Pyrex lid in the spectrophotometer. (The Pyrex lid transmits >90% down to about 330 nm and ~80% at 290 nm.[11]) The only step left to get an action spectrum is to divide the CO_2 production by the photon count at every wavelength (and possibly by an intensity correction term if $r \propto / I^1$ (see section 5) *and* if the output from the monochromator varies a lot (e.g., 10×) over the wavelength interval).

The result is shown in Figure 9 (no intensity correction) which F9 shows the incident photon to product efficiency (IPPE) as well as the absorbed photon to product efficiency (APPE). The IPPE, the *apparent* quantum yield, is really the photocatalytic (chemical) equivalent of the photoelectrocatalytic (photocurrent, IPCE) action spectrum. For the catalyst tested here, it takes about 220 incident photons (of $\lambda \lesssim 340$ nm) to make one CO_2 molecule (IPPE of 0.45%). Above 340 nm, the IPPE rapidly drops off, reflecting the fact that photons close to the absorption edge have a high probability of penetrating the film without being absorbed (Figure 2). The APPE is the same as the intrinsic quantum yield except that it includes no corrective factor for the number of photons ($e^- + h^+$ pairs) needed for the reaction. In the present case, the APPE reaches a maximum of about 0.8−0.9% (corresponding to one CO_2 molecule for every ~120 absorbed photons) for wavelengths in the interval 330−355 nm. At lower wavelengths, there is a drop-off in the APPE down to about 0.55% below 315 nm. We suspect that this is due to the decreased average penetration length of high energy photons. At 315 nm, for example, 60% of the photons are absorbed within the bottom 100 nm of the 400 nm TiO_2 nanotube film (this may be derived from the absorbance data in Figure 2), and since the sample is illuminated from the back, with the respect to the reactants, it seems reasonable that high energy photons result in less CO_2 than lower energy photons, given that they are absorbed (APPE). At 350 nm, less than 50% of the photons are absorbed by the entire 400 nm of the film, so for $\lambda > 350$ nm the excitation is nearly homogeneous. The reason for the drop in APPE at higher wavelengths is less obvious. One possibility

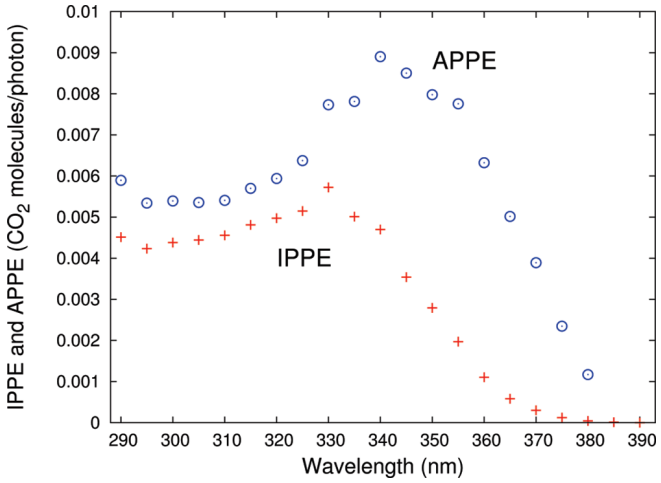

Figure 9. IPPE and APPE. Up to ∼340 nm, one CO_2 molecule results for every ∼200 photons incident on the reactor. At wavelengths above ∼340 nm, the IPPE quickly drops off, reflecting the fact that many photons pass the TiO_2 nanotube layer unabsorbed. Considering only the fraction of photons absorbed, the APPE, it is clear that higher wavelength may well induce turnover, up to about 380 nm. The APPE has a broad maximum at 345 ± 15 nm where the efficiency is about 0.8%. The APPE data at 290 nm and, particularly, above 370 nm is very uncertain. This is because it is calculated as conversion divided by absorbed photons and in the extremes of the plot both denominator and numerator are close to zero.

is that even though photons are absorbed, some may only excite localized interband states where the electron−hole pair is not free to migrate to the surface as opposed to "real" above-band gap excitation where the charge carriers have a chance to reach the surface and induce CO-oxidation. This could explain the drop in APPE above 350 nm. We note that the APPE data for $\lambda = 375$ and 380 nm have a very high uncertainty because both the numerator (turnover) and the denominator (absorbed photons) tend toward zero for higher wavelengths (Figure 8).

7. Conclusions

We have demonstrated that μ-reactors may be a convenient alternative to macroscopic reactors for obtaining quantitative information about photocatalytic performance. Specifically, we have investigated photooxidaiton of CO over TiO_2 thin films (P25 and nanotubes) at room temperature and found turnover for both types of TiO_2 to be proportional to irradiance to the power of 0.84 ± 0.03 over 4 orders of magnitude in irradiance (moderate to high irradiance). We have also determined the action spectrum for the TiO_2 nanotubes and found the incident photon to product efficiency to be almost zero above 375 nm, that it has a small peak around 330 nm, and that it is almost constant below 320 nm. This corresponds closely to the (scattering corrected) absorbance of the sample. We also estimated the absorbed photon to product efficiency, which is peaked around 345 nm, a significantly higher wavelength than the IPPE.

Acknowledgment. CINF is funded by the Danish National Research Foundation.

References and Notes

(1) Ohko, Y.; Hashimoto, K.; Fujishima, A. *J. Phys. Chem. A* **1997**, *101*, 8057–8062.
(2) Varghese, O. K.; Paulose, M.; LaTempa, T. J.; Grimes, C. A. *Nano Lett.* **2009**, *9*, 731–737.
(3) Yu, J.; Yu, J. C.; Leung, M. K. P.; Ho, W.; Cheng, B.; Zhao, X.; Zhao, J. *J. Catal.* **2003**, *217*, 69–78.
(4) Yu, J.; Su, Y.; Cheng, B. *Adv. Funct. Mater.* **2007**, *17*, 1984–1990.
(5) In, S.; Orlov, A.; Garcia, F.; Tikhov, M.; Wright, D. S.; Lambert, R. M. *Chem. Commun.* **2006**, 4236–4238.
(6) Gorges, R.; Meyer, S.; Kreisel, G. *J. Photochem. Photobiol., A* **2004**, *167*, 95–99.
(7) Matsushita, Y.; Ichimura, T.; Ohba, N.; Kumada, S.; Sakeda, K.; Suzuki, T.; Tanibata, H.; Murata, T. *Pure Appl. Chem.* **2007**, *79*, 1959–1968.
(8) Coyle, E. E.; Oelgemoeller, M. *Photochem. Photobiol. Sci.* **2008**, *7*, 1313–1322.
(9) Matsushita, Y.; Ohba, N.; Kumada, S.; Sakeda, K.; Suzuki, T.; Ichimura, T. *Chem. Eng. J.* **2008**, *135*, S303–S308; Microreaction Technology IMRET 9: Proceedings of the Ninth International Conference on Microreaction Technology - IMRET9 Special Issue.
(10) Henriksen, T. R.; Olsen, J. L.; Vesborg, P. C. K.; Chorkendorff, I.; Hansen, O. *Rev. Sci. Instrum.* **2009**, *80*, 124101.
(11) Vesborg, P. C. K.; Olsen, J. L.; Henriksen, T. R.; Chorkendorff, I.; Hansen, O. *Chem. Eng. J.* **2010**, http://dx.doi.org/ 10.1016/j.cej.2010.03.083.
(12) Jensen, K. F. *Chem. Eng. Sci.* **2001**, *56*, 293–303.
(13) Ajmera, S. K.; Delattre, C.; Schmidt, M. A.; Jensen, K. F. *Sens. Actuators, B* **2002**, *82*, 297–306.
(14) Wallis, G.; Pomerantz, D. *J. Appl. Phys.* **1969**, *40*, 3946–3949.
(15) Vesborg, P. C. K.; Olsen, J. L.; Henriksen, T. R.; Chorkendorff, I.; Hansen, O. *Rev. Sci. Instrum.* **2010**, *81*, 016111.
(16) Einaga, H.; Harada, M.; Futamura, S.; Ibusuki, T. *J. Phys. Chem. B* **2003**, *107*, 9290–9297.
(17) Gong, D.; Grimes, C. A.; Varghese, O. K.; Hu, W. C.; Singh, R. S.; Chen, Z.; Dickey, E. C. *J. Mater. Res.* **2001**, *16*, 3331–3334.
(18) Paulose, M.; Shankar, K.; Yoriya, S.; Prakasam, H. E.; Varghese, O. K.; Mor, G. K.; Latempa, T. A.; Fitzgerald, A.; Grimes, C. A. *J. Phys. Chem. B* **2006**, *110*, 16179–16184.
(19) Shankar, K.; Basham, J. I.; Allam, N. K.; Varghese, O. K.; Mor, G. K.; Feng, X.; Paulose, M.; Seabold, J. A.; Choi, K.-S.; Grimes, C. A. *J. Phys. Chem. C* **2009**, *113*, 6327–6359.
(20) Shankar, K.; Mor, G. K.; Prakasam, H. E.; Yoriya, S.; Paulose, M.; Varghese, O. K.; Grimes, C. A. *Nanotechnology* **2007**, *18*, 065707.
(21) In, S.-I.; Hou, Y.; Abrams, B. L.; Vesborg, P. C. K.; Chorkendorff, I. *J. Electrochem. Soc.* **2009**, *157*, E69–E74.
(22) Ohtani, B. *Chem. Lett.* **2008**, *37*, 216–229.
(23) Egerton, T. A.; King, C. J. *J. Oil Colour Chem. Assoc.* **1979**, *62*, 386.
(24) Linsebigler, A.; Lu, G.; Yates, J., Jr. *Chem. Rev.* **1995**, *95*, 735–758.
(25) Vorontsov, A. V.; Savinov, E. N.; Barannik, G. B.; Troitsky, V. N.; Parmon, V. N. *Catal. Today* **1997**, *39*, 207–218.
(26) Peral, J.; Ollis, D. F. *J. Catal.* **1992**, *136*, 554–565.
(27) Aguado, M.; Anderson, M.; Hill, C., Jr. *J. Mol. Catal.* **1994**, *89*, 165–178.
(28) Hwang, S.; Lee, M. C.; Choi, W. *Appl. Catal., B* **2003**, *46*, 49–63.

JP100552X